

# TIME RESOLVED BREAST TRANSILLUMINATION: ANALYTICAL, NUMERICAL AND EXPERIMENTAL STUDY

THESE No 1119 (1993)

PRESENTÉE AU DÉPARTEMENT DE PHYSIQUE

ÉCOLE POLYTECHNIQUE FÉDÉRALE DE LAUSANNE

POUR L'OBTENTION DU GRADE DE DOCTEUR ES SCIENCES

PAR

EMMANUEL B. DE HALLER

Physicien diplômé EPFZ  
originaire de Berne

acceptée sur proposition du jury:

Dr C. Depeursinge, rapporteur  
Prof. J.-J. Meister, corapporteur  
Prof. R.-P. Salathé, corapporteur  
Prof. S. T. Flock, corapporteur  
Dr P. Lenz, corapporteur

Lausanne, EPFL  
1993



## Abstract

*This work is mainly dedicated to the study of light transport through biological tissues and particularly the propagation of a light pulse. This study does not take into account the nonlinear properties of biological tissues. Different approaches were planned and then compared in order to understand and describe the physical phenomenon as well as possible. The analytical approach based on the Boltzmann transport equation gives satisfactory results for the qualitative description of the transmission of a collimated beam, but lacks precision for the quantitative determination. Nevertheless, the analytical consideration remains a useful approach to predict the behaviour of light propagating through tissues and a versatile method for this kind of study. A Monte-Carlo simulation has been developed to predict the quality of time resolved images of the breast by transillumination. The smallest diameter of a detectable carcinoma located in the breast has been computed. The simulation suggests that time-resolved imaging of the breast is possible and invaluable in the near infra-red (NIR) by transillumination. The enhancement of the transfer function by the introduction of time resolved detection is limited by the contribution of noise at short gating times. The estimated diameter of the smallest detectable sphere is derived from the image quality index theory (or IQI theory) and its value is around 4 [mm] for a 40 [mm] thick breast. The simulated images of a sphere (approximating the carcinoma) within a homogeneous medium (approximating the surrounding tissue) show a significant improvement of the image with short gating time. Experimental trials with a streak camera have confirmed our model, and the gating of the signal has been shown to be possible with an ultrafast electro-optic modulator based on the travelling wave principle.*

**Keywords**—Monte-Carlo, breast cancer, transillumination, time-of-flight, image quality index.

## Résumé

*Ce travail est essentiellement consacré à l'étude du transport de la lumière au travers de tissus biologiques et particulièrement à la propagation d'un pulse lumineux. Cette étude ne tient pas compte de l'effet non linéaire des tissus biologiques. Différentes approches ont été entreprises dans le but de comprendre et de décrire le phénomène physique avec précision. L'approche analytique basée sur l'équation du transport de Boltzmann donne des résultats qualitatifs satisfaisant mais manque de précision lors de la détermination quantitative. Ensuite une simulation sur la base de la méthode de Monte-Carlo a été développée pour prédire la qualité d'images résolues en temps obtenues par transillumination du sein. Le diamètre de la plus petite lésion cancéreuse détectable a pu être calculée. La simulation suggère que l'imagerie résolue en temps du sein est possible et prometteuse dans la région du proche infrarouge. L'amélioration des fonctions de transfert est pourtant limitée par la contribution du bruit pour des temps d'intégration trop petits. Le diamètre estimé de la plus petite lésion détectable est dérivé de la théorie de l'indice de qualité d'image (ou IQI) et cette valeur se situe à 4 [mm] pour un sein de 40 [mm] d'épaisseur. Les images simulées d'une sphère (simulant le carcinome) dans un milieu homogène (simulant les tissus environnants) démontrent une amélioration significative de l'image pour des temps d'intégration courts. Des mesures avec une caméra streak ont pu confirmer le modèle et le fenêtrage du signal par un modulateur électro-optique sur le principe de l'onde progressive a pu être observé.*

**Mots clefs**—Monte-Carlo, cancer du sein, transillumination, temps de vol, indice de qualité d'image.

## Zusammenfassung

*Diese Arbeit beschäftigt sich überwiegend mit dem Studium von Lichttransport durch biologische Gewebe und besonders von Lichtimpulsausbreitung. Die nichtlinearen Effekte der biologischen Gewebe wurden in diesem Studium nicht berücksichtigt. Verschiedene Annäherungen wurden untersucht, um das physikalische Phänomen vollständig zu verstehen und zu beschreiben. Die analytische Annäherung auf Basis der Boltzmann'schen Gleichung bringt befriedigende qualitative Ergebnisse hervor aber keine exakten quantitativen Bestimmungen. Eine Monte-Carlo Simulation wurde später entwickelt, um die Qualität von zeitaufgelöster Bilder mit Brusttransillumination vorauszusehen. Der kleinste Durchmesser einer diagnostizierbaren Schädigung in der Brust wurde berechnet. Die Simulation zeigt, dass die Zeitauflösung während der Bildaufnahme möglich und im Nah-infrarot (NIR) Bereich wertvoll ist. Die Verbesserung der Übertragungsfunktionen ist trotzdem durch den Beitrag des Rauschens für kürzeste Integrationszeiten begrenzt. Der geschätzte Durchmesser einer detektierbaren Schädigung ist etwa 4 [mm] für eine 40 [mm] dicke Brust. Simulierte Bilder von einer Sphäre (als Krebschädigung) in einem homogenen Medium (als Gewebe) zeigen eine deutliche Verbesserung des Bildes für kurze Integrationszeiten. Messungen mit einer Streak Kamera bestätigten unser Modell. Die Möglichkeit des "gating" des Signals wurde mit einem elektrooptischen Lichtmodulator ausgeführt.*

**Stichwörter**—Monte-Carlo, Brustkrebs, Transillumination, Flugzeit, Bildqualität Index.

## Riassunto

*Questo lavoro è principalmente consacrato allo studio del trasporto della luce attraverso dei tessuti biologici, e in particolare alla propagazione di un impulso luminoso. Gli effetti non lineari dei tessuti biologici non sono tenuti in considerazione in questo studio. Diverse idee sono state investigate per capire e descrivere al meglio il fenomeno fisico. Il metodo analitico offre risultati qualitativi soddisfacenti ma manca di precisione per una determinazione quantitativa. Una simulazione Monte-Carlo è stata ideata per determinare la qualità di un'immagine a risoluzione temporale di una transilluminazione del seno. Il diametro della più piccola lesione detetabile è stato calcolato. La simulazione suggerisce che la transilluminazione a risoluzione temporale è possibile e valida nella regione del infrarosso vicino. Il miglioramento delle funzioni di trasferimento è purtroppo limitato a causa del rumore dei fotoni per dei tempi d'integrazione troppo corti. Il diametro stimato dalla più piccola lesione detetabile proviene direttamente dalla teoria dell'indice di qualità d'immagine (o teoria dell'IQI) e il suo valore è di 4 [mm] per un seno di 40 [mm] di spessore. Le immagini simulate di un oggetto sferico (rappresentando la lesione) in un medio omogeneo (rappresentante il tessuto) mostrano un miglioramento significativo dell'immagine per dei tempi d'integrazione corti. Le misure effettuate con una streak camera hanno confermato il nostro modello e la possibilità di "gating" del segnale con un modulatore elettro-ottico è stata osservata.*

**Parole chiave**—Monte-Carlo, cancro del seno, transilluminazione, tempo di volo, indice di qualità d'immagine.

---

## Acknowledgements

I am deeply grateful to my supervisor, Dr. Christian Depeursinge, for his support and collaboration during this thesis project.

During the course of this research, Dr. Lionel Desponds has provided a fruitful help in the understanding of the image quality index theory.

For the last two years, Pr. Stephen Thomas Flock brought rich informations and greatly helped me in the comprehension of light transport through biological tissues.

Many thanks to Claude Genton, M.D., of the Institute of Pathology of the University Hospital Center in Lausanne who provided the tissue samples and has brought a lot of useful informations about the histology and the pathology of the human breast.

Thanks to Pr. Jean Buttet, Pr. Jean-Jacques Meister, Pr. René-Paul Salathé and Dr. Peter Lenz for having participated in the jury of this thesis.

Many thanks to Jose Llambias for his technical support and for his contribution to the development and trials of the infrared camera.

Thanks to Ausilio Bauen, Frédéric Bevilacqua, Ramiro Conde, Olivier Coquoz, Pierre Marquet and Quet Kim Yong Teck for their invaluable contribution.

Thanks to Xavier Clivaz and his colleagues of the Laboratoire d'Optique Appliquée (LOA) for their critical input.

Many thanks to Olivier Charpié (GMP S.A.) who spent so many hours to adjust and check the dye laser for a proper pulsed operation.

Thanks to Uwe Denzer (Hamamatsu Germany) who supplied the streak camera.

I would like to express my entire gratitude to my parents whose support and comprehension in my education made this possible.

I am also grateful to Mr. Jacques Darbellay and the teachers of Maya-Joie (1978) for having built the fundamentals of my scholar education.

Special thanks to Angela for her infinite patience.

I also would thank my friends, relatives, colleagues of the Laboratoire de Génie Médical and all those I forget, for their friendly support.

An unexpected thank to Nyda and Waco, my beloved dogs, who accompanied me for long relaxing walks.

This thesis work has been supported by the Swiss National Fund for Scientific Research grant FN 32-31261.91.

## Notation

The “système international d’unités” (SI) is generally used, unless specified when other units are expressed in the literature or used for convenience.

Notation	Units	
K-M		P. Kubelka and F. Munk
H-G		L.G. Henyey and J.L. Greenstein
NIR		near infrared
CCD		charge coupled device
FWHM		full width at half maximum
TOF	[ps]	time of flight
PSF		point spread function
LSF		line spread function
C	[mm <sup>-1</sup> ]	contrast
MTF		modulation transfer function
W		Wiener spectrum
SNR		signal to noise ratio
IQI	[mm]	image quality index
OD		optical density
OD <sub>t</sub>		temporal optical density
$\mathcal{F}$		Fourier transform
$\mathcal{F}^{-1}$		inverse Fourier transform
①		medium 1
②		medium 2
a		scalar
$\vec{a}$		vector
$\vec{r}=(x,y,z)=(r,z)$	[mm]	spatial vector (coordinates)
$\vec{f}=(f_x,f_y,f_z)$	[mm <sup>-1</sup> ]	spatial frequency vector
CD		direction cosine



$\hat{z}$		unit vector in the direction $z$
$\hat{s}$		unit vector in the direction $\omega$
$\hat{s}'$		unit vector in the direction $\omega'$
$L(\hat{r}, \hat{s})$		flux of photons
$U(\hat{r}, \hat{s})$		average flux of photons
$\vec{F}(\hat{r})$		current of photons
$L_d(\hat{r}, \hat{s})$		scattered flux of photons
$L_{ir}(\hat{r}, \hat{s})$		reduced flux of photons
$i(z)$		forward scattered intensity
$j(z)$		backscattered intensity
$c = 0.218$	[mm/ps]	average speed of light in tissues
$n = 1.37$		average refraction index in tissues
$p(\hat{s}, \hat{s}')$		single scattering phase function
$g$		anisotropy factor (mean cosine)
$K$	[mm <sup>-1</sup> ]	absorption coefficient (K-M)
$S$	[mm <sup>-1</sup> ]	scattering coefficient (K-M)
$\kappa$		diffusion coefficient
$\Sigma_a$	[mm <sup>-1</sup> ]	absorption coefficient
$\Sigma_s$	[mm <sup>-1</sup> ]	scattering coefficient
$\Sigma_s' = \Sigma_s(1-g)$	[mm <sup>-1</sup> ]	reduced scattering coefficient
$\Sigma_t = \Sigma_s + \Sigma_a$	[mm <sup>-1</sup> ]	total attenuation coefficient
$W_{abs}$		absorption condition
$\phi$	[radian]	radial angle
$\theta$	[radian]	azimutal angle
$\alpha_i$	$0 < \alpha_i \leq 1$	$i^{\text{th}}$ random number
$L$	[mm]	free pathlength
$\bar{L}$ or mfp	[mm]	mean free path
$t_f$	[ps]	maximum TOF
$t_b$	[ps]	ballistic time



# Contents

Abstract	1
Résumé	2
Zusammenfassung	3
Riassunto	4
Acknowledgements	5
Notation	6
Contents	9
<b>CHAPTER 1</b>	
<b>INTRODUCTION</b>	<b>15</b>
1.1. Motivation	16
1.2. Biooptics	18
1.3. Diaphanography	21
1.4. Mechanism responsible for the image	22
1.5. State of the art	24
1.5.1. Chrono-coherent imaging (CCI)	24
1.5.2. Heterodyne detection	25
1.5.3. Time-gating	26
1.5.4. Streak camera	27
1.5.5. Ultrafast Kerr cell	28
1.5.6. Time-constraint imaging	29
1.5.7. Discussion	29
<b>CHAPTER 2</b>	
<b>ANALYTICAL MODEL</b>	<b>31</b>
2.1. Optical coefficients	32
2.2. Analysis of light transport	33
2.3. The diffusion model	35
2.4. Location of a spherical object	36
2.5. Pulse propagation	39
2.6. Phase function	43
<b>CHAPTER 3</b>	
<b>NUMERICAL METHOD</b>	<b>47</b>
3.1. Simulation of light propagation through tissues	48
3.1.1. Source	49
3.1.2. Sample	50

3.1.3. Detector	50
3.2. Optical parameters	51
3.3. Image parameters	52
3.4. Simulation process	52
3.5. Results of the simulation	55
3.5.1. Optical density	62
3.5.2. Point spread function	64
3.5.3. Contrast	67
3.5.4. Pulse transmission	68
3.5.5. Image Quality Index or IQI	69
3.5.6. Estimated IQI	71
3.5.7. Simulated images	73
<b>CHAPTER 4</b>	
<b>EXPERIMENT</b>	<b>77</b>
4.1. Tissue characterisation	77
4.1.1. Experimental setting	78
4.1.2. Histology and pathology	79
4.1.3. Tissue characteristics	80
4.2. Time resolved imaging	82
4.2.1. Source	82
4.2.2. Electro-optic amplitude modulator	83
4.2.3. Detector	85
4.3. Results	86
4.3.1. Streak camera	86
4.3.2. Pulse gating	91
4.3.3. Image of a slit	94
<b>CHAPTER 5</b>	
<b>CONCLUSION</b>	<b>101</b>
5.1. Analytical approach	102
5.2. Numerical approach	102
5.3. Experimental approach	103
5.4. Perspective	103
<b>BIBLIOGRAPHY</b>	<b>107</b>
<b>APPENDIX</b>	<b>123</b>
A.1. Tissue spectroscopy	123
A.2. Optical oximetry	125

---

A.3. The two-flux Kubelka-Munk model	130
A.4. The Boltzmann equation	132
A.5. Diffusion approximation	133
A.6. The diffuse intensity	138
A.7. Free pathlength	141
A.8. Image parameters and Image Quality Index	142
A.9. Program	145
A.10. Formaldehyde, hematoxylin and eosin	149
A.11. Modulator test data sheet	151
A.12. CCD imager	153
Curriculum vitae	155



**“-Adieu dit le renard. Voici mon secret. Il est très simple:  
on ne voit bien qu’avec le cœur.  
L’essentiel est invisible pour les yeux ”**

*Le Petit Prince* de Antoine de Saint Exupéry





**CHAPTER 1*****INTRODUCTION***

Transillumination, a term describing any method for viewing the interior of an object by shining light through it, has been applied as diagnostic aid since the beginning of this century in inflammatory diseases of the sinuses or for the differentiation between solid tumours of the testis and hydrocele. In the present days, the most common use of transillumination is the optical oximeter, which gives information on the blood oxygenation (Taylor and Whitwam, 1986, Mendelson and Ochs, 1988). Light sources as laser diodes illuminate a part of the body (generally the fingertip or the earlobe) at two or more wavelengths and on the basis of differential spectrophotometry of the transmitted or backscattered light, the blood oxygenation is computed (de Haller and Depeursinge, 1991). Similar systems have been developed to detect brain lesions in neonates by shining light through the head (Cope et al., 1988, Cope and Delpy, 1988).

M. Cutler (1929) started to evaluate breast lesions after observation on breast specimens suggested the possibility of establishing some points of difference between tumours of different density. This method lost rapidly its interest due to the poor spatial resolution of the technique. The time resolved transillumination should be a new promising non ionising imaging modality. The use of a pulsed

laser source in the near infrared (NIR) region where biological tissues are fairly transparent and an efficient time-gated detection system would lead to a practical and secure tool for breast cancer screening and give better spatial resolution.

The past few years have brought numerous experiments on time resolved transillumination and the obtained results are convincing but there has been lack of clinical interest because the transilluminated sample being too thin or propitious to that kind of measure. Further a major task consists in the accurate description of light distribution in tissues by a theoretical model, which should enlighten the understanding of the process of time resolved transillumination. With that goal in mind, the following work will investigate analytical and numerical modelling to describe as faithfully as possible the time resolved transillumination of biological tissues and then try to confirm the models with experimental results.

### **1.1. Motivation**

On the first hand, the characterisation of biological tissues is one of the challenges of modern medicine. The study of light propagation through tissues and an eventual differentiation would bring a useful technique for pathology. On the other hand, breast cancer struck one woman out of ten in 1991, and one fourth of the suffering patients died (Wallis, 1991). Furthermore, 76.6% survive five years after surgery and 63% are alive after 10 years. This type of cancer is primarily observable in women in the 45 to 55 years old range and is the major cause of mortality for women within 45 and 50 years old. Unfortunately this cancer strikes also 3% of the women under 35 and in 90% of the registered cases it is lethal because of the too late detection (McSweeney and Egan, 1984). The growth of a breast carcinoma follows an exponential curve set by a constant rate of cellular division (Fig. 1.1). Twenty years ago a satisfactory method to detect an early carcinoma was not available and the detection usually occurred in the post-clinical phase when metastasis were already present (Gullino, 1977). For the last ten years, a regular screening of women in various countries helped in the early detection of the breast cancer in 70% of the women in the 50 years old and up (Jones, 1982).

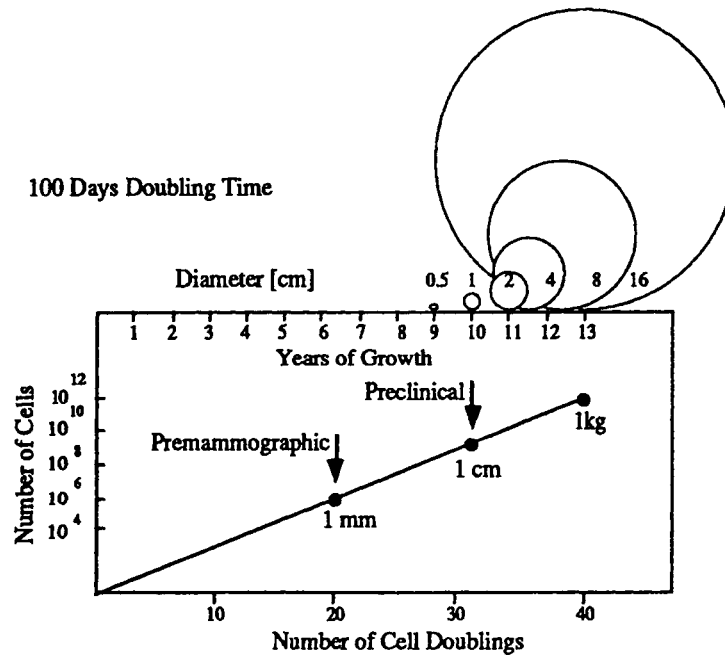


Fig. 1.1: demonstration of the long preclinical existence of a breast carcinoma. The data are compiled on 100 days of tumour doubling time as an average value (Gullino, 1977).

Images of the interior of living bodies can be formed using x-rays, magnetic resonance, ultrasound, electrical impedance, positron-emission, thermal emission, and other probes. Each of these methods has drawbacks that limits use as a continuous, noninvasive, nondestructive monitor for living organisms. The most competitive and modern technique is the mammography: the breast is compressed between two plates, an x-ray source irradiates the breast and the image (mammogram) is recorded on a photosensitive substratum after passing through a phosphor plate. This method enables the detection of more than 70% of the breast cancers in screened patients (Gullino, 1977, Feig, 1984, Lester, 1984, Drexler et al., 1985, Gold et al., 1986). This technique uses ionising radiation, and mammography is suspected to induce 0.2% of the breast cancers (Fox et al., 1978, Shapiro et al., 1982, Feig, 1984). This reason makes unacceptable a screening on younger patients (40 years old and below, McSweeney et al., 1984). To allow an earlier screening, other investigation methods were developed or evaluated: MRI (magnetic resonance imaging) suffers from controversial results and still has to prove its value (expensive and toilsome); thermography which only provides surface information (Isard, 1982,

Jones, 1982); echography which lacks a precise characterisation of the lesions (benign or malignant lesion) and diaphanography which is mainly used as a preliminary examination before a biopsy (Ohlsson et al., 1980, Angquist et al., 1981, Isard, 1981, 1982, Jones, 1982, Marshall et al., 1984, Shalev, 1984, Drexler, 1985, Greene et al., 1985, Wallberg, 1985, Wallberg et al., 1985, 1986). The breast cancer detection rate is only 30% with diaphanography (Geslien et al., 1985, Gisvold et al., 1986, Monsees et al., 1988) compared to the 70% of mammography. In spite of these new investigations, mammography remains actually the best screening tool, giving an image definition and contrast enabling a precise and reliable diagnosis (Shapiro et al., 1982, Feig, 1984, Lester, 1984).

## 1.2. Biooptics

The propagation of light through biological tissues is an issue of growing concern in many medical applications, particularly in laser medicine. Many models that predict light distribution within tissues have been developed and the accuracy of these models depend upon how well the optical characteristics of tissues are known. Light is transmitted through a biological medium with

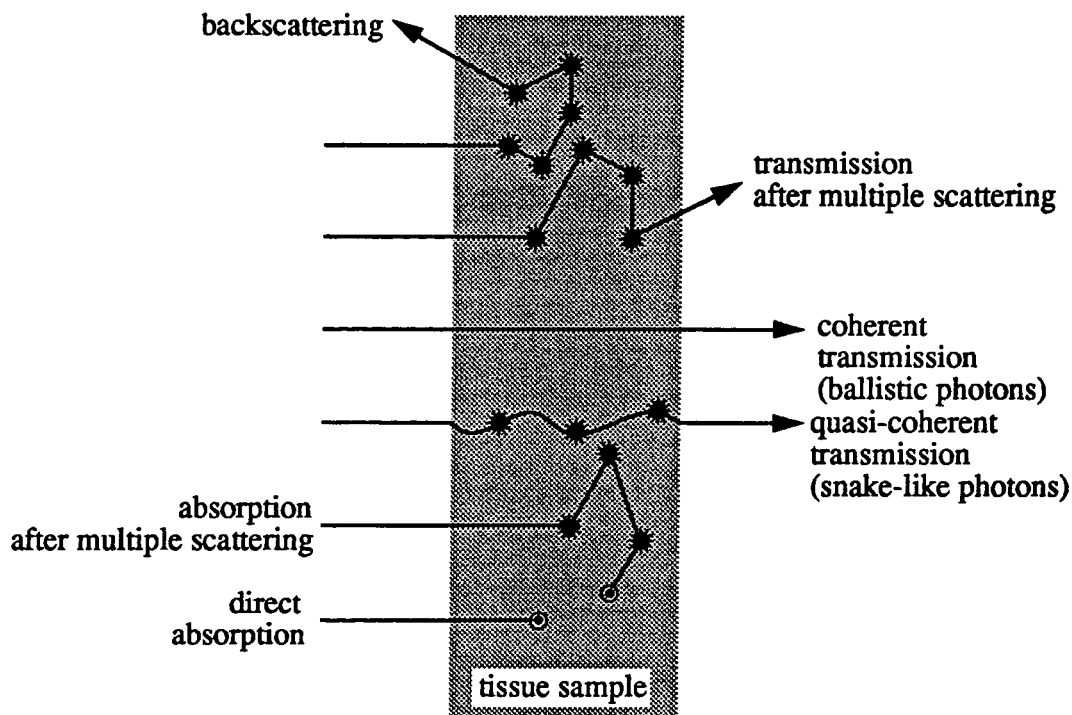


Fig. 1.2: scheme of the different interactions between light and tissues or "photon history".

varying degrees of absorption and scattering (Fig. 1.2), but in the NIR range, scattering dominates because the inhomogeneities of cellular structures and particle size are of the order of an optical wavelength.

Absorption occurs at discrete locations where pigments are present (nucleus or cytoplasm) and depends on the wavelength (see also appendix A.1). Scattering also occurs at discrete locations and is supposedly fully elastic: (i) the photon is able to go through the tissue unscattered, this is a *ballistic* photon or coherent transmission. This phenomenon is mainly observable in weakly scattering tissues or optically thin samples, but for a thick part of the body, it is mostly improbable that a coherent transmission could be observed (Flock et al., 1987, Andersson et al., 1990, Hebden and Kruger, 1990); (ii) the photon undergoes only a few diffusions (i.e. the photon does not drift much from its original direction), and is known as a *snake-like* photon or quasi-coherent transmitted photon which conserves part of their initial coherence so that they interfere with the original beam; (iii) the photon is *multiply scattered*, losing any spatial or anatomical information. The differentiation of these three ways of photon transmission is easily done on a time scale with a short pulse as input (Fig. 1.3). The ballistic photons go straight to the detector within the time  $t_b = \frac{z}{c}$  where  $c$

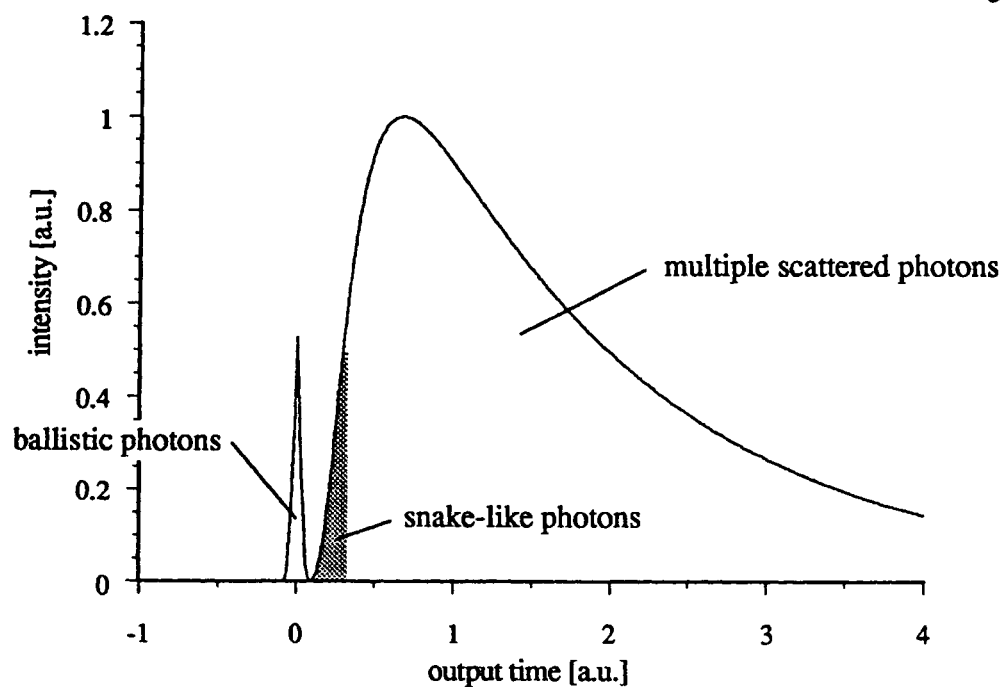


Fig. 1.3: differentiation of the various types of transmitted photons on an output signal (short pulse as input).

is the speed of light in the tissue and  $z$  the tissue thickness, then the snake-like photons build the very first part of the output signal and finally the multiple scattered photons build the rest of the output signal. The scattering and the amount of interactions depend upon the tissue constitution, the size and shape of the cells and the concentrations of particles in the cytoplasm.

Cells are commonly several microns in diameter, muscle cells may be a few millimetres long and nerve cells may be over a metre long. A cell consists of a thin membrane ( $\sim 75$  [Å] thick), the cytoplasm which is a colloidal suspension of particles and the nucleus (Fig. 1.4). Epithelial tissue consists in dense layered cells that cover or line a surface, connective tissue supports and connects tissues

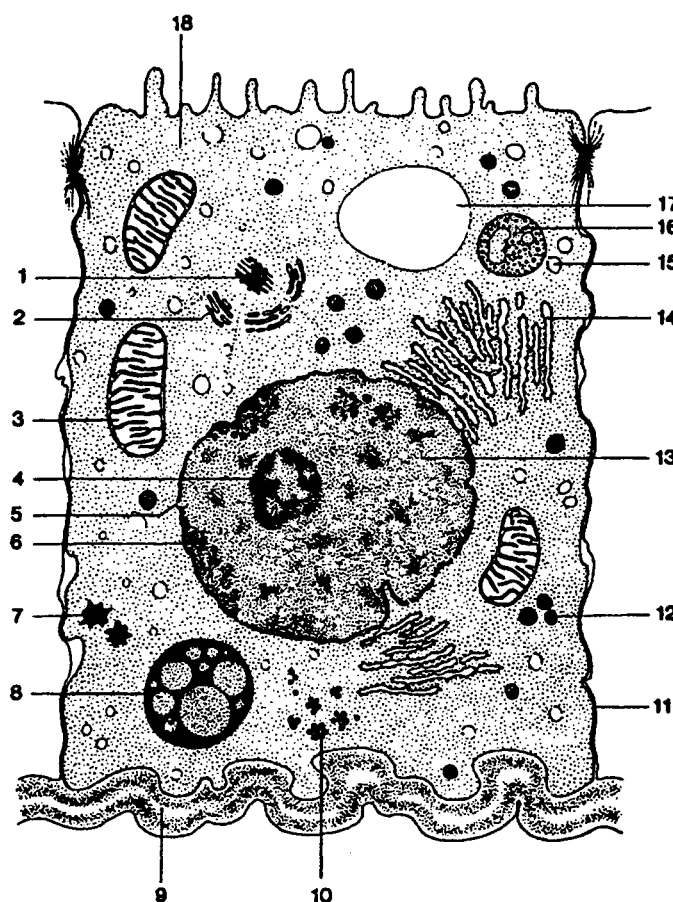


Fig. 1.4: scheme of a cell from electron microscopy.  
 1.centrosome. 2.Golgi apparatus. 3.mitochondria.  
 4.nucleolus. 5.nucleus pore. 6.nucleus membrane.  
 7.fatty droplet. 8.pigment. 9.basal membrane.  
 10.glycogen. 11.cellular membrane. 12.granule.  
 13.nucleus. 14.endoplasmic reticulum. 15.small  
 vacuole. 16.lysosome. 17.big vacuole.  
 18.cytoplasm.

to the skeleton, muscle consists of tight bundled cells that are 1 to 40 [mm] long and up to 40 [ $\mu\text{m}$ ] in diameter and nervous tissue consists of neurones or nerve cells which have a vital centre connected to other nervous cells by long arms or axons, like an octopus

### 1.3. Diaphanography

The diaphanography developed by M. Cutler (1929) enabled the visualisation of a lesion within a breast. The examination is made in a totally dark room with the patient sitting opposite to the examiner. An intense white light source is placed against the under surface of the breast and gradually moved as different areas of the breast are inspected successively, the object being to place the particular portion in question directly between the light and the examiner's eye or a camera (Fig. 1.5). The difference of absorption of the various tissues enables the

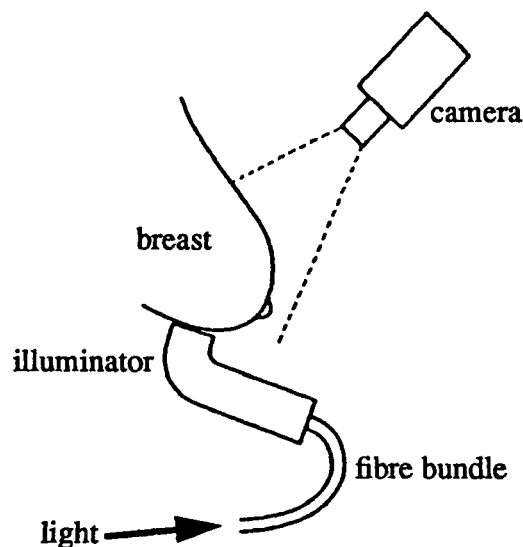


Fig. 1.5: diaphanography principle. The light is guided by a fibre bundle to an illuminator and the image is recorded by a camera.

detection of the lesions which look darker (dense tumour or haematoma) or clearer (cysts) in the surrounding tissues. Nevertheless, the edges of the lesions are blurred and the contrast is weak. Thus diaphanography gives a rough anatomical distribution and characterisation of breast lesions. The use of two wavelengths or more gives useful information on the metabolism of the lesions and the surrounding tissues. This is possible according to optical oximetry (de

Haller and Depeursinge, 1991) which is a technique widely used for the determination of blood and tissue oxygenation (see also appendix A.2). Furthermore, the diaphanography provides information on the lesion itself, compared to mammography which gives informations on the microcalcifications growing in the cancerous lesion.

This method could be improved with modern ultra-fast optical detection technology. An intense source illuminates a slab of tissue and the scattered photons are removed from the signal in order to get a sharp anatomical image built by the very few ballistic photons, if any, and the snake-like photons. The pulsed source, available since the 1960's, is the laser which is the most adequate tool for this purpose (monochromatic, weak divergence, short pulses and high power density). The choice of the NIR illumination is motivated by the fair transparency of biological tissues at these wavelengths (see also appendix A.1). The most relevant problem is the spatial (ie: temporal) filtering of the signal in order to get useful information on the images. The whole research on time resolved imaging was directed towards pathlength limitation, i.e. allowing a photon to fly a certain distance (ie: a certain time) thus eliminating the noisy overflow of the multiple scattered photons.

#### **1.4. Mechanism responsible for the image**

The formation of the image is mainly due to differential absorption in tissues (Watmough, 1982, 1983, Shalev et al., 1985). Tissues have optical properties described by three components, absorption, scattering and phase function. Absorption occurs in the chromophores such as haemoglobin, myoglobin, cytochrome or chromatin. These pigments have a particular absorption spectrum which enables their differentiation and for the three first chromophores, there is a further difference between the reduced and oxidised state. The scattering of light occurs at the interfaces between cells or components of the cells. Multiple scattering is a source of blur and so the resolution of the images is strongly deteriorated (Fig. 1.6). Finally the phase function determines in which direction the light would be the most often scattered.

The spectrophotometric study of haemoglobin shows that blood has absorption



peaks (see also appendix A.1) in the red and NIR region so that a strongly perfused part of the body should appear as a shadow, and other tissues such as bone, adipose or skin are translucent and look brighter. For breast tissues, there is a window between 700 and 1100 [nm] where the lowest percentage of light is absorbed (Fig. 1.7). The carcinoma is suspected to be more irrigated than the



Fig. 1.6: diaphanography of a right healthy breast and a left breast showing a dense tumour (Cutler, 1929). The blood vessels on the breast surface are easily detectable.

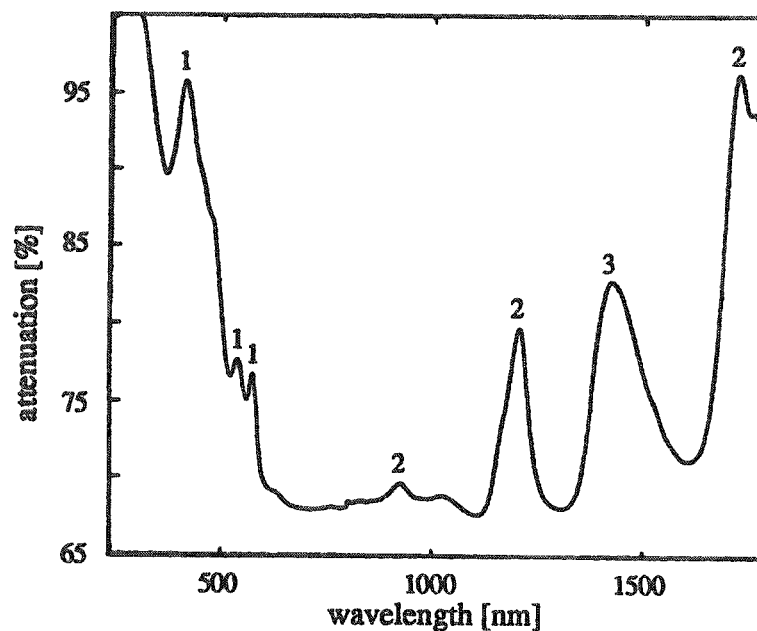


Fig. 1.7: attenuation spectrum through a 3 [mm] thick slab of breast tissue (from Marks, 1992). Contribution of haemoglobin (1), fat (2) and water (3).

surrounding tissues (Watmough, 1982, Jain and Ward-Hartley, 1984, Shalev et al., 1985, Vaupel, 1990, Flock, 1991), it should be then easily differentiated from the surrounding tissues which are normally perfused. Furthermore, the nucleus contains chromatin, a chromophore responsible for light absorption, and the cancerous cells are known to have a bigger nucleus than normal cells. This is mainly due to the fact that cancerous cells have a wrong encoding and do not behave as a normal. These cells are dividing permanently so that the nucleus is always synthesising proteins and has a bigger volume than a normal healthy nucleus.

### **1.5. State of the art**

For the three last years, numerous research groups have investigated the analysis of light transport through turbid media with new techniques of time resolved transillumination.

The theoretical study of photon transmission through tissues is often based on transport theory and numerical simulations. These approaches are preferred to the exact solutions using Maxwell equations because of the inhomogeneity of biological tissue. Light transport theory has lead to a better comprehension of the behaviour of photons in biological tissues and to a method for an objective characterisation of tissues.

Based on recent technological progress or development in pico- and femtoseconds technique as well as new detection devices, a renewal of interest in a non-invasive screening technique made time resolved diaphanography a trend. Despite a large unexplored theoretical field on tissue optics, the modern investigation on time resolved transillumination is mainly dedicated to experimental tentatives particularly in the low coherence imaging.

#### **1.5.1. Chrono-coherent imaging (CCI)**

J. Seraphin and K. Spears (1989) proposed the chrono-coherent imaging technique (Fig. 1.8). A short pulse of laser light is split into two coherent pulses, one of which is used to transilluminate the object of interest while the other serves as the coherent reference light needed for hologram formation. A series of

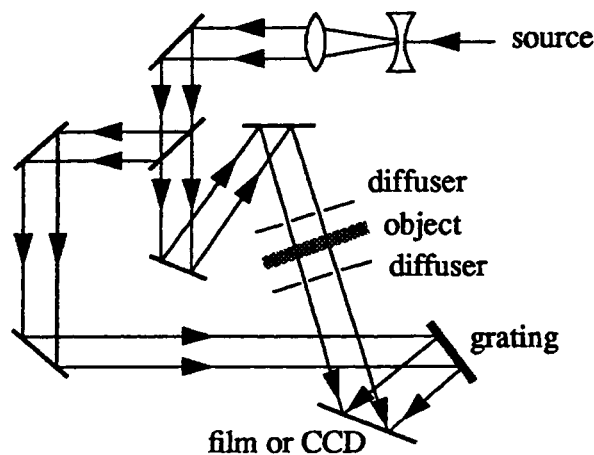


Fig. 1.8: transmission geometry for CCI.

mirrors is arranged so that both pulses travel the same distance before reaching a photographic plate or film. Since the reference and object pulses must arrive at the film within the coherence time interval to create a hologram, and since scattered light travels random paths of generally greater lengths, the use of very short pulses substantially reduces the amount of obscuring scattered light included in the hologram. The geometry is such that the reference pulse strikes the film at an acute angle, and it sweeps across the film like a wave hitting the shore. Consequently, a very short pulse illuminates only a narrow slice of the film at any instant. Thus the hologram is actually a continuous image sequence revealing time delay as well as attenuation of the object pulse.

Spears et al. (1989) recorded a distinct image of a “E” letter placed between two diffusing plates. Further, Chen et al. (1991) described such an experiment with electronic holography (to reduce stability problems) and obtained images of two crossed needles through a 6 [mm] slab of raw chicken meat.

### 1.5.2. Heterodyne detection

M. Toida et al. (1990) developed an imaging technique using an optical heterodyne system (Fig. 1.9). The laser beam is divided in two different paths by a beam splitter. One passes through an phase modulator to phase-shift the signal and the beam is then directed towards the sample. The second beam serving as a local oscillator passes through another phase modulator to phase-shift the signal slightly more than the first beam. The two wavefronts are then effectively

superimposed before an optical frequency mixer employing a photomultiplier tube. The output signal from the photomultiplier is amplified and filtered electronically and then recorded on an x-y recorder as a function of the shifted position of the local oscillator beam with respect to the beam axis.

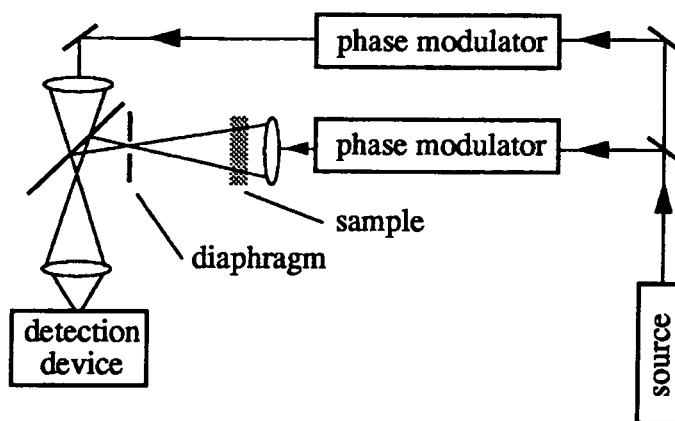


Fig. 1.9: optical heterodyne imaging principle.

With this method an experimental verification of the directional resolution capability for image detection in highly scattering media has been done and compared with the conventional direct detection technique, which prevents complete imaging of the object due to light scattering. A test bar chart has been recorded through a milk-gelatine solution. Further a tomographic image of a chicken leg in vitro specimen has been reconstructed with this method.

### 1.5.3. Time-gating

S. Andersson et al. (1990) used a photon counter to select the less scattered photons emerging from the sample with the delayed coincidence technique. A laser pulse illuminates the sample and the signal is recorded in the photon counter through an optical fiber with an acceptance angle of  $2^\circ$  (Fig. 1.10). The time delay is triggered optically on the incident pulse. The signal is fed through a fast amplifier to a time-to-amplitude converter. The stop signal comes from a diode triggering on the incident pulse. Then the output signal goes to an analyser in which an histogram of arrival of photons is formed (ie: temporal dispersion curve).

This method showed significant results on images of opaque black rubber cords in a paraffin phantom. The contrast is enhanced in comparison with the

conventional imaging technique. S. Andersson is the only one to publish in vivo results of a transilluminated hand. A scan has been done on a finger in order to detect the bone and again the contrast is enhanced.

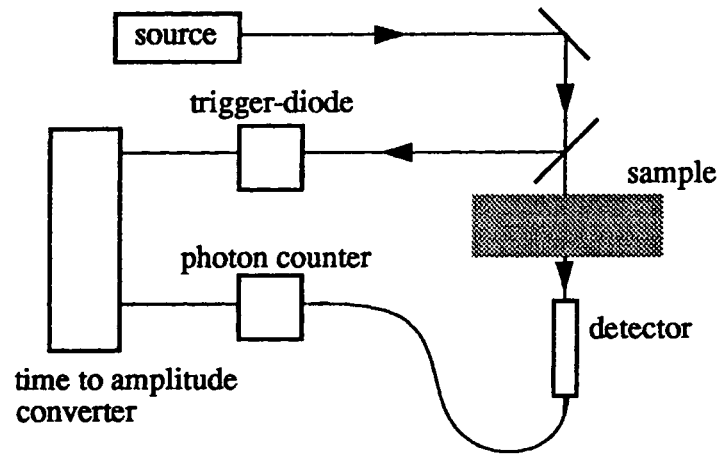


Fig. 1.10: time gating experimental setting.

#### 1.5.4. Streak camera

J. Hebden and R. Kruger (1990) used a streak camera to make an image through a scattering phantom (Fig. 1.11). A picosecond laser pulse is incident on a

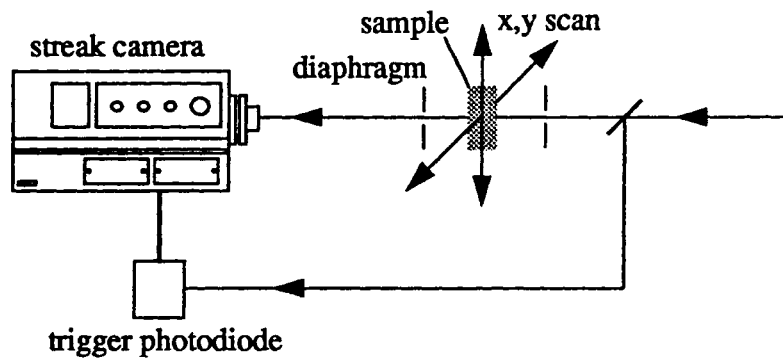


Fig. 1.11: experimental setting with the streak camera

sample and the streak camera will measure, as a function of the time, the intensity of the transmitted light which emerges from a region near to the optical axis. The photons detected first will have been deviated least from the optical axis. Only those photons will be taken in account for the formation of the image. This technique allowed the imaging of opaque disks in a milky solution, and the images have been recorded with various time window showing the blurring of

the image for wide time windows and the strong contribution of noise for too narrow time windows.

### 1.5.5. Ultrafast Kerr cell

M.A. Duguay and J.W. Hansen (1969) (see also Duguay and Mattik, 1971) proposed an experimental setting to “freeze” a short light pulse in order to visualise it. This made possible photographing light pulses in flight. An infrared pulsed laser source generates a train of pulses at a given wavelength 1064 [nm]. A KDP doubling crystal transforms the pulses in shorter pulses (about  $\sqrt{2}$  shorter) of wavelength 532 [nm] (second harmonic generation). The green pulses are sent via a variable optical delay line into a rectangular cell containing a colloidal suspension. The suspension is calculated to scatter a few percents of the light. It is important that the green pulses are vertically polarised so that much of the light is scattered toward the camera. The green pulses become brightly visible and are photographed from the side. The ultrafast shutter is a Kerr cell where birefringence is induced directly by the short infrared pulses. The infrared pulses are horizontally polarised and induce a time dependant birefringence.

L. Wang et al. (1991) proposed this method (Fig. 1.12) to get 2-D images through scattering media. This technique should be able to select the ballistic and snake-like photons from the too much scattered photons. They present images of a test bar chart behind a thin layer of breast tissue.

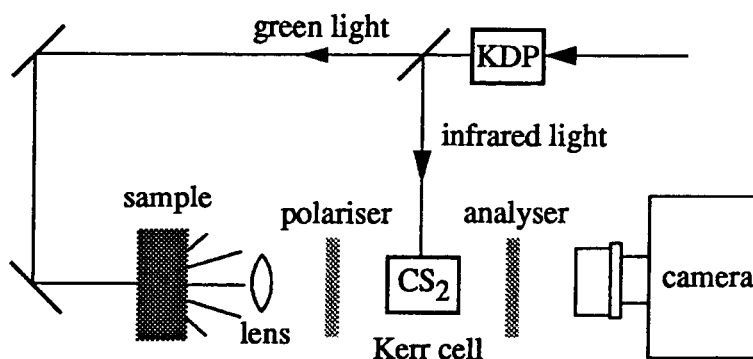


Fig. 1.12: experimental setting to visualise objects in turbid media with a Kerr cell.

### 1.5.6. Time-constraint imaging

Benaron et al. (1992) have developed an imaging technique based on time of flight and absorbance (TOFA imaging, Fig. 1.13). They measure the transit time and absorbance of a constant, early fraction of detected photons. In theory, the farther light travels through tissue, the more likely that the light has diffused randomly and contains little or no spatial information. Thus optical variations directly between emitter and detector disproportionately affect the intensity and transit time of these early arriving photons, and this change in transit delay can be used as an imaging variable. The device is based on a time-constrained, time of flight and absorbance, NIR multi-wavelength spectrophotometer. The imaging is divided into two functions, the detection and the localisation. With this

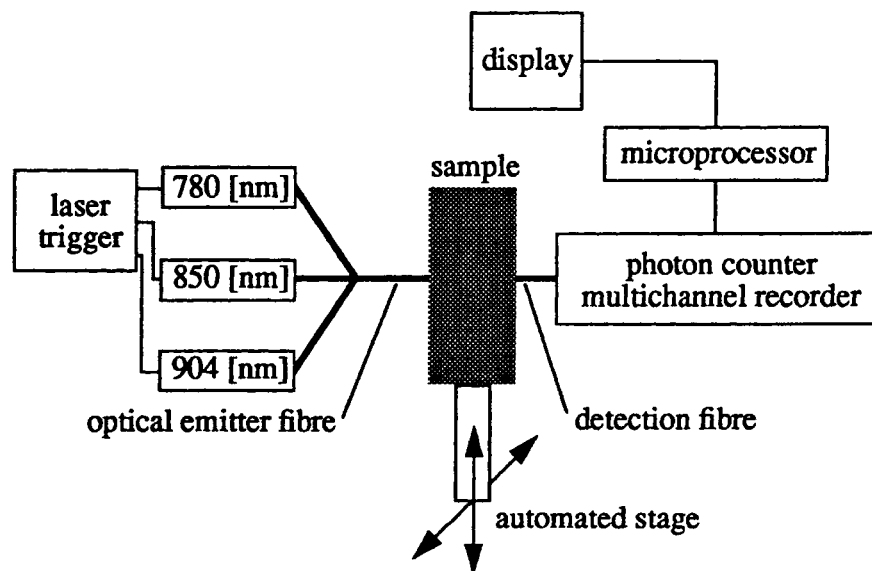


Fig. 1.13: multi wavelength spectrophotometre for time-constraint and absorbance imaging.

technique, imaging of scattering bodies, inanimate model systems as well as mammals, in which major organs are visible, have been made possible.

### 1.5.7. Discussion

The use of low coherence or holography principle for medical imaging with a laser source has to be proven in clinical conditions. In effect the experiments done by the different groups publishing in that subject have used phantoms made out of a solution of water with microspheres, milk colloidal suspension or oil

droplets suspension, which are far from biological tissues which are made out of tightly packed cells. The cytoplasmic membranes build a continuous border within the tissue creating a dense network of interfaces where photons are inevitably scattered, although colloidal solutions are made out of particles isotropically distributed in water, and photons could fly between the particles without collisions (Fig. 1.14). Others used thin layers of chicken meat which

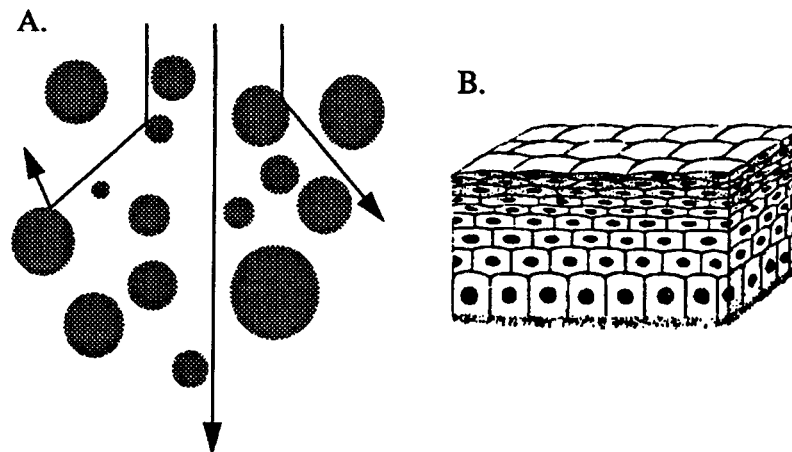


Fig. 1.14: schemes of a phantom sample (A.) made out of microspheres in water and a biological sample (B.) of epithelial structure.

appears to be poorly absorbent and scattering, thus an ideal sample for such experiments. The assumption that this technique would be totally useful for clinical situation (i.e. tissue thickness  $>10$  [mm]) is not possible only on the basis of a few selected experimental settings.

The use of real time gating is more versatile because the time gate is easily modified to get the optimal conditions for imaging. The modulation with an ultrafast Kerr cell is however not a practical solution, since the green light which should be used for the transillumination is greatly absorbed by tissues and so the images would be strongly blurred. Furthermore, the average power for such experiment is far too high, being round  $10^7$  [W] peak power for 10 [ps] pulses, necessitating powerful laser sources.

We would like then to propose a gating technique based on an ultrafast travelling wave amplitude modulator (in the GHz frequency range) and a detector which is a low light level IR CCD camera.



## CHAPTER 2

# ***ANALYTICAL MODEL***

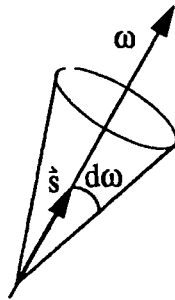
Three different approaches could be considered for modelling and describing the propagation of light in media that are both scattering and absorbing. The first approach could be the solving of Maxwell equations in the electromagnetic multiple scattering case (Ishimaru, 1977, Twersky, 1979). Furthermore, one can apply the models derived from radiative transfer theory applying approximate solutions to the Boltzmann transport equation (Ishimaru, 1978, van de Hulst, 1980, Groenhuis et al., 1983, Grossweiner et al., 1990). The last possibility is a numerical simulation on the basis of the Monte-Carlo methods. These three methods should be able to give an accurate description of the photon history through a biological tissue.

The Maxwell equations approach assumes that the medium has a permittivity which undergoes temporal and spatial fluctuations about a mean value. Via the material equations, the differential or integral equations for statistical quantities describing the electromagnetic fields can be derived. Although in principle mathematically rigorous, the electromagnetic approach has not yet been widely

used in tissue optics, since the application of Maxwell's equations in non-homogeneous media such as tissue is difficult and measurements of the dielectric quantities required in this method have not yet been published for tissue. Further the wavelength dependency of scattering (Mie theory) should be used to get the influence on the fluctuations. So in practice approximations have to be made to get useful results (Ishimaru, 1977, 1978, Twersky, 1979).

## 2.1. Optical coefficients

The “système international d’unités” (SI) will be used, unless specified when other units are expressed for convenience or reference to published results. Before presenting the optical coefficients, it is useful to define the elements describing the light field (photon field) in the medium.



- The *angular current*  $\vec{F}(\hat{r}, \hat{s})$  is defined as the energy carried by photons propagating in an elemental solid angle  $d\omega$  about a direction  $\omega$  through a region of unit area positioned at  $\hat{r}$ .
- The *angular flux*,  $L(\hat{r}, \hat{s})$  is defined as the modulus of the energy carried by photons propagating in an elemental solid angle  $d\omega$  about a direction  $\omega$  through a region of unit area positioned at  $\hat{r}$ . Also  $L(\hat{r}, \hat{s}) = |\vec{F}(\hat{r}, \hat{s})|$ . The net current at  $\hat{r}$  can be defined as  $\vec{F}(\hat{r}) = \int_{4\pi} L(\hat{r}, \hat{s}) \hat{s} d\omega$ .
- The *average flux*  $U(\hat{r})$  at  $\hat{r}$  is defined as  $U(\hat{r}) = \frac{1}{4\pi} \int_{4\pi} L(\hat{r}, \hat{s}) d\omega$ .

In order to make comparisons between the analytical model and the numerical computation where results are given in amount of photons, it is necessary to reduce the above mentioned concepts to a quantity of photons instead of energy. The relationship is known as a proportional factor  $h\nu$  ( $h$  is the Planck constant

and  $\nu$  is the frequency) for a monochromatic source.

The three fundamental optical interaction coefficients characterising a medium are the *absorption coefficient*  $\Sigma_a$ , the *scattering coefficient*  $\Sigma_s$  and the (single scattering) *phase function*,  $p(\hat{s}, \hat{s}')$ .

The absorption and scattering coefficients, within the confines of the radiative transfer theory, represent the probability per infinitesimal pathlength for a photon to be absorbed or scattered.  $\Sigma_s$  is the integral of the differential scattering coefficient  $\frac{d}{d\omega}\Sigma_s(\omega \rightarrow \omega')$ , which represents the probability per infinitesimal pathlength per unit solid angle of scatter from solid angle  $\omega$  to  $\omega'$ . When the scattering coefficient is independent of incident photon direction (as usually assumed in tissue optics)  $(\omega \rightarrow \omega')$  may be replaced by  $\hat{s} \cdot \hat{s}'$ , which is the cosine of the angle between the incident and scattered photon directions.

The phase function  $p(\hat{s}, \hat{s}')$ , which describes the angular dependence of the scatter, is often used in radiative transfer theory, and is derived from the differential scattering coefficient by

$$p(\hat{s}, \hat{s}') = \frac{1}{\Sigma_s} \cdot \frac{d}{d\omega}\Sigma_s(\hat{s} \cdot \hat{s}') \quad \text{Eq. 2.1}$$

The phase function is assumed to have a cylindrical symmetry around the direction  $\omega$ , of the incident photon.

Three other encountered parameters are the reduced scattering coefficient  $\Sigma_s'$ , the extinction coefficient  $\Sigma_t$  and the average cosine of scattering or anisotropy parameter  $g$ . These parameters can be derived from the fundamental interaction coefficients (Eq. 2.2).

$$\begin{aligned} \Sigma_s' &= \Sigma_s \cdot (1 - g) \\ \Sigma_t &= \Sigma_s + \Sigma_a \\ g &= \frac{\Sigma_s}{\Sigma_s + \Sigma_a} \end{aligned} \quad \text{Eq. 2.2}$$

Finally, there is another coefficient which is not an interaction parameter, this is the effective attenuation coefficient  $\Sigma_{\text{eff}}$  defined as  $\Sigma_{\text{eff}} \cong \sqrt{3\Sigma_a(\Sigma_a + \Sigma_s')}$ .

## 2.2. Analysis of light transport

The description of light distribution in biological tissues has been puzzling a host of investigators who have reported numerous values for the transport coefficients

of tissues. The exact analysis of light transport should lead to the three parameters  $\Sigma_s$ ,  $\Sigma_a$  and  $p(\hat{s}, \hat{s}')$ , which are required to be able to give an accurate characterisation of biological tissues.

The most simple description of the light transmission through a turbid medium is the simple exponential behaviour known as the Beer's law describing the unscattered transmitted light  $I(z) = I_0 \cdot e^{-(\epsilon \cdot z)}$ , where  $I_0$  is the total incident intensity,  $I(z)$  the transmitted intensity at  $z$  and  $\epsilon$  the extinction coefficient formerly accepted as  $\epsilon = \Sigma_a + \Sigma_s$ . This model necessitates a point-like collimated beam, normally incident on a slab, neither reflection at the surface, nor the scattering effect are considered far from the optical axis nor the backscattering. The determination of the coefficients is difficult when surface reflection is present, necessitating a correction which is required for all mismatched surfaces. For a sample placed between two glass plates the beam is reflected at the air-plate, plate-sample, sample-plate, plate-air and for thin samples, internal multiple reflections have to be considered, thus making this model difficult to use for accurate results. Further, the unscattered light is hardly detectable for optically thick samples. However, this model has been applied in oximetry (assuming  $\epsilon = \Sigma_a$  as a rough simplification) with success (Gordy and Drabkin, 1957, Taylor, 1986, Hazeki et al., 1987, de Haller and Depeursinge, 1991).

A model assuming multiple scattering has to be considered to get an accurate description of light transport through tissues. For this task, some assumption have to be done in order to simplify the theoretical solving of the equations from the theory of multiple scattering radiative transfer.

The properties related to the wave component of light, such as interference or diffraction as well as polarisation, are ignored. In some situations where the medium is sufficiently thin (a few mfp) or poorly scattering ( $\Sigma_s \ll \Sigma_a$ ), these properties should be considered, but in this work, the tissue-like multiple scattering condition precludes them. The scattering is assumed as elastic and fluorescence is negligible. Furthermore, the absorption and scattering process are assumed as linear, so no multiphoton absorption occurs. Finally the samples considered in this work are assumed to be optically homogeneous and have an isotropic random distribution of scatterers and absorbers.

An analytical model widely used is known as the two-flux Kubelka-Munk model described by P. Kubelka and F. Munk (1931) and later by P. Kubelka (1948) (see also appendix A.3). The K-M model has been found to be formally identical to the solution of the source free transport equation of radiative transfer (van Gemert and Star, 1987) for a scattering phase function consisting of the sum of a forward peak and an isotropic part (Wilson et al., 1986). This model is applied to slab samples where the photons are propagating parallel and counter-parallel to a given diffuse incident infinitely extended source. P. Kubelka (1948) completed the model with isotropic scattering. With some extensions, this model could be used with anisotropic scattering conditions (Marijnissen and Star, 1985). The value of the absorption coefficient  $K$  and the scattering coefficient  $S$  are proportional to  $\Sigma_a$  and  $\Sigma_s$ :  $K = 2\Sigma_a$  and  $S = \Sigma_s$  (Patterson et al., 1988) and for real tissues where  $\Sigma_a \ll \Sigma_s'$ ,  $K = 2\Sigma_a$  and  $S = \frac{1}{4} (3\Sigma_s' - \Sigma_a)$ . The K-M model is widely used for the characterisation of biological tissues and seems to be the most accurate method to determine the optical coefficients of a given tissue (van Gemert et al., 1987, 1988).

### 2.3. The diffusion model

Considering the Boltzmann equation (see also appendix A.4 and A.5 for detailed development) which express the balance of the flux in a volume  $dV$  (stationary case)

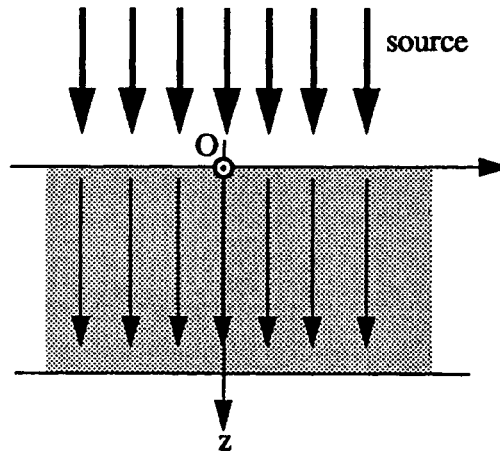
$$\hat{s} \nabla L(\hat{r}, \hat{s}) = -\Sigma_t L(\hat{r}, \hat{s}) + \Sigma_s \int_{4\pi} p(\hat{s}, \hat{s}') L(\hat{r}, \hat{s}') d\omega + S \quad \text{Eq. 2.3}$$

the left term is the variation of the flux, the first term at the right describes the losses due to scattering and absorption, the second term the gain due to photons scattered in the  $s$  direction and  $S$  express the source term.

In the case of biological tissues, with strong scattering ( $\Sigma_s \gg \Sigma_a$ ) and a phase function combining a strongly forward scattering (delta function) and isotropic scattering, the solution of the equation for light transmission in the  $z$  direction is:

$$L(z) \cong L_0 \cdot e^{-(\Sigma_{\text{eff}} \cdot z)} \quad \text{Eq. 2.4}$$

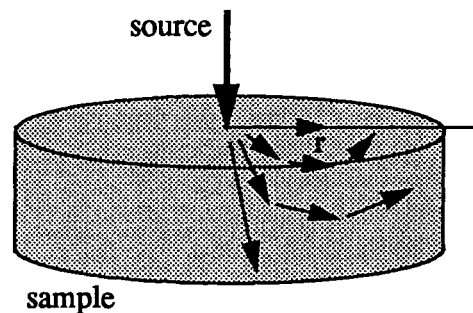
where  $z$  is the tissue thickness.



And for backscattered light in a thick sample:

$$L(r) \equiv \frac{L_0}{\sqrt{r}} \cdot e^{-(\Sigma_{\text{eff}} \cdot r)} \quad \text{Eq. 2.5}$$

where  $r$  is the radial distance from the source.



## 2.4. Location of a spherical object

The location of an object within a turbid medium is made possible by the calculation of the perturbation of transmitted light by an object within a slab (den Outer, 1992). With an object much smaller than the sample size, it is possible to determine the disturbance on the diffuse intensity. This is made possible by considering that diffusion inside the object is different from the diffusion of the surrounding medium. Solving the Laplace equation for a 3-dimensional semi-infinite slab of thickness  $z_{\text{max}}$  containing a spherical object of radius  $r_0$  at thickness  $z_0$ , homogeneously illuminated on its upper surface (Fig. 2.1), one could determine the output intensity profile and predict the position of the object. The calculation is done by introducing the analog of charges, dipoles and their mirror image used in the formalism of electrodynamics (see also appendix A.6).

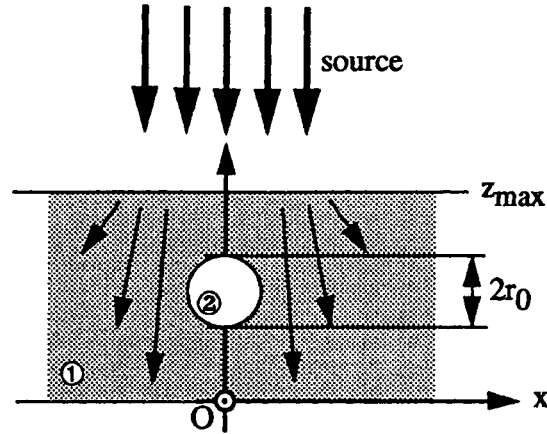


Fig. 2.1: lateral view of the object enclosed in the sample.

The stationary diffusion equation for the sample is the Laplace equation:

$$\nabla^2 I(\hat{r}) = 0 \quad \text{Eq. 2.6}$$

with the boundary conditions:

$$I(x, y, z_{\max}) = S(x, y) \quad I(x, y, 0) = 0 \quad \text{Eq. 2.7}$$

$I(\hat{r})$  being the incident diffuse intensity.

The diffusion equation inside the absorbing object is:

$$\nabla^2 I(\hat{r}) = \kappa^2 I(\hat{r}) \quad \text{Eq. 2.8}$$

To get the transmitted light, one should solve Eq. 2.6 and Eq. 2.8 with the boundary conditions set in Eq. 2.7.

The equation describing the transmitted light within the diffusion approximation for an absorption much smaller than the scattering (as it is expected in biological tissues) would be:

$$T(x, y, \text{mfp}) = \frac{\text{mfp}}{z_{\max}} + 2a \cdot \text{mfp} \cdot \sum_{i=-\infty}^{\infty} \frac{z_0 + 2iz_{\max}}{((z_0 + 2iz_{\max})^2 + |\hat{r}|^2)^{3/2}} + 2s \cdot \text{mfp} \cdot \sum_{i=-\infty}^{\infty} \frac{|\hat{r}|^2 - 2(z_0 + 2iz_{\max})}{((z_0 + 2iz_{\max})^2 + |\hat{r}|^2)^{5/2}} \quad \text{Eq. 2.9}$$

where the first term describes the unscattered light, the second term the absorption and the third term the scattering (see also appendix A.6). If the object

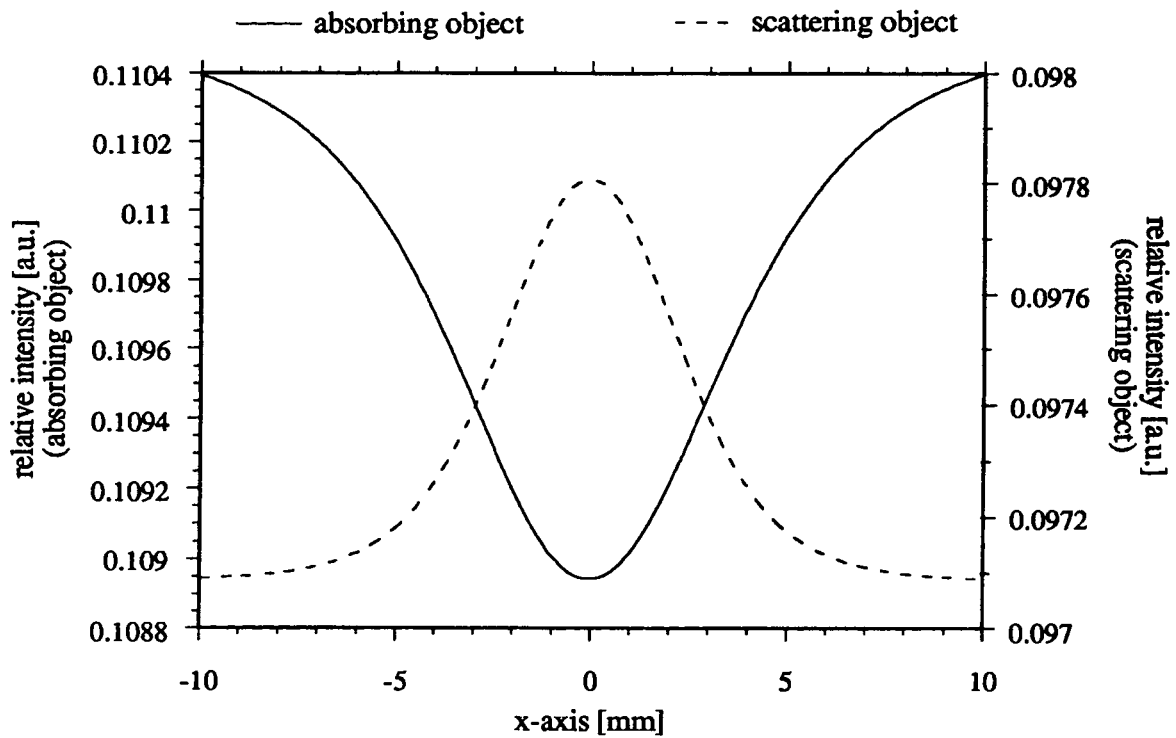


Fig. 2.2: plot of the transmitted intensity through a 10 [mm] thick tissue slab containing a spherical object of 2 [mm] set at 5 [mm] from the illuminated surface. The solid line is the signal of an absorbing object and the dashed line the signal of a purely scattering object.

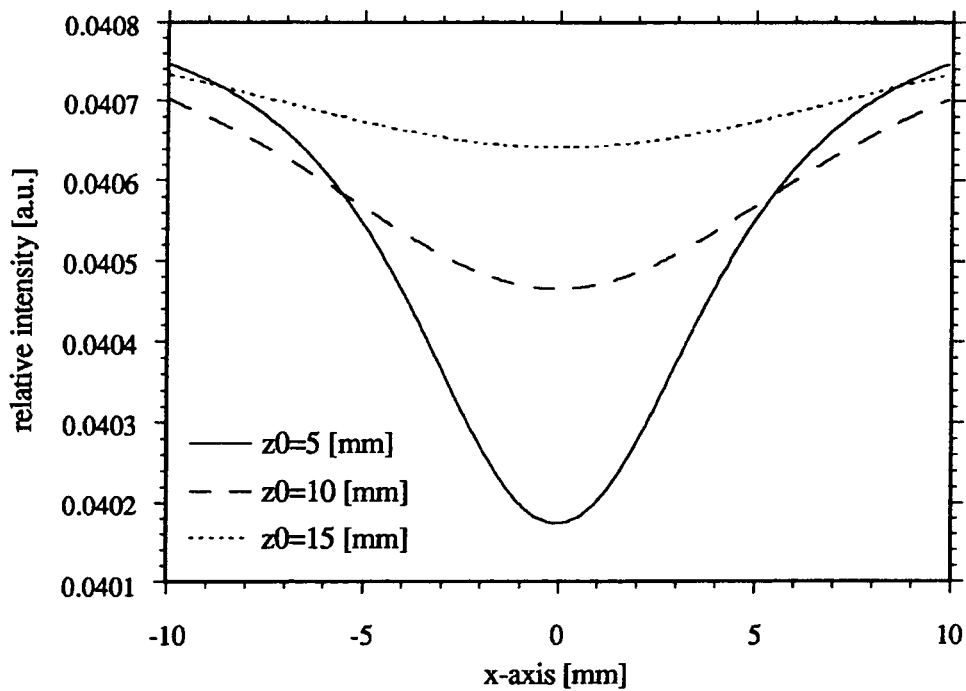


Fig. 2.3: plot of the intensity profile of a 2 [mm] absorbing sphere set at 5, 10 and 15 [mm] in a 20 [mm] thick slab of adipose.



does not absorb, the second term in Eq. 2.9 disappears. This particular solution to the Laplace equation necessitates a purely scattering medium, although the object could be either absorbing, scattering or both.

The analytical results for an absorbing and scattering spherical object embedded in a 10 [mm] thick slab of adipose have been computed according to Eq. 2.9 and are plotted in Fig. 2.2. Furthermore, to describe the influence of the object location (how far it is from the receiver), the analytical solution for an absorbing spherical object within a tissue slab has been computed also with Eq. 2.9 and displayed in Fig. 2.3. As expected, the profile grow sharper as the object is nearer to the receiver.

## 2.5. Pulse propagation

An arbitrary wavefunction  $u(\hat{r}, t)$  at a fixed position  $\hat{r}$  can be described as a superposition integral of harmonic functions (Eq. 2.10, Saleh and Teich, 1991).

$$u(\hat{r}, t) = \int_{-\infty}^{\infty} U_{\omega}(\hat{r}) e^{i\omega t} d\omega \quad \text{Eq. 2.10}$$

$$U_{\omega}(\hat{r}) = \int_{-\infty}^{\infty} u(\hat{r}, t) e^{-i\omega t} dt \quad \text{Eq. 2.11}$$

Since  $u(\hat{r}, t)$  is real,  $U_{\omega}(\hat{r})$  should be symmetrical so that  $u(\hat{r}, t)$  is the sum of a complex function and its conjugate (Eq. 2.12).

$$u(\hat{r}, t) = \int_0^{\infty} [U_{\omega}(\hat{r}) e^{i\omega t} + U_{\omega}^*(\hat{r}) e^{-i\omega t}] d\omega \quad \text{Eq. 2.12}$$

Thus, the complex wavefunction  $U(\hat{r}, t)$  (Eq. 2.13) is defined as twice the first term of Eq. 2.12.

$$U(\hat{r}, t) = 2 \int_0^{\infty} U_{\omega}(\hat{r}) e^{i\omega t} d\omega \quad \text{Eq. 2.13}$$

and the real part of it is the wavefunction  $u(\hat{r}, t)$  (Eq. 2.14).

$$u(\hat{r}, t) = \frac{1}{2} [U(\hat{r}, t) + U^*(\hat{r}, t)] \quad \text{Eq. 2.14}$$

So a polychromatic wave propagating in the  $z$  direction can be described by a superposition integral given by Eq. 2.15.

$$U(\vec{r}, t) = \int_0^{\infty} a_{\omega} e^{-ikz} e^{i\omega t} dt \quad \text{Eq. 2.15}$$

Where  $a_{\omega}$  is the complex envelope of the component of frequency  $\omega$  and wavenumber  $k$ . If the wave is of finite duration  $\sigma_t$ , then the wave is a pulse travelling in the  $z$  direction and the wavepacket extends over  $\sigma_z = \sigma_t \cdot c$  and if the pulse intensity  $I(\vec{r}, t) = |U(\vec{r}, t)|^2$  is Gaussian with a FWHM of  $\sigma_t$ , its spectral bandwidth is given by  $\sigma_{\omega} = \frac{1}{4\pi\sigma_t}$ .

As a general formulation for the pulse propagation, it is adequate to speak about the incident pulse  $v_i(t)$  and the detected pulse  $v_d(t)$  which are both real functions (Ishimaru, 1978). The function  $v_d(t)$  is then the convolution of the function  $v_i(t)$  by the impulse response  $h(t, t')$  (Eq. 2.16).

$$v_d(t) = \int_{-\infty}^{\infty} v_i(t') h(t, t') dt' \quad \text{Eq. 2.16}$$

A light pulse is assumed as a polychromatic wave and can be expanded as a sum of monochromatic waves by Fourier decomposition (Eq. 2.17).

$$v_i(t) = \int_{-\infty}^{\infty} V_i(\omega) e^{-i\omega t} d\omega \quad \text{Eq. 2.17}$$

So that the detected pulse  $v_d(t)$  is also a convolution (Eq. 2.18).

$$v_d(t) = \int_{-\infty}^{\infty} V_i(\omega) H(\omega, t) e^{-i\omega t} d\omega \quad \text{Eq. 2.18}$$

$H(\omega, t)$  is the output function when the input is a time-harmonic function  $e^{-i\omega t}$ . The incident pulse  $v_i(t)$  could be expressed through the real part of its complex envelope  $a_i(t)$  (Eq. 2.19).

$$v_i(t) = \text{Re} [a_i(t) e^{-i\omega_0 t}] \quad \text{Eq. 2.19}$$

$\omega_0$  is defined as the carrier frequency. Similarly, the detected pulse is described by its complex envelope  $a_d(t)$ . Furthermore, the complex envelope could be decomposed by Fourier integral (Eq. 2.20).

$$a_i(t) = \int_{-\infty}^{\infty} A_i(\omega) e^{-i\omega t} d\omega \quad \text{Eq. 2.20}$$

Thus the incident spectrum  $V_i(t)$  is given by the sum of the complex envelope spectrum and its complex conjugate (Eq. 2.21).

$$V_i(\omega) = \frac{1}{2} [A_i(\omega - \omega_0) + A_i^*(-\omega - \omega_0)] \quad \text{Eq. 2.21}$$

Finally the detected pulse  $v_d(t)$  could be expressed in the form of Eq. 2.19 with

$$a_d(t) = \int_{-\infty}^{\infty} A_i(\omega) H(\omega_0 + \omega, t) e^{-i\omega t} d\omega \quad \text{Eq. 2.22}$$

The fluctuations of the detected pulse are described by the correlation function of the complex envelope (Eq. 2.23 and Eq. 2.24).

$$B(t_1, t_2) = \langle a_d(t_1) a_d^*(t_2) \rangle \quad \text{Eq. 2.23}$$

$$B(t_1, t_2) = \int_{-\infty}^{\infty} d\omega_1 \int_{-\infty}^{\infty} d\omega_2 A_i(\omega_1) A_i^*(\omega_2) \Gamma e^{-i\omega_1 t_1 + i\omega_2 t_2} \quad \text{Eq. 2.24}$$

where  $\Gamma$  is the correlation of the detected field due to the time harmonic incident fields at two frequencies  $\omega_0 + \omega_1$  and  $\omega_0 + \omega_2$  (Ishimaru, 1978). In a random turbid medium the propagation and scattering of a pulse  $I(t)$  could be described by the two-frequency correlation function  $\Gamma$  or two frequency mutual coherence function (Eq. 2.25).

$$\Gamma = \Gamma(\omega_0 + \omega_1, \omega_0 + \omega_2, t_1, t_2) = \langle H(\omega_0 + \omega_1, t_1) H^*(\omega_0 + \omega_2, t_2) \rangle \quad \text{Eq. 2.25}$$

This formulation lead to the description of a wave propagation through the coherence time and the coherence bandwidth. For a wave propagating at the frequency  $\omega$ , the output fluctuates in time and the correlation of the output wave at time  $t_1$  and  $t_2$  decreases as the difference  $\tau = t_1 - t_2$  increases. The time difference  $\Delta t$ , when the correlation disappears or decreases to a given level, is the coherence time. This is an objective measure of the correlation of a wave in time. In the case of two waves propagating at frequencies  $\omega_1$  and  $\omega_2$ , the correlation of the fluctuation decreases as the frequencies are separated. The frequency difference  $\Delta f = \omega_{\text{coh}}$ , when the correlation disappears or decreases to a given level, is the coherence bandwidth and gives an objective measure of the correlation of two waves. The inverse of the coherence bandwidth is the pulse width. Generally  $\Gamma$  is stationary in time (Ishimaru, 1978).

To describe the pulse transport let us consider an incident pulse  $I_i(t)$  propagating through a turbid medium with randomly distributed scatterers. The pulse is then determined by its impulse response  $G(t)$  to the delta function with the

convolution integral (Eq. 2.26).

$$I(t) = \int G(t-t') I(t') dt' \quad \text{Eq. 2.26}$$

$I(t)$  is the output pulse,  $G(t)$  is the inverse Fourier transform of the two-frequency correlation function  $\Gamma$  evaluated at  $t_1 = t_2 = t$ .

In the case of strong fluctuation (or when the incoherent component of the wave dominates the coherent component, as in tissues with  $\Sigma_s \gg \Sigma_a$ ) we have:

$$G(t) = \left(\frac{\pi\omega_{\text{coh}}}{4}\right) \sum_{n=0}^{\infty} (2n+1) (-1)^n \exp\left\{-\left[(2n+1) \cdot \frac{\pi}{4}\right]^2 T\right\} \quad \text{Eq. 2.27}$$

with  $T = \omega_{\text{coh}}(t-z/c)$ . Eq. 2.27 is the universal form of the impulse response displayed in Fig. 2.4 (Ishimaru, 1978). The pulse width  $T_s$ , which is function of

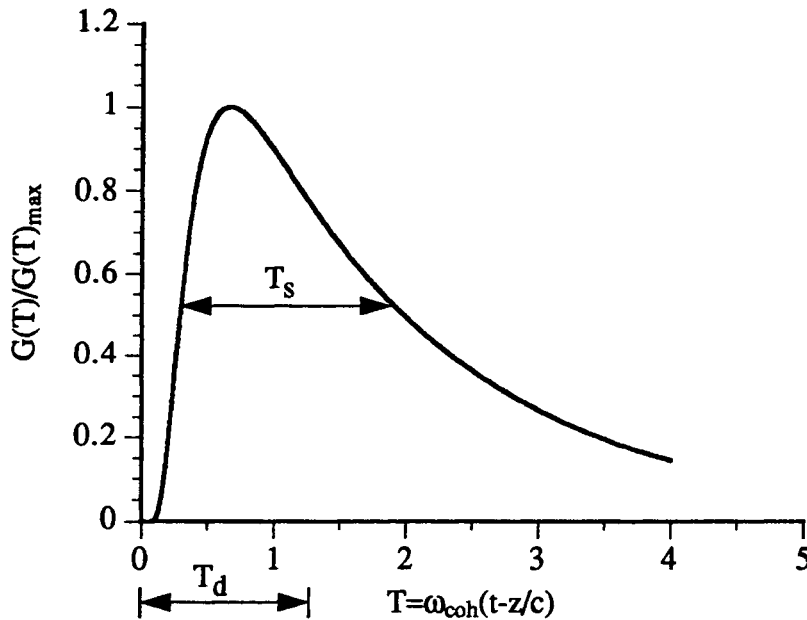


Fig. 2.4: universal form of the pulse shape applicable to a wide variety of physical situations.

the square of the slab thickness for strong fluctuations, is given as  $\omega_{\text{coh}}^{-1}$  and the delay time  $T_d$  is a function of  $T_s$  (Ishimaru, 1978). The peak of the output pulse appears at  $\frac{1}{4}T_d$ . The coherent intensity (delta function) appearing on the 0 of the time scale is neglected in the case of tissue scattering.

In the diffusion approximation, one can settle the decay of the coherent part of the signal in function of the thickness and the optical properties of the sample. The temporal displacement between the coherent (dirac) and the incoherent peaks decrease as the scatterer density get lower and the sample thickness

diminishes (Eq. 2.28 and Fig. 2.5).

$$\frac{L_{\text{coh}}}{L_{\text{trans}}} = \frac{1}{1 + (a \cdot (e^{n\Sigma_s z} - 1)) / (1 + n\Sigma_m z)} \quad \text{Eq. 2.28}$$

$L_{\text{coh}}$  is the coherent flux,  $L_{\text{trans}}$  the total transmitted flux,  $a$  the solid angle of photon collection,  $n$  (unitless) the density of scatterers and  $\Sigma_m$  the momentum transfer scattering cross section calculated by Mie theory (Ishimaru, 1978, Yoo and Alfano, 1990). In the case of biological tissues, the coherent part is almost nonexistent for a sufficient thickness ( $>10$  [mm]). The high density of scatterers as well as the high scattering property of tissues tend to eliminate the coherent part of the signal. The extinction factor  $\epsilon$  in  $I_{\text{coh}}(z) = I_0 \cdot e^{-\epsilon z}$  for the coherent output intensity in the NIR range is in the range from 1.9 to 9 [ $\text{mm}^{-1}$ ] for biological tissues (Clivaz, 1992, Clivaz et al., 1992, Wilson, 1992).

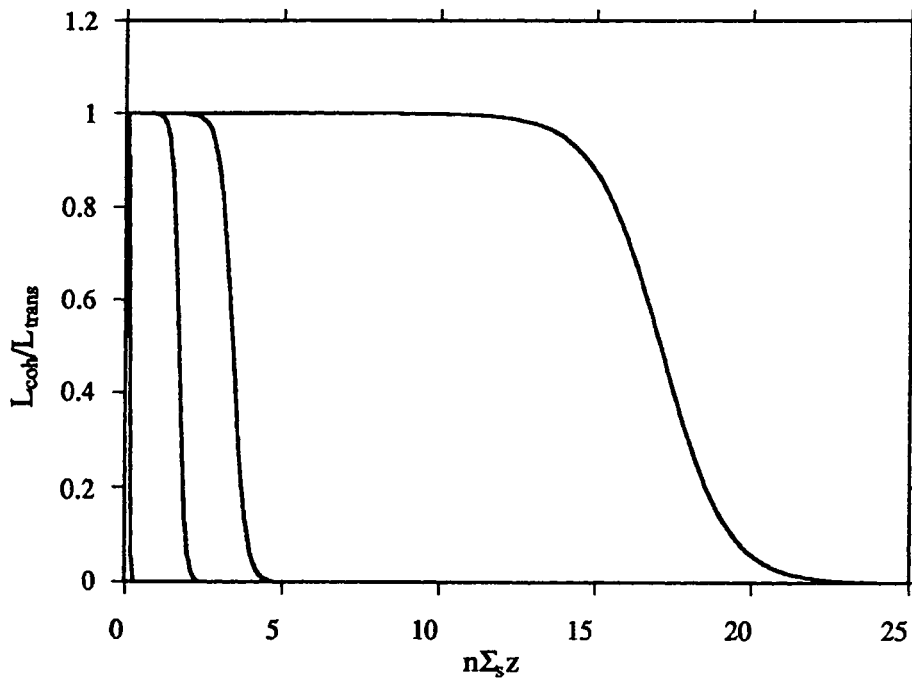


Fig. 2.5: plot of the ratio of the transmitted coherent flux and the total transmitted flux in function of  $n\Sigma_s z$ . From left to right the curves are plotted in function of decreasing  $\Sigma_s$ .

## 2.6. Phase function

The choice of a phase function is very important in any calculation on multiple scattering. In a well defined physical problem, the phase function is given and not chosen (van de Hulst, 1980). Exact phase function consideration will lead in

practice to time consuming computing or oblige one to use approximate methods to calculate multiple scattering. It is preferable to use in a simpler phase function, which although preserves the main properties of the more complex function (i.e. the anisotropy) and allows an easier computation. It is often possible to replace a complex phase function by a simpler one without changing its effect on multiple scattering phenomenon.

The phase function of tissues involves the estimation of the angular dependence of the light scattered by a thin slab of tissue. The evidence is that the light scattering in tissues is forward peaked and anisotropic (Kullenberg, 1974, Fine et al., 1985, Flock et al., 1987, van Gemert et al., 1988, Flock, 1991). The phase function usually used to approximate the description of tissue scattering is the one presented by L.G. Henyey & J.L. Greenstein (1941, Eq. 2.29 and Fig. 2.6).

$$p(\hat{s}, \hat{s}') = p(\hat{s} \cdot \hat{s}') = \frac{1}{4\pi} \cdot \frac{1 - g^2}{\sqrt{(1 + g^2 - 2g\hat{s} \cdot \hat{s}')^3}} \quad \text{Eq. 2.29}$$

This phase function varies smoothly from isotropic ( $g=0$ ) to a narrow forward peak ( $g=1$ ) or to a narrow backward peak ( $g=-1$ ). At each  $g>0$ , the function

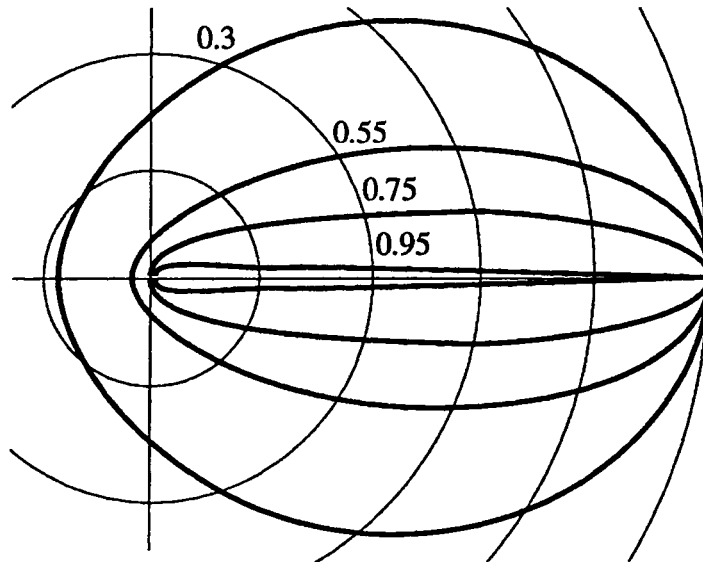


Fig. 2.6: polar plot of the H-G phase function, normed to 1, for  $g=0.3, 0.55, 0.75$  and  $0.95$

increases uniformly from the backward direction to the forward direction. This makes the H-G phase function ideal for calculation on multiple scattering in

which the influence of anisotropy has to be determined with a one-parameter equation. Furthermore, the H-G phase function resembles those computed on the basis of the Mie theory for particles whose radius is near the wavelength (Henyey and Greenstein, 1941).





## CHAPTER 3

# ***NUMERICAL METHOD***

In the 1930's, Enrico Fermi made some numerical experiments (that would now be called Monte-Carlo simulations) for studying the behaviour of the newly discovered neutrons. During the 1940's, the scientists working on the Manhattan project at Los Alamos developed a class of mathematical methods which were called the Monte-Carlo method.

The Monte-Carlo method enables the description of a purely stochastic phenomenon, i.e. a sequence of states determined by random single events. But the average behaviour of such phenomenon can also be described by mathematical equations. By this way a non-probabilistic problem could be solved with a probabilistic method. A Monte-Carlo simulation brings a numerical solution on the basis of mathematical equations. Such a simulation could be considered as a "natural simulation" or as a solution of the equations by random sampling.

The central topic in the development of a model of light propagation in tissues is the precise prediction of the spatial distribution of photons. The single events are

determined by interactions of photons with tissue where scattering and absorption take place. Scattering and absorption occur randomly along the path of photons, but the average of a large number of photons leads to the expected result. Thus, following the trajectory of enough photons to avoid strong statistical variation, the behaviour of light could be determined accurately. The use of a Monte-Carlo simulation to determine the behaviour of photons in tissues is valid within the condition that scattering occurs independently one of another, i.e. the scattering of a photon is not within a wavelength of the previous scattering event.

### 3.1. Simulation of light propagation through tissues

A simulation of the behaviour of photons within tissues enables the fair understanding of the transillumination imaging technique and a useful methodology in the domain of the time-gating effect. The simulation is a Monte-

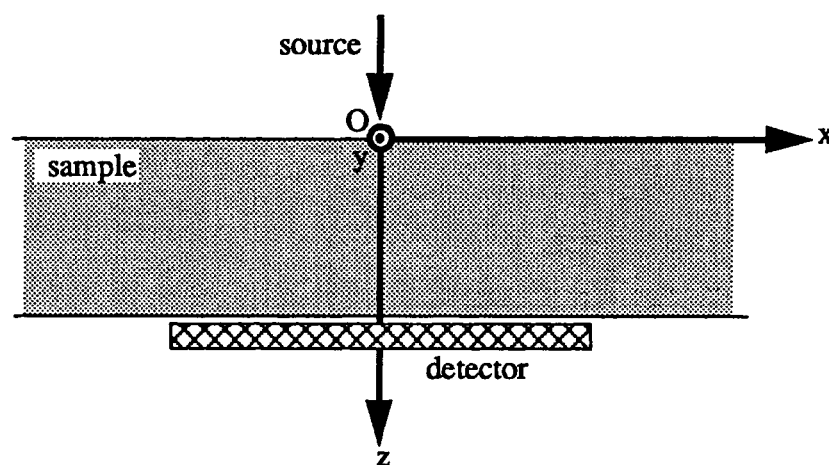


Fig. 3.1: physical elements of the simulation setting projected on the  $(x,z)$ -plane.

Carlo one combining the purely stochastic behaviour of photons and the deterministic physical law describing the multiple scattering of light. The light intensity is assumed to be due to equal-energetic photons. The photon is assumed to be a dimensionless particle travelling through tissues. The wave component of the photon is neglected. The simulation process computes the 3-D trajectory of a large number of photons. This trajectory is only modified by absorption and

scattering. These events or interactions occur randomly along the path and are determined by the absorption condition and the phase function. Each photon follows a free path between each interactions. Scattering is mainly due to interfaces and cell components, and absorption to chromophores such as haemoglobin (see also appendix A.1). The computing process includes the source, the sample and the detector geometries.

For convenience and because of cylindrical symmetry, the 3-D views are projected on the (x,z)-plane, the y-axis pointing out of the page (Fig. 3.1).

### 3.1.1. Source

The light source is assumed as a pulsed laser, each photon being emitted in the same direction with no divergence. The light is described by one pulse of photons normally incident on the upper surface of the sample. The pulse exhibits a Gaussian shape and is discretised, for numerical purpose, by the sum of 40 delta functions, the envelope of which determines the laser pulse (Fig. 3.2). At time  $t_0 = 0$  [ps] the Gaussian pulse which FWHM is 5 [ps] is emitted. Specular reflection and interface losses on the upper surface of the sample are neglected, meaning that all the photons in the pulse penetrate the sample.

The source is either a point source centred at O or a light cylinder with a diameter of 50 [mm], normal to the upper surface and centred at O (Fig. 3.3).

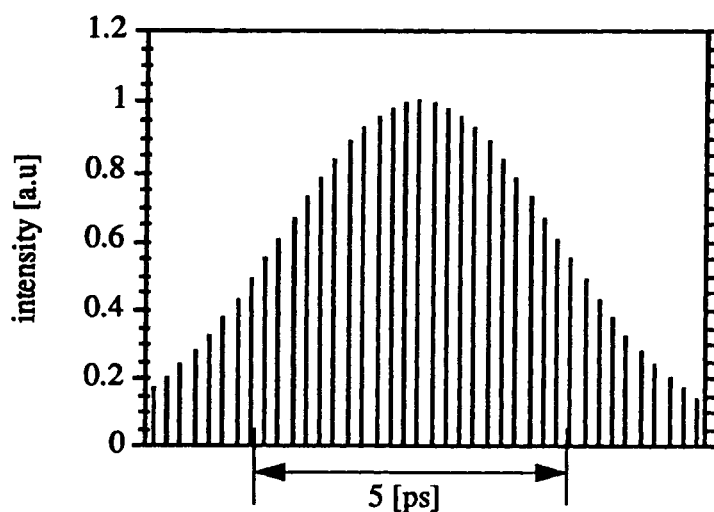


Fig. 3.2: discretisation of the laser pulse with 40 discrete infinitesimal pulses of photons. The maximal intensity was set in order to get  $10^6$  photons per pulse.

### 3.1.2. Sample

According to the model we chose, the sample is defined as a semi-infinite plane-parallel slab assumed as homogeneous tissue (Fig. 3.3). The dimensions of the

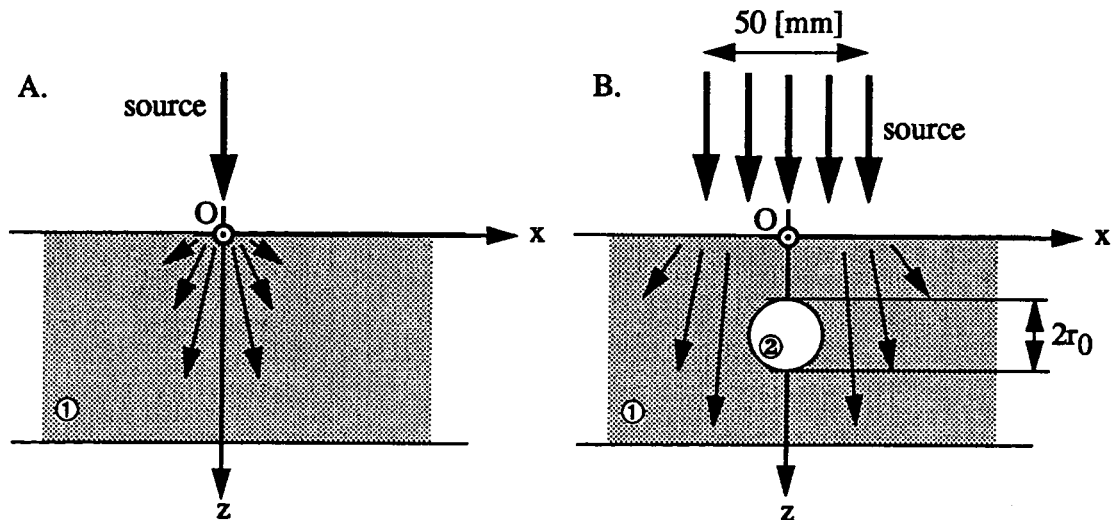


Fig. 3.3: simulation setting of the sample and the source, for a point source (A.) and for an expanded source (B.) illuminating the sample with a spherical carcinoma of radius  $r_0$  centred at a depth  $z_0$ .

slab are set with the plane  $(x,y)$  for the upper and lower surface and the thickness  $z$ , all in [mm]. The thickness is either 20 or 40 [mm] to satisfy clinical relevance. The tissue is assumed to be adipose (see Table 1). The carcinoma is simulated by a sphere of radius  $r_0$  located at a depth  $z_0$  within the sample, and the optical coefficients are those of carcinoma, given in Table 1.

### 3.1.3. Detector

The detector modelled is a perfect  $1 \times 1$  [cm<sup>2</sup>] CCD with  $512 \times 512$  pixels. Each

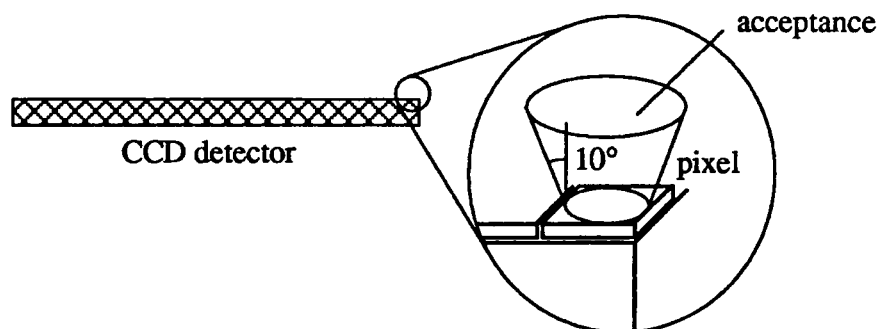


Fig. 3.4: simulation model of the CCD.

pixel is a square with 19.53 [ $\mu\text{m}$ ] sides. To add a spatial filter, the CCD has an acceptance angle of  $10^\circ$ . Each photon reaching the detector has a weight of 1.

### 3.2. Optical parameters

The optical parameters chosen for the simulation are mainly taken from literature where a lot of data have been collected for biological tissues. Generally the references have to be recent in order to have accurate data to compute realistic and clinical situations for reliable results. The average refractive index is set at 1.36 (Barer et al., 1953) (although other authors defined it as 1.4 (Flock, 1991)) which gives a speed of light  $c_n$  of 0.218 [ $\text{mm ps}^{-1}$ ]. The optical coefficients of tissues we used in our simulation were taken from Peters et al. (1990, Table 1) who examined bloodless biological tissue samples in vitro. The carcinoma appears then to be diffusing and the adipose absorbing. This difference from in vivo observation (Watmough, 1982) should be mainly due to the lack of tissue perfusion.

Tissue type	700 [nm]		900 [nm]	
	$\Sigma_a$ [ $\text{mm}^{-1}$ ]	$\Sigma_s$ [ $\text{mm}^{-1}$ ]	$\Sigma_a$ [ $\text{mm}^{-1}$ ]	$\Sigma_s$ [ $\text{mm}^{-1}$ ]
Glandular	0.047	28.4	0.062	19.8
Adipose	0.070	17.2	0.075	15.8
Fibrocystic	0.022	26.8	0.027	19
Fibroadenoma	0.052	14.4	0.072	10.6
Carcinoma	0.045	23.6	0.050	17.8

Table 1: mean value of the absorption coefficient  $\Sigma_a$  and the scattering coefficient  $\Sigma_s$  with  $g = 0.95$ , for each of five tissue types at wavelengths of 700 and 900 [nm] (from Peters et al., 1990).

The scattering angle for scattered photons has been calculated from the cumulative distribution derived from the phase function with an anisotropic factor  $g$  of 0.95 (Flock et al., 1987, Jacques et al., 1987, Jacques, 1989) which is a realistic value for biological tissues.

### 3.3. Image parameters

It is necessary to define the elements describing the image and the image formation. The three main image parameters used in the simulation are the *resolution*, the *contrast* and the *noise* (see also appendix A.8).

- The *resolution* is described by the modulation transfer function or MTF which is defined as:

$$\text{MTF}(f_x, f_y) = |\mathcal{F}(\text{PSF}(x, y))| \quad \text{Eq. 3.1}$$

- The *noise* is expressed through the Wiener spectrum (Dainty and Shaw, 1974). In the simulation, the Wiener spectrum was derived from the noise obtained by illuminating the entire detector from an expanded source of radius 25 mm through adipose tissue. Quantum noise and a term covering the speckle and anatomical noise were added. With the hypothesis of a Gaussian MTF(f) and a white noise, the Wiener spectrum could be expressed through the variance  $\sigma_A^2$  of the noise for an aperture A, or illuminated area A.

$$W(f) = A \cdot \sigma_A^2 \quad \text{Eq. 3.2}$$

- The *contrast* C was computed with the difference of transmission of two adjacent tissue samples of identical thickness. The optical density OD is expressed through  $\text{OD} = -\log(I/I_0)$  where I is the total transmitted intensity and  $I_0$  the total incident intensity. The temporal optical density  $\text{OD}_t$  is given as  $\text{OD}_t = -\log(I_t/I_0)$ , where  $I_t$  is the total transmitted intensity up to time t and  $I_0$  the total incident intensity. It depends on the system and the gating time. We used the contrast C defined as the difference of transmission per length unit. The reason of this expression will be explained in paragraph 3.5.5.

$$C = \frac{|\Delta\text{OD}|}{\Delta z} \quad \text{Eq. 3.3}$$

### 3.4. Simulation process

At time  $t_0 = 0$  [ps], the first photons of the pulse strike the upper surface of the sample. Each photon follows a random path length determined by the free path

length. The scattering length (see appendix A.7 for detailed development) and scattering angle are derived from their cumulative probability distributions. The drawing of a first random number  $\alpha_1$  leads to the free path  $L$  between two interactions (Eq. 3.4).

$$L = \frac{-\ln\alpha_1}{\Sigma_t} \quad \text{Eq. 3.4}$$

The probability of a free path length greater than the sample thickness is very small because of the large thickness  $z_{\max}$  of the sample compared to the mean free path  $L$  of a photon. A second random number  $\alpha_2$  is drawn and compared with the absorption condition  $W_{\text{abs}} = \Sigma_a/\Sigma_t$  (Wilson and Adam, 1983) and determines whether the photon is absorbed or scattered. If the photon is not absorbed, the drawing of a third random number  $\alpha_3$  gives the scattering angle derived from its cumulative probability distribution (Eq. 3.5. and Fig. 3.5).

$$\theta = \arccos \left\{ \frac{1}{2g} \left[ 1 + g^2 - \left( \frac{1 - g^2}{1 + g - 2g\alpha_3} \right)^2 \right] \right\} \quad \text{Eq. 3.5}$$

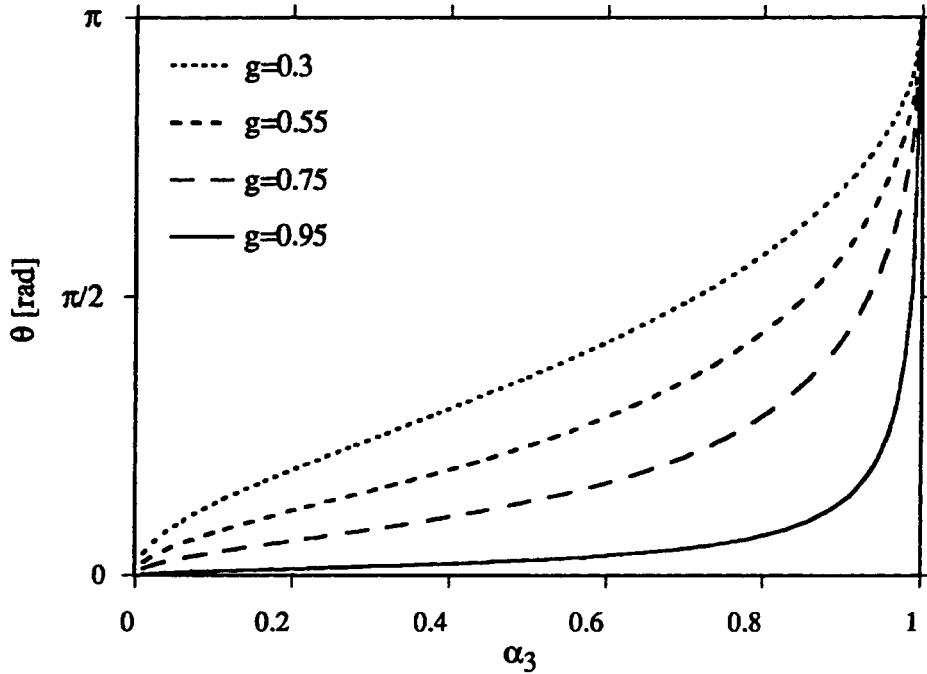
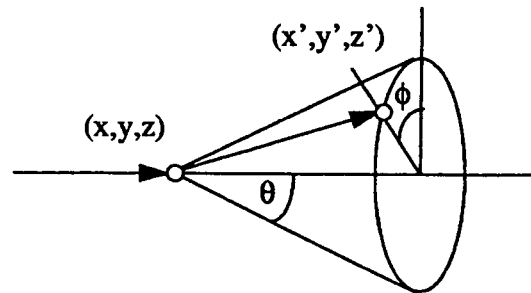


Fig. 3.5: cumulative probability of the H-G phase function for  $g=0.3$ ,  $g=0.55$ ,  $g=0.75$  and  $g=0.95$

Finally the drawing of a fourth random number  $\alpha_4$  will give the radial angle between  $0$  and  $2\pi$ . The temporary coordinates of the photons i.e. the location of

the interactions are computed with the equations (Eq. 3.6 and Eq. 3.7) presented by Kalos and Whitlock (1986).



$$CDx' = \frac{\sin \theta}{\sqrt{1 - CDz^2}} [CDy \cdot \sin \phi - (CDz \cdot CDx \cdot \cos \phi)] + CDx \cdot \cos \theta$$

$$CDy' = \frac{\sin \theta}{\sqrt{1 - CDz^2}} [CDx \cdot \sin \phi - (CDz \cdot CDy \cdot \cos \phi)] + CDy \cdot \cos \theta$$

$$CDz' = \sin \theta \cdot \sqrt{1 - CDz^2} \cdot \cos \phi + CDz \cdot \cos \theta \quad \text{Eq. 3.6}$$

$$x' = x + CDx' \cdot L$$

$$y' = y + CDy' \cdot L$$

$$z' = z + CDz' \cdot L$$

Eq. 3.7

If the total time for the photon history exceeds a chosen time  $t_f$ , the history is terminated and a new photon is considered. The last coordinates of the photon are stored.

We thought it would be relevant to add a term describing the anatomical and the eventual speckle noise to the quantum noise. Thus we decided to simulate this additional noise. The drawing of a fifth random number  $\alpha_5$  modulates the probability of presence of the photon assuming a probability density distribution. The allowed TOF  $t_f$  is given at the beginning of the computation and this choice simulates the selection of the photons which follow the shorter random path. Following Kruger et al. (1990) the gating time is defined as the difference between the TOF of a ballistic photon (or ballistic time  $t_b$ ) and the allowed TOF  $t_f$  of the photons. The amount of photons is greater than  $10^6$ , selected to reduce the statistical variations caused by a too small number of photons.



### **3.5. Results of the simulation**

First of all, the accuracy of the simulation has to be established. Actually a simulation could lead to erroneous results if admitted as an objective tool from the beginning. Some known parameters have to be controlled in order to assess the model and to determine what kind of errors are possibly met during simulation.

The Monte-Carlo program has been developed with the Pascal computer language to run on standard PC (IBM PC AT-286) for preliminary debugging and then passed to a more powerful calculator (Apollo DN-3500). The time requested for the determination of a single PSF is particularly long due to the Monte-Carlo process computing the path of every single photon. As an example, a photon travelling through adipose suffers around 20 interactions per travelled millimetre. Each interaction necessitates numerous complex operations (generation of four random numbers, computing of the free path length, the scattering angle and the radial angle, to finally get the new position of the photon if not absorbed), so a pulse of  $10^6$  photons travelling through 20 [mm] of tissue requires much more than  $5 \cdot 10^9$  complex operations. Thus controls of the drift from the initial parameters have to be done (see also appendix A.9). To get a time gain, the program has been then translated in C computer language and tests have been run again on a Motorola 68040 based Apollo DN-5500. The C language enabled a more accurate computing (less drift) and lead to a portable Monte-Carlo program (the program has been also compiled and tested on HP series 700, Silicon Graphics Iris and Cray 2 without any change in the code). The Cray logic necessitates a radical change in the Monte-Carlo program in order to avoid time consuming computing, so that the Cray 2 computer eventually was not used.

In order to confirm the accuracy of the Monte-Carlo computing, simple results of the simulation were compared to independent, exact calculations and to measures done on phantoms. The simulation was compared with published results of diffuse transmittance and reflectance by van de Hulst (1980) (Fig. 3.6 and Fig. 3.7) for two different slabs of 1 mfp and 4 mfp thickness.

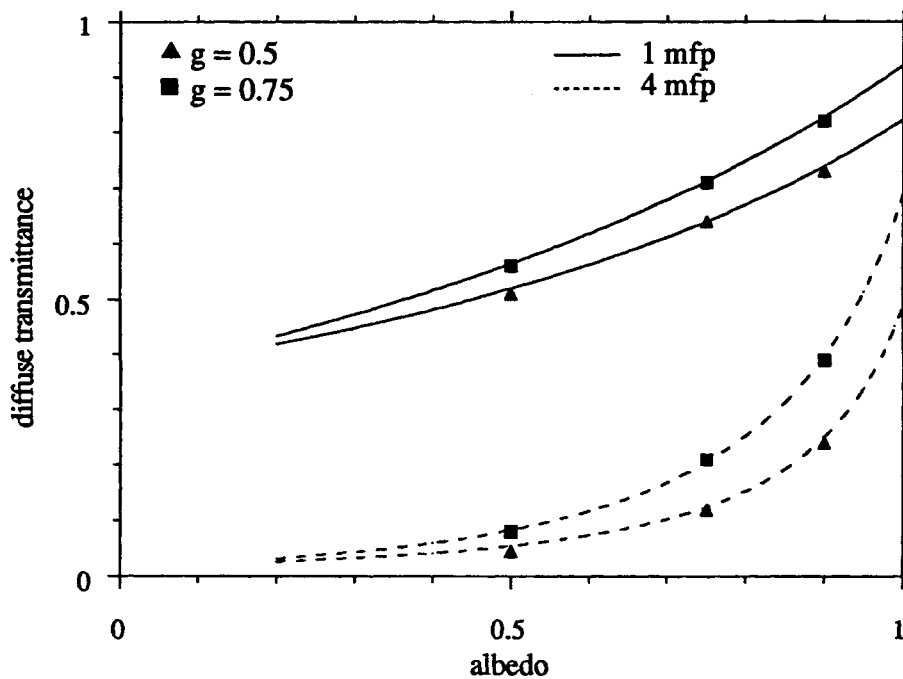


Fig. 3.6: diffuse transmittance computed with the Monte-Carlo simulation (data points) plotted with the lines connecting data of van de Hulst tables. The solid lines are for a 1 mfp thick slab and the dashed line for a 4 mfp thick slab.

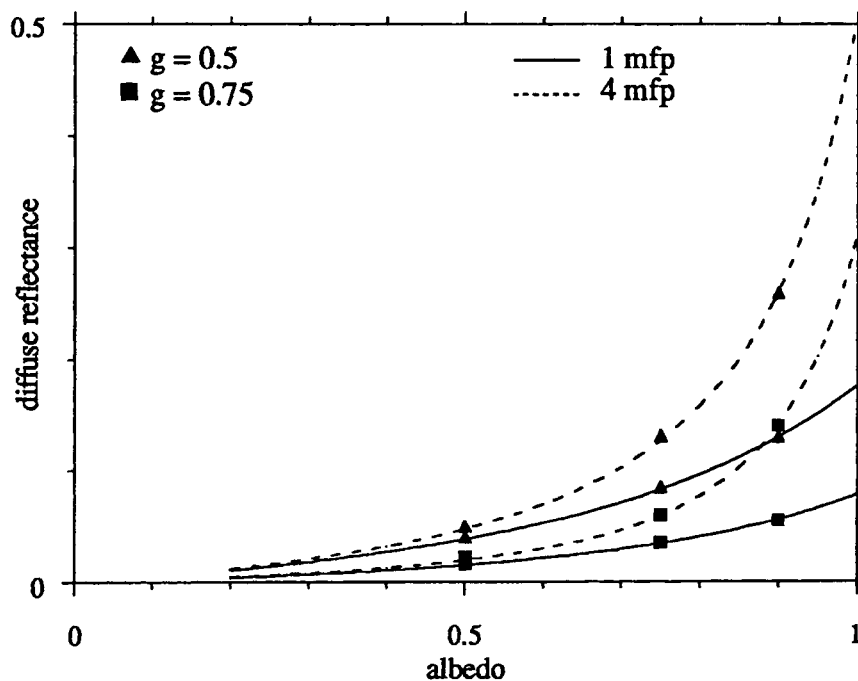


Fig. 3.7: diffuse reflectance computed with the Monte-Carlo simulation (data points) plotted with the lines connecting data of van de Hulst tables. The solid lines are for a 1 mfp thick slab and the dashed line for a 4 mfp thick slab.

Further comparisons were made with experimental results obtained on samples of a microsphere colloidal suspension in water (Bevilacqua et al., 1993, Marquet et al., 1993). Knowing the size and refraction index of the polystyrene microspheres, the exact microscopic optical characteristics of the microsphere suspension have been determined with Mie theory (program proposed by C.F. Bohren and D.R. Huffman, 1983). The colloidal suspension is set in a 5 [mm] cuvette and a laser diode (670 [nm]) illuminates the sample. A linear CCD detects the transmitted signal. The value of the amplitude  $H$  and the width  $L$  of the output signal are determined (Fig. 3.8). These two parameters are then

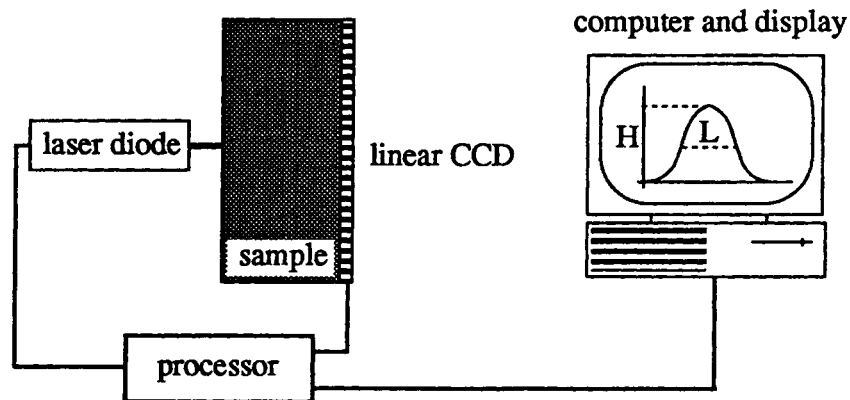


Fig. 3.8: experimental setting for the determination of the amplitude  $H$  and the width  $L$  of the signal through a sample of microsphere suspension.

compared to Monte-Carlo simulation results. The simulation assumes the same parameters as the experimental setting: the incident beam size, divergence and intensity, the optical coefficients of the transilluminated medium and the dimensions of the system. The relation between the measurements of the assumed Mie scattering and the simulation has been plotted as a function of the scattering coefficient for a fixed value of the absorption coefficient of water (Fig. 3.9). The agreement is very good for small values of  $\Sigma_s$ , but for  $\Sigma_s > 4.5$  [ $\text{mm}^{-1}$ ], the width  $L$  is no longer linear and tends to be smaller than expected, moreover, the amplitude  $H$  is slightly above the simulated curve. This phenomenon is explained as a masking effect; ie: the spheres “hide” each other at high concentrations (Flock, 1988, Peters et al., 1990) and the scattering event is no longer independent of the preceding one.

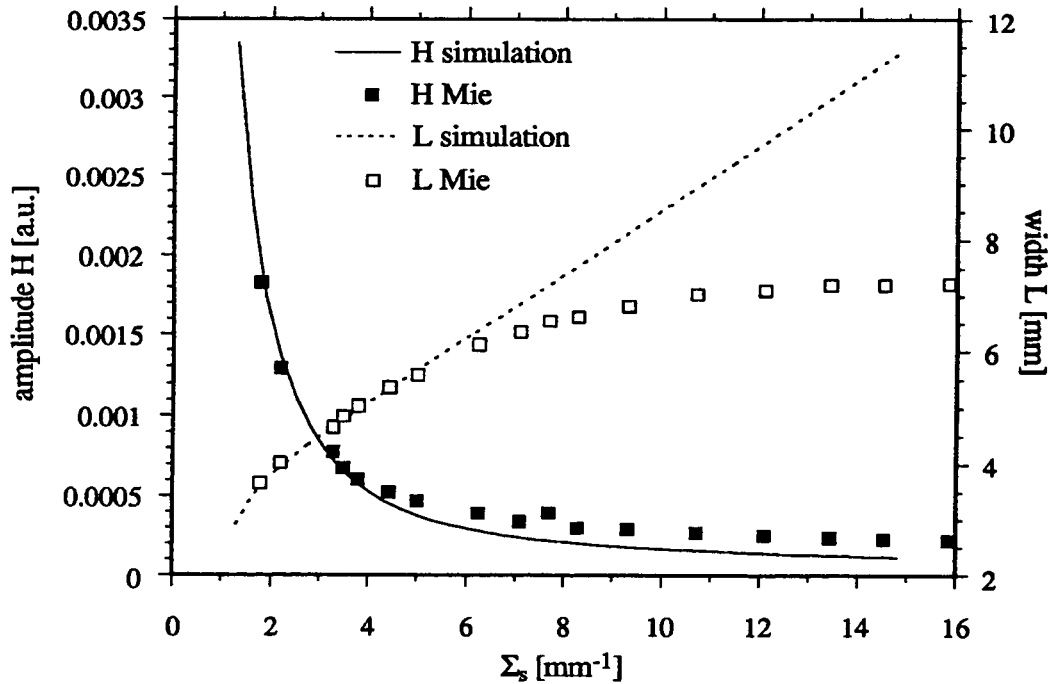


Fig. 3.9: plot of the simulation results and measured values of both the amplitude H (solid line, plain points) and the width L (dotted line, outlined points) for a fixed absorption set at  $5 \times 10^{-4}$  [mm<sup>-1</sup>].

Another comparison has been done with the results published by J.M. Maarek et al. (1984). They used a Monte-Carlo simulation to compute the photon migration through blood and obtained the spatial distribution of photons in a semi-infinite plane-parallel slab. They considered the photons as ambulatory particles and blood as a suspension of red cells in a perfectly transparent plasma. The phase function for the scattering process has been obtained experimentally from  $0^\circ$  to  $180^\circ$ , with  $10^\circ$  intervals, with extremely diluted human whole blood samples (hematocrit ratios of 0.1 and 0.45). They derived a discrete cumulative probability distribution to be used in the Monte-Carlo simulation. This is not exactly the cumulative probability obtained with the H-G phase function, but the spatial repartition of photons is fairly similar to our results: the TOF  $t_f$  is fixed at 200 [ps], the anisotropy factor  $g$  has been set at 0.55, 0.75 and 0.95, the absorbed photon coordinates are stored and a two dimensional projection ( $x$ - $z$  plane) is plotted in each of these figures (Fig. 3.10 to Fig. 3.15). A detailed plot is provided to have a better overview of biological tissue scattering within the first millimetre, where the forward scattering is mostly observable.

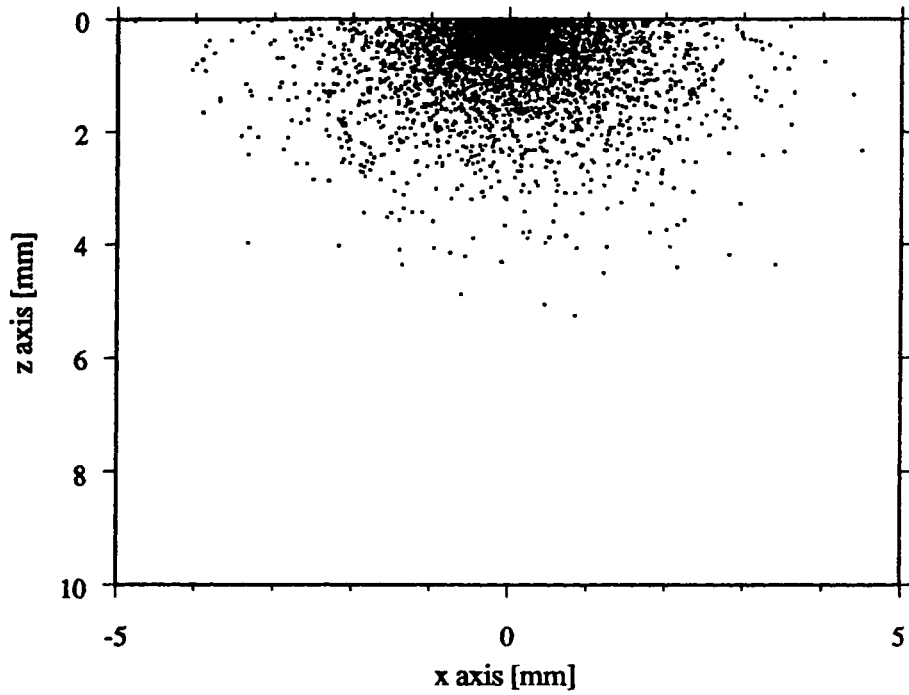


Fig. 3.10: absorbed photon distribution in tissue with  $\Sigma_a=0.07$ ,  $\Sigma_s=17.2$ ,  $g = 0.55$  and a TOF of 200 [ps].

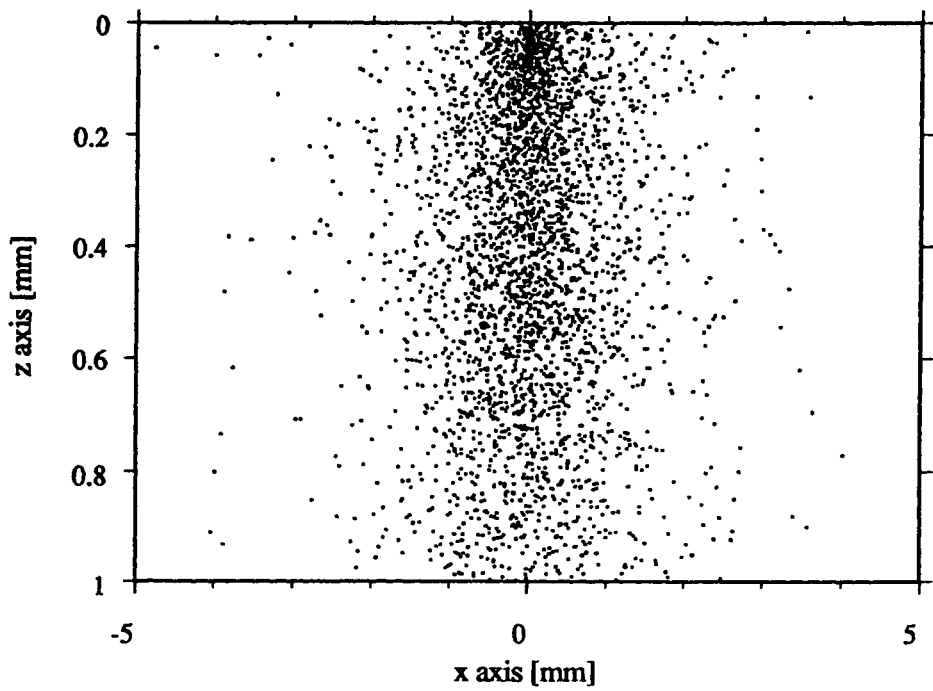


Fig. 3.11: detail of the preceding figure.

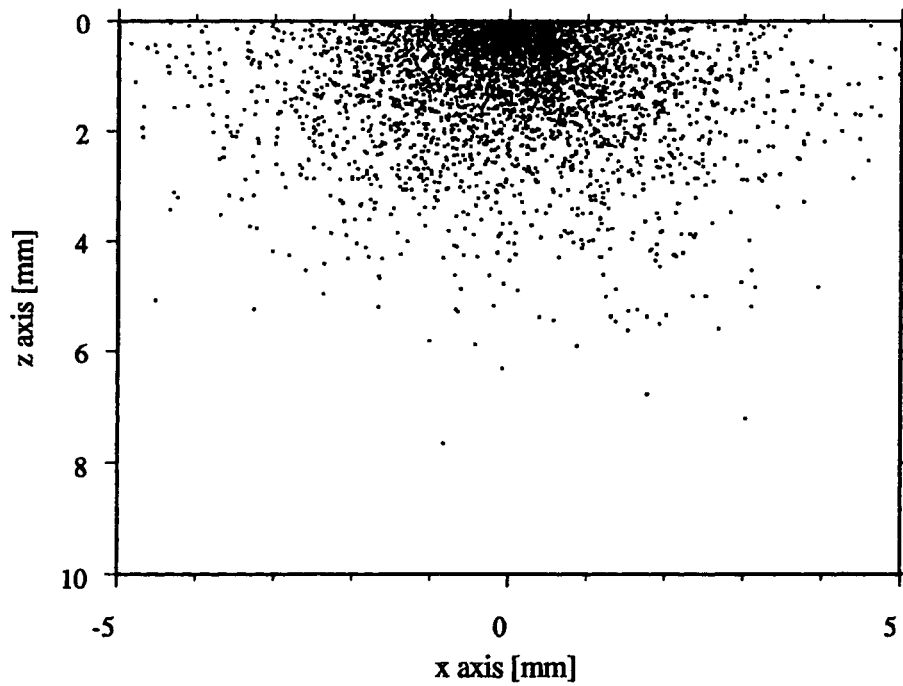


Fig. 3.12: absorbed photon distribution in tissue with  $\Sigma_a=0.07$ ,  $\Sigma_s=17.2$ ,  $g = 0.75$  and a TOF of 200 [ps].

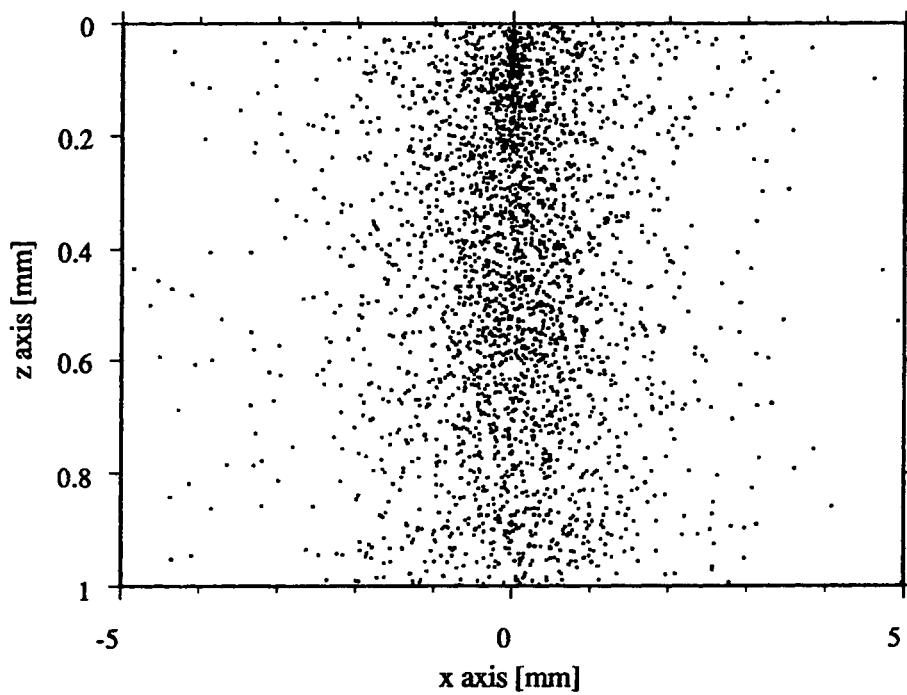


Fig. 3.13: detail of the preceding figure.

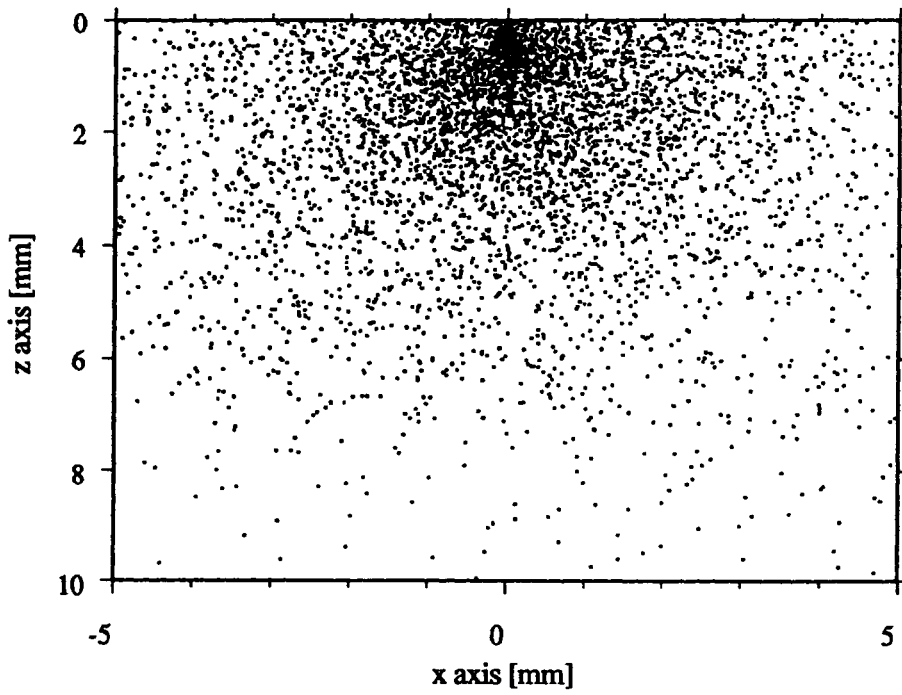


Fig. 3.14: absorbed photon distribution in tissue with  $\Sigma_a=0.07$ ,  $\Sigma_s=17.2$ ,  $g = 0.95$  and a TOF of 200 [ps].

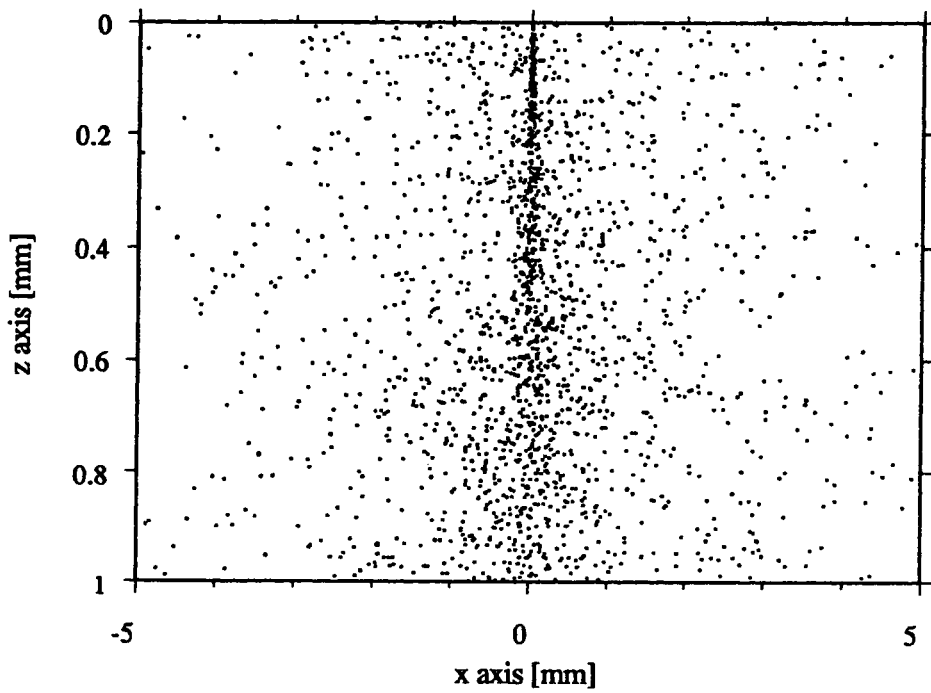


Fig. 3.15: detail of the preceding figure.

Although the phase function they described is empirically established and not the analytical H-G phase function used in the present simulation, the present photon distributions in the tissue are consistent with the published results. The average distribution is a radially symmetrical distribution for the three different anisotropic factors  $g$ . This phenomenon is easily observable on samples of biological tissues or phantoms, where light seems to be evenly scattered in the space, the direction being totally random. This was observed and described by C.C. Johnson (1970) in whole blood, where the emitted light from a fibre optic had a spherical shape. These observations could lead to erroneous consideration or critical over simplifications. Nevertheless, a closer observation of the spatial distribution in the first millimetre of the sample (Fig. 3.11, Fig. 3.13 and Fig. 3.15) shows a significant difference in the photon migration for the three different anisotropic factors  $g$ .

### 3.5.1. Optical density

An important parameter in tissue transillumination is the extinction property of biological tissues. The amount of transmitted photons will determine the quality and the reliability of the image. The optical density should lead to the accurate choice of the source intensity, detector, and the experimental conditions, in order to have optimal images. For example, the quantum efficiency of the eye such that it is able to recognise an image made out of almost  $10^5$  [photons  $\text{cm}^{-2}$ ] (Rose, 1973) and so a minimum number of photons is required.

The computing of the optical density OD and the temporal optical density  $\text{OD}_t$ , defined as  $\text{OD}_t = -\log I_t/I_0$  where  $I_t$  is the transmitted intensity up to time  $t$ , has been done with a single pulse illuminating a tissue slab, and the photons have been collected on the simulated CCD detector. The optical density has been then plotted as a function of the sample thickness (Fig. 3.16) and of the time of flight (Fig. 3.17). The data points and linear regressions have been computed for thicknesses from 0.5 to 5 [mm] each 0.5 [mm] and 10, 20 and 40 [mm]. The temporal optical density  $\text{OD}_t$  has also been plotted as a function of the time of flight TOF for a 5 [mm] thick adipose slab. Both of these plots give a good representation of the photon loss for thick slabs of tissues or short TOF.



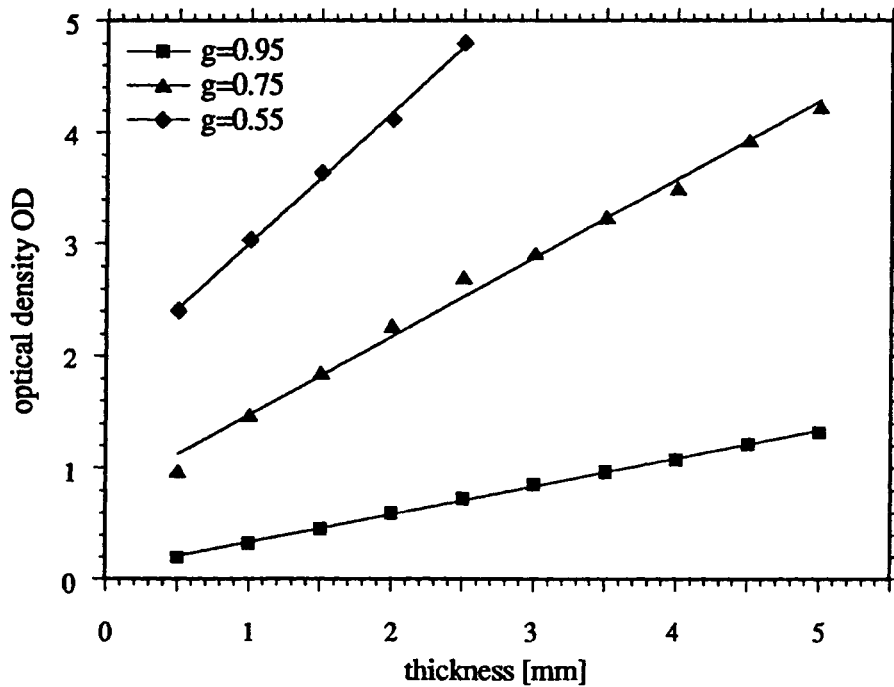


Fig. 3.16: plot of the optical density OD as a function of the sample thickness. The sample is an adipose tissue with  $\Sigma_a=0.07$ ,  $\Sigma_s=17.2$ ,  $g = 0.55, 0.75$  and  $0.95$ , the TOF has been set at two times the ballistic time  $t_b$ .

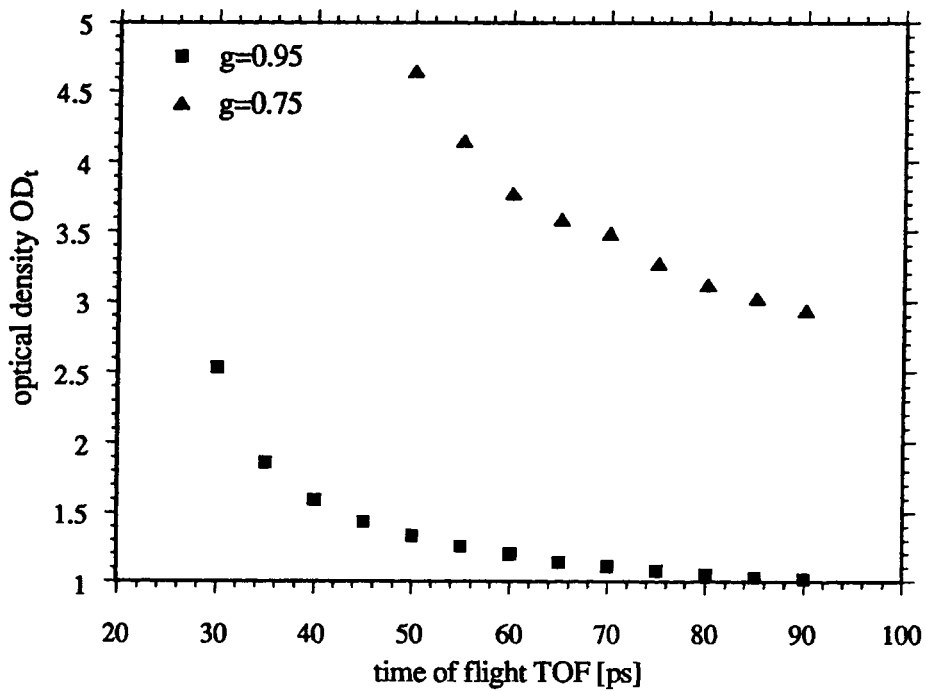


Fig. 3.17: plot of the temporal optical density  $OD_t$  as a function of the time of flight for a 5 [mm] thick tissue slab with  $\Sigma_a=0.07$ ,  $\Sigma_s=17.2$  and  $g=0.95$  and  $0.75$ . The values for  $g=0.55$  were not displayed for practical reasons

### 3.5.2. Point spread function

The point spread function PSF which admits a Gaussian shape (Fig. 3.18) has been simulated with a point source illuminating a homogeneous plane-parallel slab of adipose tissue (Fig. 3.3 A). The transmitted intensity is then stored on the modelled CCD and integrated over the y-axis in order to have the intensity profile of the PSF which is assumed to be the LSF profile (Eq. 3.8).

$$\int \text{PSF}(x, y) dy = \text{LSF}(x) \quad \text{Eq. 3.8}$$

Then the LSF was normalised in order to have

$$\int \text{LSF}(x) dx = 1 \quad \text{Eq. 3.9}$$

so that the computed MTF starts with the value 1 at spatial frequency 0.

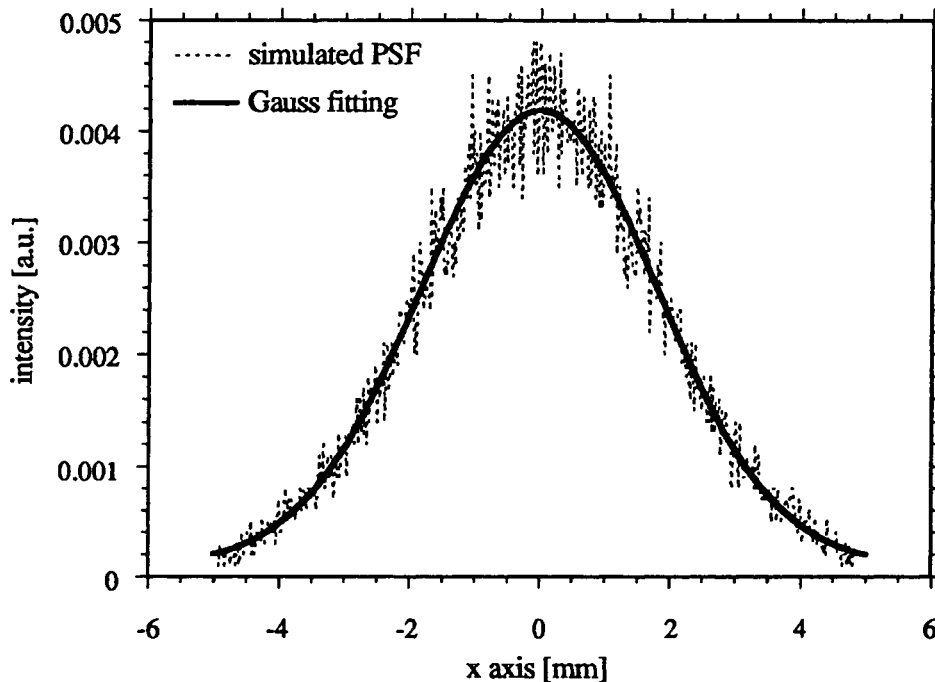


Fig. 3.18: plot of the Gaussian fitting of the PSF (solid line) superposed on the simulated PSF (dotted line).

The PSF is characterised by its width or FWHM which is also a significant parameter for the image resolution (resolution criteria). Roughly, a distinct spot, with an estimated diameter which looks much smaller than the FWHM of the computed PSF, could not be assumed as an object. However the MTF is more practical in determining the image resolution. The cut-off frequency could be read directly as the spatial frequency corresponding to the half amplitude of the MTF (DeVelis and Reynolds, 1979, see also appendix A.8).

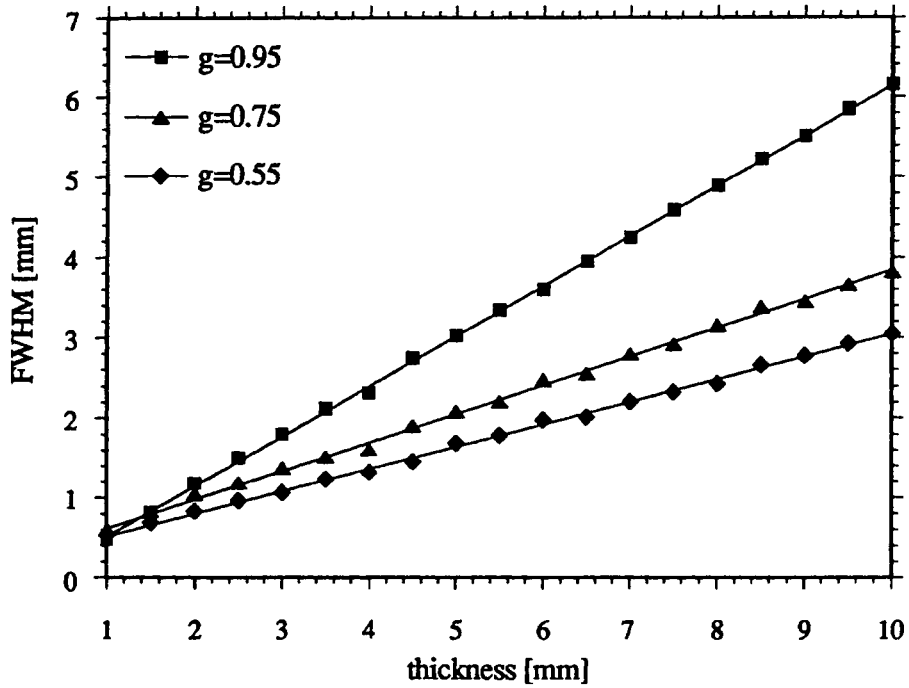


Fig. 3.19: plot of the PSF FWHM as a function of the thickness of a tissue slab, for  $\Sigma_a=0.07$ ,  $\Sigma_s=17.2$  and  $g=0.95$ ,  $0.75$  and  $0.55$ . The TOF has been set at four times the ballistic time  $t_b$ .

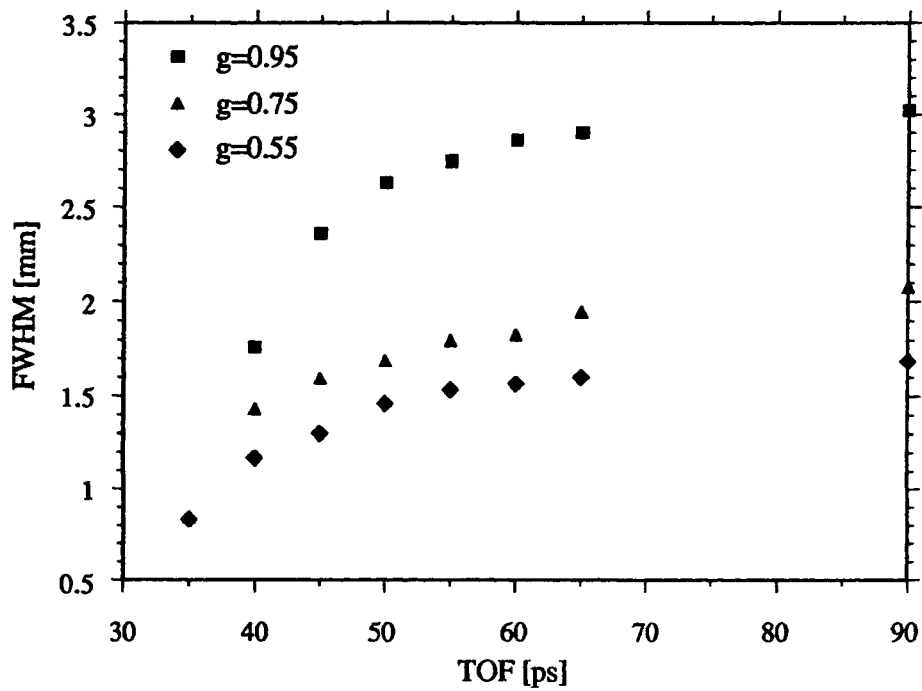


Fig. 3.20: plot of the PSF FWHM as a function of the time of flight for a 5 [mm] thick tissue slab with  $\Sigma_a=0.07$ ,  $\Sigma_s=17.2$  and  $g=0.95$ ,  $0.75$  and  $0.55$ .

The widths of the PSF have been computed for different situations as thickness (Fig. 3.19) and gating time (Fig. 3.20). The result looks unexpected, for the more scattering is the slab, the narrower is the FWHM. This is only due to the phase function and particularly to the anisotropic factor  $g$ . For a  $g$  near to 1, almost all photons are forward scattered, they propagate through the slab and reach the detector within the time of flight. If  $g$  is much smaller than 1, only the few less scattered photons reach the detector within the time of flight and the signal will look narrower. The multiple scattered photons which should contribute to the broadening of the signal are not detected, for they remain in the slab, either absorbed or “frozen” due to the limited TOF. This phenomenon is also observable on Fig. 3.10 to Fig. 3.15 where the photon repartition is more confined for small values of  $g$  (Fig. 3.11) than for greater values of  $g$  (Fig. 3.15). From now, the simulation has been run only for an anisotropic factor  $g=0.95$  and no longer for  $g=0.75$  and  $g=0.55$ . This choice has been determined on the tissue characteristics which typically have a  $g$  near 0.95. Furthermore, only slab thicknesses of 20 and 40 [mm] have been considered to meet clinical conditions (Fig. 3.21).

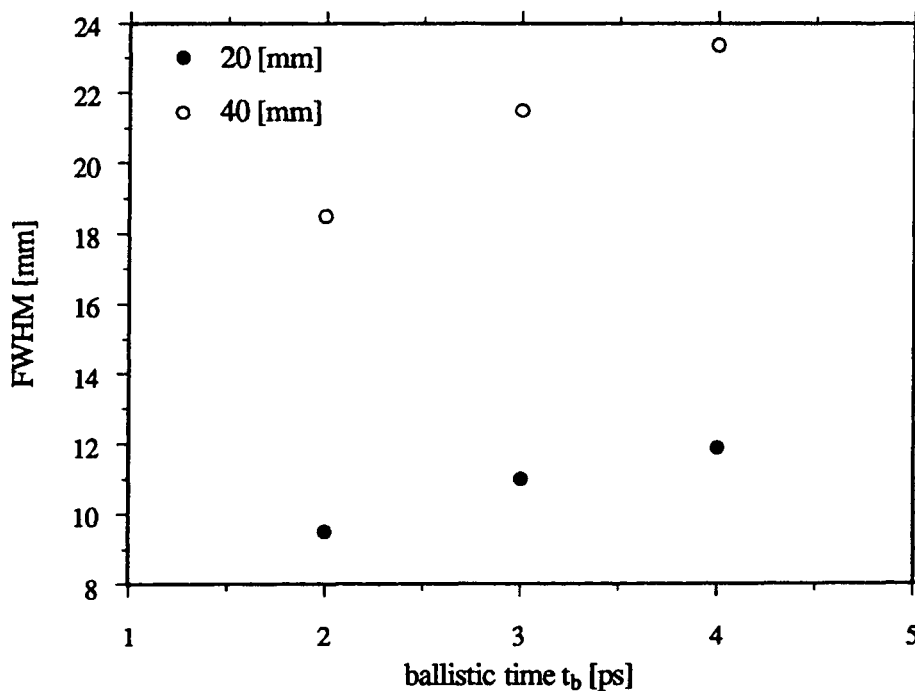


Fig. 3.21: plot of the PSF width for a human breast in clinical conditions, i.e. for 20 and 40 [mm] thick slabs and  $g=0.95$ , as a function of the time of flight expressed in multiples of the ballistic time  $t_b$ .

### 3.5.3. Contrast

The contrasts have been computed at 700 [nm] for two adjacent 10 [mm] thick slabs of different tissues with  $g=0.95$ , illuminated with the expanded source (Fig. 3.22). The mean value of the transmitted intensity for each slab was taken avoiding the edge value. Then with the optical intensity OD the contrast was determined (Eq. 3.3).

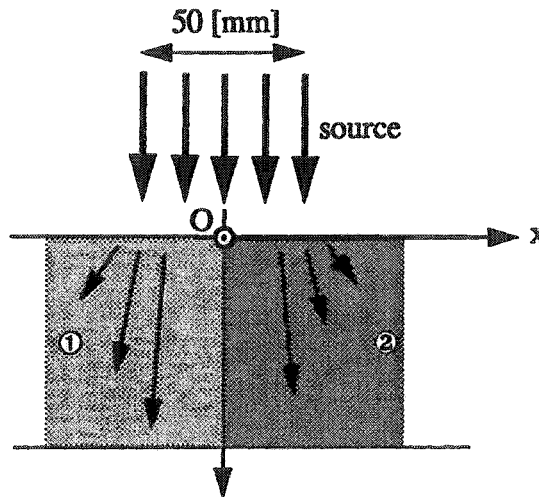


Fig. 3.22: simulation setting for contrast computing

	Glandular	Adipose	Fibrocystic	Fibroadenoma	Carcinoma
Glandular	0.00	0.20	0.06	0.26	0.09
Adipose	0.20	0.00	0.15	0.06	0.10
Fibrocystic	0.06	0.15	0.00	0.21	0.04
Fibroadenoma	0.26	0.06	0.21	0.00	0.17
Carcinoma	0.09	0.10	0.04	0.17	0.00

Table 2: computed contrasts according to the data displayed in Table 1.

These estimated theoretical contrasts are qualitatively similar to those observed on x-rays mammogram. It appears that the best contrast is obtained between the glandular tissue and the fatty tissue or the fibrous tissue and the fatty tissue, which is the case in mammography, where the pattern of fibrose is a clear and distinct web on the more blurred background due to the fatty content, whereas cancerous lesions are hardly detected except for the tiny microcalcifications embedded in the carcinoma (Rothenberg et al., 1986, Lamarque et al., 1992).

### 3.5.4. Pulse transmission

The transmission of light pulses through biological tissues has been computed in different conditions and the result for a Dirac input signal propagating through a slab of adipose has been compared to the analytical solution for the same conditions (Fig. 3.23). The simulation as well as the analytical solution leads to a

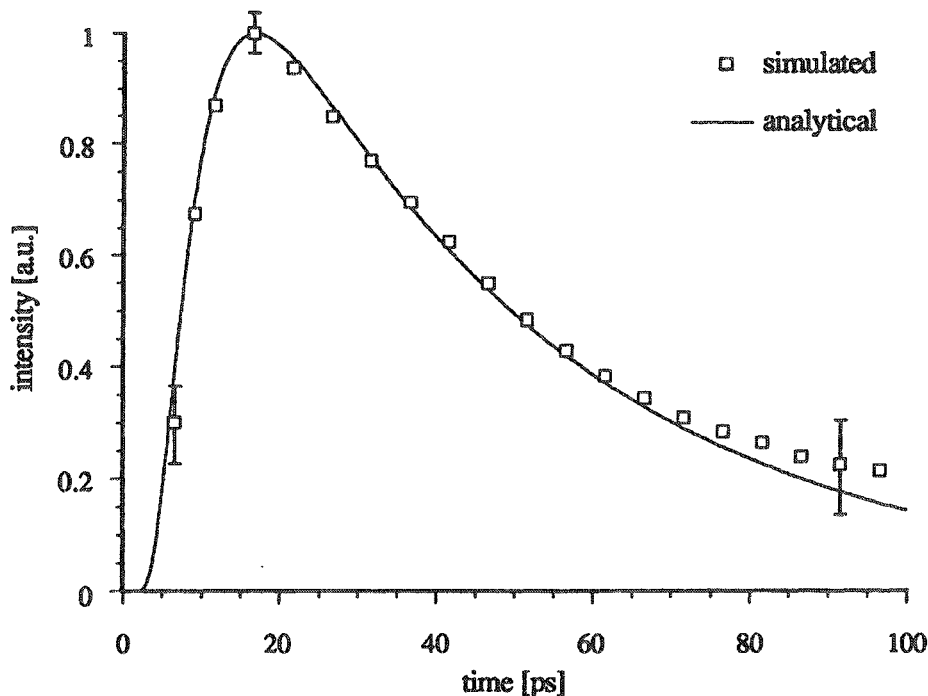


Fig. 3.23: plot of the impulse response computed with the Monte-Carlo simulation (points) and with multiple scattering theory (line) as a function of the time.

so called universal form of the impulse response (Ishimaru, 1978). The output pulses exhibits the same shape, but the width  $T_s$  and delay  $T_d$  differs from one situation to the other, as a function of the scattering conditions. The simulated pulse shows a difference at the end. Actually the signal tail is slightly higher than the analytical prediction. This artifact is due to the detector: the analytical theory assume a 1-D point detector placed in the axis of the incident source and the simulation necessitated a 2-D ( $5 \times 5$  [mm<sup>2</sup>]) surface to detect the photons. This is a more realistic condition, for a streak camera records the signal on a CCD, which is not a 1-D detector.

Furthermore, as mentioned in paragraph 2.5, the behaviour of the pulsewidth  $T_s$  is a function of the square of the slab thickness (Fig. 3.24) which means actually

a strong fluctuation process is dominating or  $\Sigma_a \ll \Sigma_s$ , and the delay  $T_d$  is in the same order of  $T_s$ . To observe weak fluctuations, or linear dependency of  $T_s$  as a function of the slab thickness (Ishimaru, 1978), the pulse broadening should be observed in the very few microns after hitting the surface, so that only a few scattering processes occur. These conditions are no longer in accordance with the diffusion approximation and thus the simulation does not give relevant results.

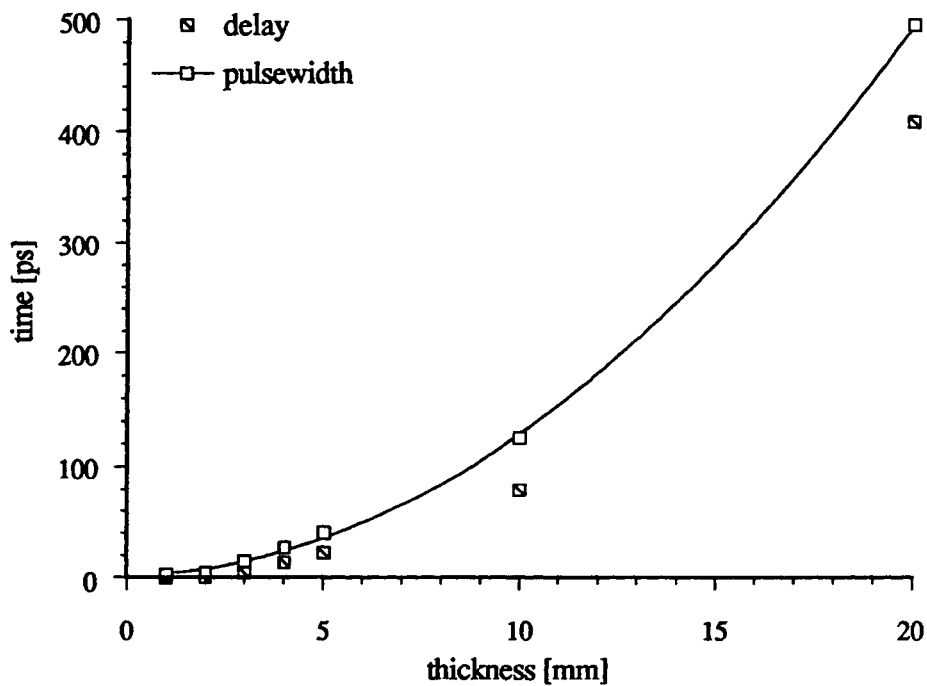


Fig. 3.24: plot of the computed delay  $T_d$  and the pulsewidth  $T_s$  as a function of the thickness in an adipose slab.

### 3.5.5. Image Quality Index or IQI

The resolution of an image is assumed as the capability of rendering tiny details. This resolution can be also defined as the size of the smallest detectable object on a radiological image, the image quality index or IQI (Pochon, 1983, Desponds, 1991, Desponds et al., 1991). The original purpose of the IQI is to dispose of an objective and intuitive method for the evaluation of image quality in screen-film mammography. This index has been shown to be positively correlated with the subjective opinion of radiologists (Desponds et al., 1991). Initially proposed by Harris et al. (1964), the model describing the detectability of a small object is based on decision theory. The probability of a correct detection is related to the signal-to-noise ratio SNR (Rose, 1948). The

calculation of this diameter can be performed from the object contrast, the MTF of the imaging system and the Wiener noise spectrum of the image. Its validity for the prediction of the observation of microcalcifications by radiologists has been assessed by Loo et al. (1984) and more recently by Desponds et al. (1991). Based upon this study, we are confident that the calculation of the diameter of the smallest detectable lesion is correct. The IQI has been defined for the quantitative measurement of image quality in mammography. The value of the IQI is implicitly derived from the general expression of the SNR (Eq. 3.10) for an object which spatial frequency shape is  $S(\hat{f})$ .

$$\text{SNR} = C\sqrt{2\pi} \frac{\int (d\hat{f} \cdot \hat{f} \cdot S^2(\hat{f}) \cdot \text{MTF}^2(\hat{f}))}{\sqrt{\int (d\hat{f} \cdot \hat{f} \cdot S^2(\hat{f}) \cdot \text{MTF}^2(\hat{f}) \cdot W(\hat{f}))}} \quad \text{Eq. 3.10}$$

The expression of the SNR (Eq. 3.10) is valid for a quasi ideal observer (Desponds et al., 1991) and assumes the noise is a white noise and a gaussian object. It can be applied to the image obtained by time resolved transillumination and is in good agreement with the experiment. The shape form factor  $S(\hat{f})$  has been computed for the sphere and is related to the spherical Bessel function  $j_1$  (Eq. 3.11, Gradshteyn and Ryzhik, 1965, Arfken, 1970).

$$S(f) = 4\pi R^3 \frac{j_1(2\pi fR)}{2\pi fR} \quad \text{Eq. 3.11}$$

In our case, the spectrum of a Gaussian object matched to a sphere size is given by Eq. 3.12 (Desponds et al., 1991) and the diameter of the sphere has been derived from the solution of where it is implicitly contained, thus giving a precise estimation of the IQI (which is equal to  $2R$ ).

$$S(f) = \frac{4}{3}\pi R^3 e^{-\frac{2}{3}\pi^2 R^2 f^2} \quad \text{Eq. 3.12}$$

The basic image parameters: the contrast  $C$ , the  $\text{MTF}(f)$  and the Wiener noise spectrum  $W(f)$  have been computed with the simulation. The common values of the SNR are 5 (Rose, 1948) or 5.4 (Desponds et al., 1991) and we decided to use the conservative value of 5.

The unusual expression of the contrast has been motivated by the fact that one needs an expression for  $C$  which is independent of the object size or the slab



thickness. Actually, the determination of the IQI value is an iterative process to fit the size of the embedded object (ie: the value of  $R$  in Eq. 3.12), in order to satisfy Eq. 3.10, so the expression of the contrast must be constant even though the size of the object change.

### **3.5.6. Estimated IQI**

The IQI has been computed for time resolved transillumination on the basis of the simulated image parameters, i.e. the transfer function of the system (MTF of the source, sample, detector combination), the simulated Wiener noise and the contrast  $C=0.1$  from Table 2. The IQI is plotted as a function of the gating time, for different scattering properties ( $g=0.85$  and  $g=0.95$ , Fig. 3.25) and tissue slab thickness ( $z=20$  [mm] and  $40$  [mm], Fig. 3.26). The noise is considered as a Gaussian white noise for gating times greater than  $40$  [ps]. A minimum of the IQI values is observed around  $40$  [ps] ( $100$  [ps]) for the  $20$  [mm] ( $40$  [mm]) thick slab. This minimal value mainly originates from the competitive action of the decrease of the PSF width and noise increase at short gating time. Actually, the PSF are very narrow at short gating times (Fig. 3.20), but the noise contribution increases rapidly. This leads to an optimal situation for the image quality which depends on the tissue thickness and the intensity of the source. Obviously, the curves would shift left- and downwards for more intense sources or longer exposure time. We arbitrarily chose only one pulse striking the upper surface of the slab. It is interesting to observe that the anisotropic factor  $g$  plays an important role in the IQI calculation. As mentioned before, for  $g$  near to  $1$ , the PSF are wider than those for  $g$  smaller than  $1$ , whereas the IQI values are greater for  $g=0.85$  than for  $g=0.95$ . There is obviously a balance between the broader PSF for great values of  $g$  and the noise increase for small values of  $g$  due to a greater optical density OD (there are less transmitted photons and the quantum noise increases), so that the noise is actually the most limiting factor to the IQI in the case of tissue transillumination.

These promising results have to be compared with the modern conventional diaphanography. Systematic screening on a large group of subjects has reported that lesions smaller than  $5$  [mm] can not be detected (Drexler et al., 1985).

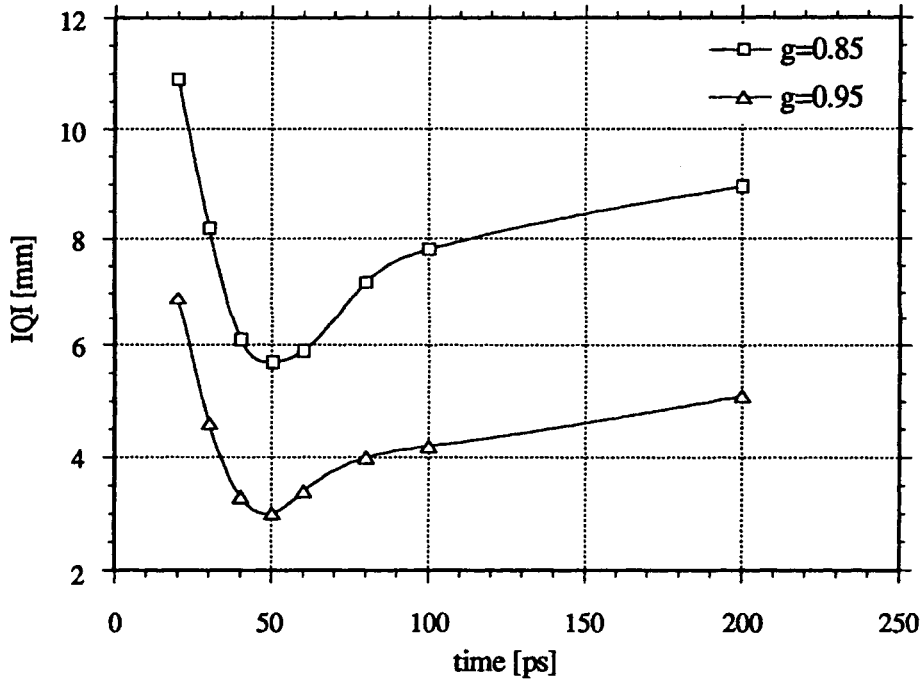


Fig. 3.25: plot of the IQI as a function of the gating time for  $g=0.85$  and  $g=0.95$  through a 20 [mm] slab of adipose and a contrast of 0.1.

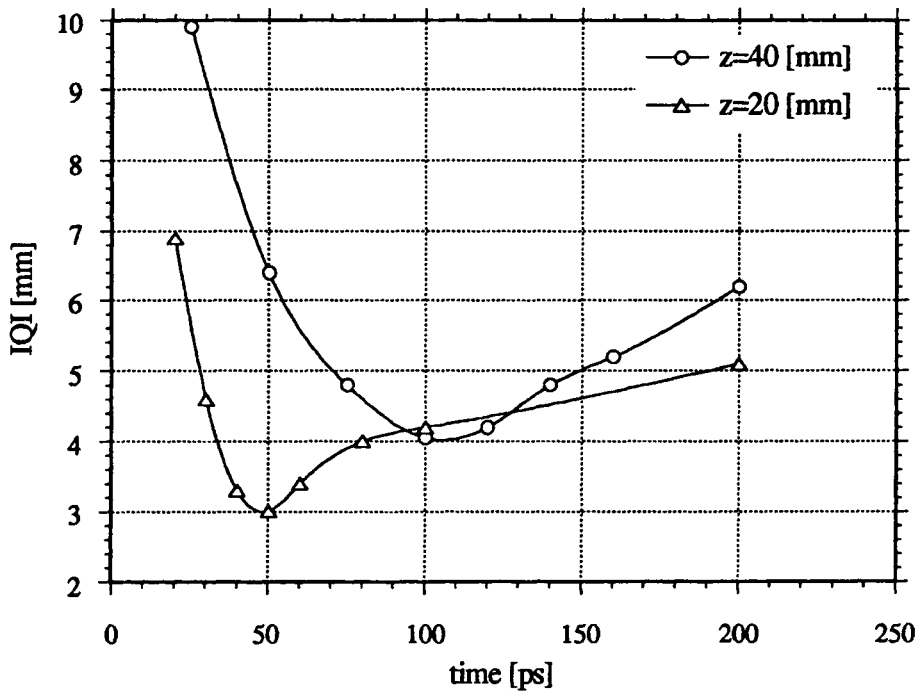


Fig. 3.26: plot of the IQI as a function of the gating time through a slab thickness of 20 and 40 [mm] of adipose for  $g=0.95$  and a contrast of 0.1.

Cancers which are typically larger than 10 [mm] are detected in a few percentage of patients, and for a reliable diagnostic, the lesion must be equal or greater than 20 [mm] (Bartrum and Crow, 1984, Geslien et al., 1985). This study however does not provide details on the exact location of the detected lesions. There are no available information about the thickness of the examined breasts and how deep the lesions were located. Thus the predicted values give only a rough estimation of the diagnostic performance of diaphanography which is 30% for 10 [mm] lesions, 64% for lesions from 10 to 20 [mm] and 78% for lesions greater than 20 [mm] (Bartrum and Crow, 1984).

### 3.5.7. Simulated images

A spherical object is located in the sample and gives various intensity profiles depending on its depth and its size. It is obvious that the depth or size of the lesion is very important in the transillumination and the image would be greatly blurred for objects far from the detector or tiny lesions, due to multiple scattering. A simple model has been simulated, a sphere approximating the carcinoma is set in the slab assumed to be homogeneous. The optical characteristics of the sphere are taken from Table 1 (carcinoma) and the surrounding medium is assumed as adipose. In a first step, images were simulated with a single pulse of  $10^9$  photons, but the computing time being too long, the method using convolution has been preferred for further simulations. Images of objects have been computed combining the MTF and the spatial spectrum  $S$  of an object then superposing the noise (Eq. 3.13).

$$\text{image} = \mathcal{F}^{-1}(\text{MTF} \cdot S) + \text{noise} \quad \text{Eq. 3.13}$$

With this convolution method, the computation of an image is no longer time consuming, and enables the imaging of more complicated shapes than simple spheres. With Eq. 3.13, non-time-resolved images of an absorbing and a non absorbing 2 [mm] spherical object embedded in the middle of a 10 [mm] thick slab of adipose have been simulated in order to have a comparative result of both cases (Fig. 3.27). Obviously, the absorbing sphere leaves a darker shadow on the image and the scattering sphere a brighter area than the surrounding medium.

Further, the image of an absorbing 4 [mm] sphere in the centre of a 20 [mm] thick adipose slab has been computed for different gating times, i.e. 50, 100 and 200 [ps] (Fig. 3.28). The effect of the gating time is significant, the contrast and shape of the object being more distinct for short gating times, but the noise pattern increases too.

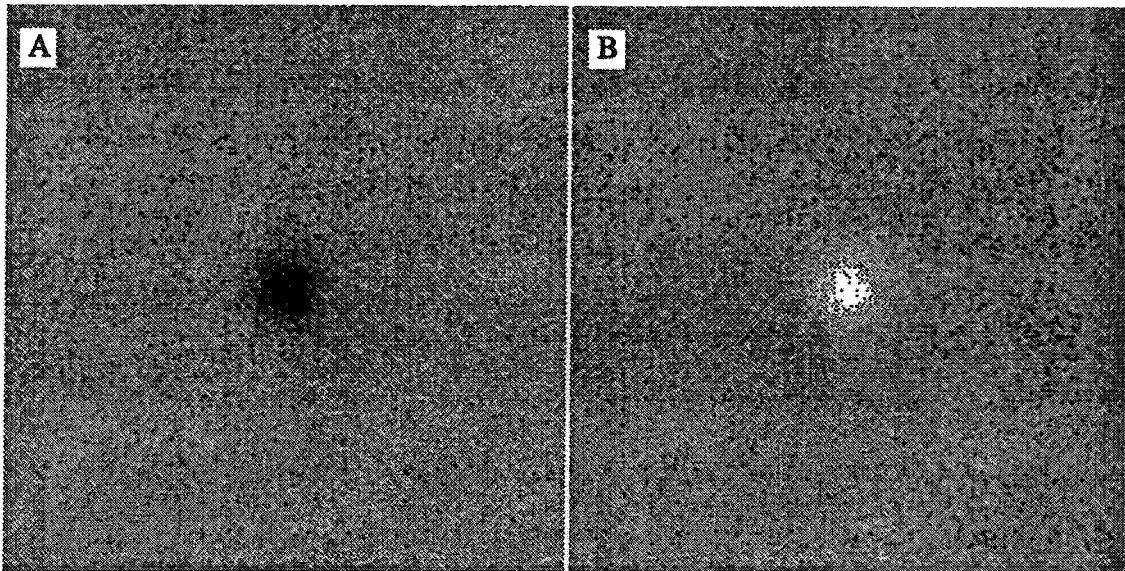


Fig. 3.27: simulated  $10 \times 10$  [mm<sup>2</sup>] images of a 2 [mm] spherical object in the middle of a 10 [mm] thick sample. Image A is the image of an opaque object and in image B the object is scattering.

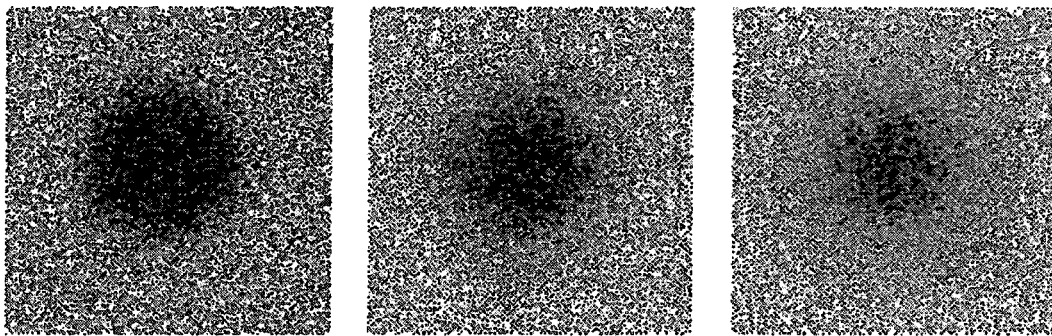


Fig. 3.28: simulated  $10 \times 10$  [mm<sup>2</sup>] images of a 4 [mm] absorbing sphere within a 20 [mm] thick slab of adipose for a gating time of 50, 100 and 200 [ps].

Furthermore, the simulation has been then compared to the analytical solution of the perturbation of the transmitted light by a spherical object presented in paragraph 2.4. The intensity profile of the simulated image (non time resolved) is superposed on the analytical solution for a 2 [mm] sphere with carcinoma-like

optical properties set in the middle of a 10 [mm] thick slab of adipose (Fig. 3.29). The analytical solution looks narrower. Actually, the profile of the simulation result has been fitted to a Gaussian curve to get rid of the noise whereas the analytical solution is a smooth function. The displayed numerical result is the best fit on the computed result (analog to Fig. 3.18) and the analytical curve is covered by the noise contribution so that the small difference should not be significant. Nevertheless, the difference originates probably from the different phase functions used either in the analytical solution or the Monte-Carlo simulation.

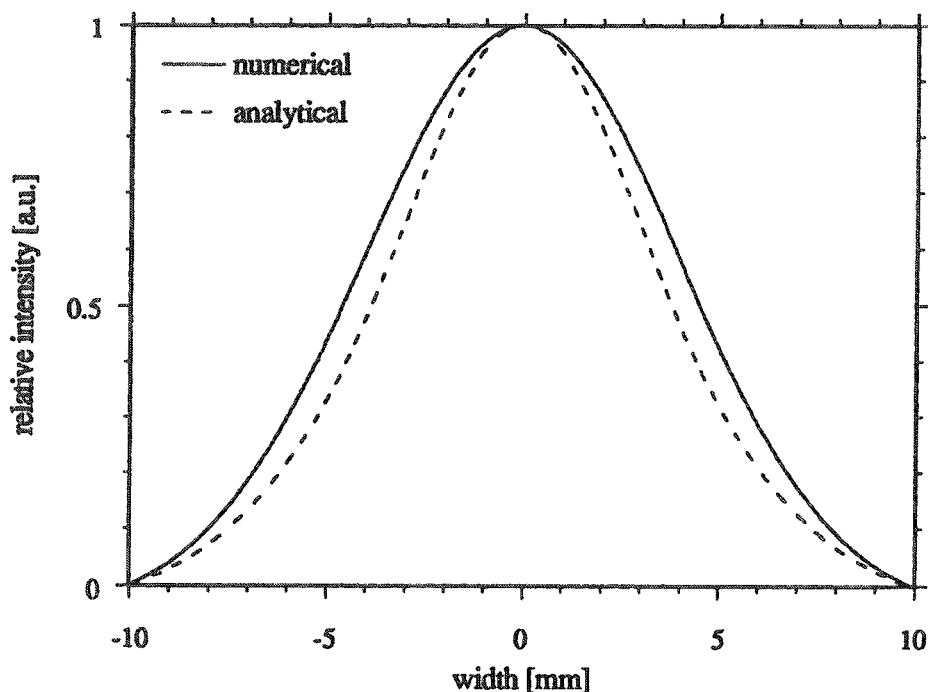
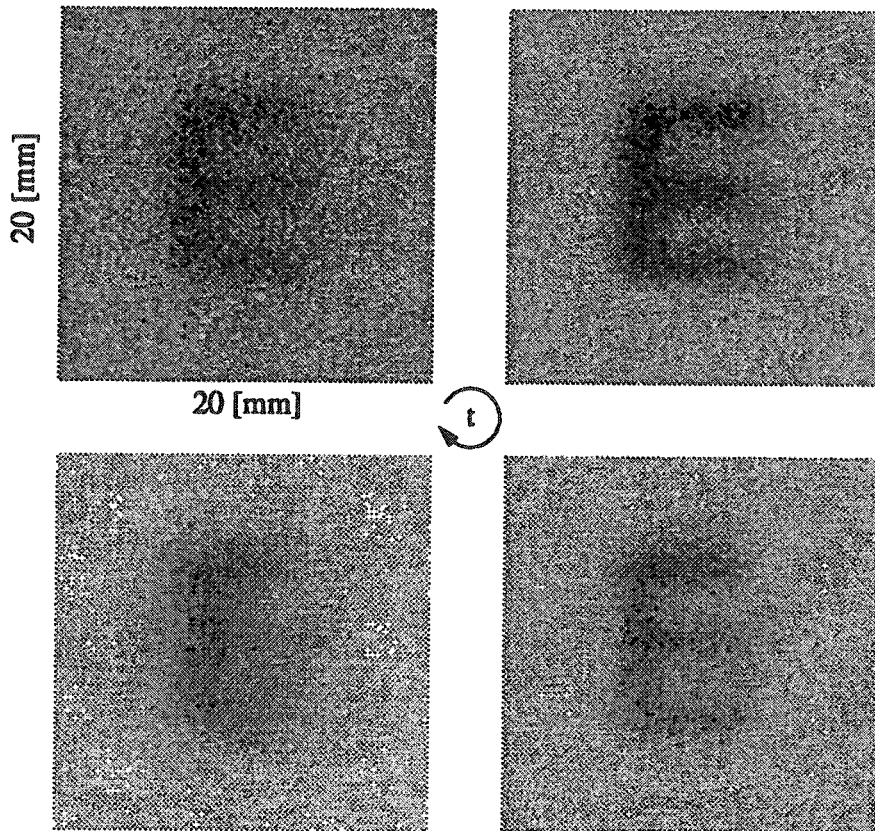


Fig. 3.29: comparison of the normalised intensity profiles of a Monte-Carlo simulated (solid line) and an analytical computed (dashed line) lineshape of a 2 [mm] sphere at 5 [mm] within a 10 [mm] thick slab.

To have an illustration of the contribution of both noise for short gating time and multiple scattering for long gating time, the image of an opaque E has been simulated for different gating times. The 20 [mm] thick medium uses the optical coefficients of adipose, a  $g$  of 0.95 and the letter, which is totally absorbing, is set in the middle of a  $20 \times 20$  [mm<sup>2</sup>] square and the width of the lines are 2 [mm]. The optimal result has been computed with a gating time of 50 [ps] whereas for 20 [ps] the noise diminishes the visibility of the letter and for 200 [ps] the

multiple scattered photons strongly blur the image and the letter is hardly recognised.



**Fig. 3.30:** transmission simulation of an object (E) through 20 [mm] of adipose for gating times  $t$  of 20, 50, 100 and 200 [ps] (clockwise from top at left).

## CHAPTER 4

# ***EXPERIMENT***

The experimental method for the study of light transport through biological tissues has been divided into two parts. On the first hand, the characterisation of various breast tissues have been determined in order to have a differentiation between healthy and cancerous breast tissues, with the widely used method using integrating sphere measurements analysed with the K-M theory, then compared to another method using a CCD line to measure the PSF of a tissue region. On the other hand, the time resolved imaging has been tested. The transmission of a light pulse has been measured for various tissues and detector gating.

### **4.1. Tissue characterisation**

Tissue characterisation is one of the XX<sup>th</sup> century medical challenges. Many methods based on ultrasonic devices, thermographic units, MRI techniques, NMR spectroscopy as well as light measurements have been investigated to determine which method would be the most practical for noninvasive in-vivo tissue characterisation and accurate diagnosis (Cold, 1986). These different methods have both pros and cons, which are mainly related to the physical technique used: for example, the ultrasonic method is able to give reliable

information, but different tissues with the same acoustic impedance will give the same value; thermography is able to give the temperature pattern of a living tissue but lacks specificity (Jones, 1982); the IRM or NMR spectroscopy necessitates enormous technology and appears to be expensive in predictive medicine and screening campaign (Jones, 1982); finally optical tissue characterisation by mean of NIR or far red illumination is one of the most simple methods with the use of tiny laser diodes and fiber optics but did not give relevant results with in-vivo experimentation. Nevertheless, this method has been shown to be accurate for differentiation by in-vitro measures (Flock, 1988, van Gemert, et al., 1988, Peters et al., 1990).

#### 4.1.1. Experimental setting

The widely used method for measuring the optical properties of tissues is based on the K-M theory (Kottler, 1960, Prahl et al., 1987, van Gemert et al., 1987, Peters et al., 1990, see also appendix A.3) for a slab illuminated with a diffuse source. For the transmittance measure (Fig. 4.1a), the collimated laser beam is,

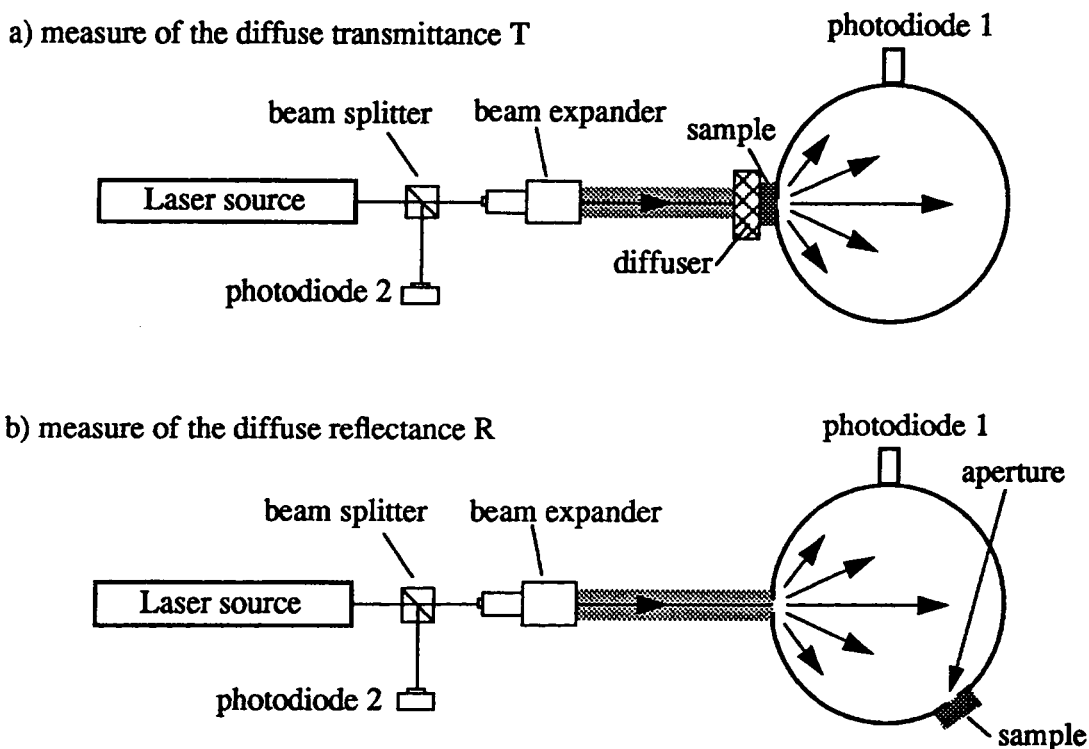


Fig. 4.1: experimental setting for the measure of the diffuse transmittance  $T$  and the diffuse reflectance  $R$ .



expanded with a beam expander and then passes through a diffuser so that the tissue sample behind the diffuser is assumed as illuminated diffusively. The light is then collected in an integrating sphere and the signal measured by the photodiode 1 via a lock-in amplifier and a computer. The signal is normalised in intensity with the photodiode 2 to eliminate the intensity variations of the source. The transmittance  $T$  is given by:

$$T = \frac{T_{\text{sample}}}{T_{\text{inc}}} \quad (\text{Eq. 4.1})$$

where  $T_{\text{sample}}$  is the transmitted light intensity through the sample put in a cuvette measured by the photodiode 1 and  $T_{\text{inc}}$  is the transmitted incident intensity through water in the cuvette measured by the photodiode 1. The cuvette is a 5 [mm] thick glass cuvette (Hellma, series 100-OS).

For the reflectance measure (Fig. 4.1b), the sphere itself is used as the sample illuminator (the sphere is assumed as a perfect light diffuser), so that the diffuse incident illumination condition requested to meet the K-M theory is available. The reflectance  $R$  is then:

$$R = \frac{R_{\text{sample}} - R_{\text{inc}}}{R_{\text{tot}} - R_{\text{inc}}} \quad (\text{Eq. 4.2})$$

where  $R_{\text{sample}}$  is the measured backscattered intensity measured by photodiode 1 with the sample in the cuvette on the aperture and a black background (total absorption),  $R_{\text{inc}}$  the intensity measured by the photodiode 1 with the cuvette filled with water on the aperture and a black background and  $R_{\text{tot}}$  is the measured intensity in the fully tapered sphere (the whole inner surface of the sphere is reflective).  $R_{\text{inc}}$  is adjusted to have an estimated correction for the refracting index mismatch and the reflected light on the illuminated surface of the cuvette. The numerator is then the expression for the total backscattered intensity from the sample only (the effect of the cuvette is taken into) and the denominator is the expression of the total diffuse intensity incident on the sample. The aperture is a circular 5 [mm] hole.

#### **4.1.2. Histology and pathology**

The type of tissues which are encountered in breast are mainly the skin on the

surface, fatty tissues or adipose, fibrose tissue, glandular tissue and the pectoral musculature (Fig. 4.2). The skin colour depend on the individual, the fatty tissues

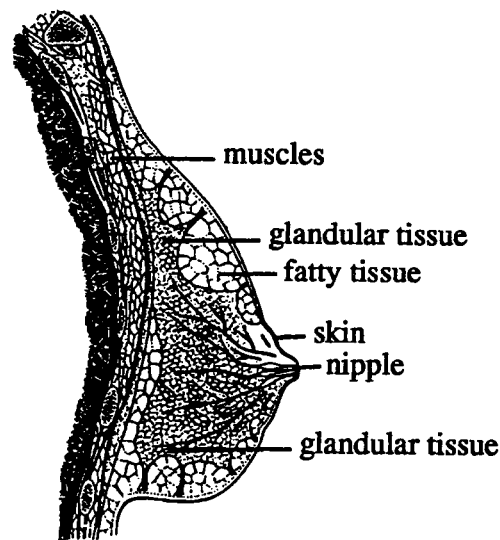


Fig. 4.2: sagittal section of a human breast.

look yellowish, the fibrose and the glandular tissues are off-white or ivory-white and the muscles are red (Genton, 1992). The tissues are more or less perfused as a function of the temperature, the humoral excitation and the kind of tissues (Jain and Ward-Hartley, 1984). They however exhibit a given colour (Genton, 1992) and do not look evenly red due to perfusion. The capillary bed does not alter the colour. The fixation of tissues by formaldehyde at 4% vol. does not change greatly the original colour of a tissue (see also appendix A.10). It tends to tarnish the muscles colour. Thus an in-vitro characterisation of tissues should be fairly near to in-vivo conditions, for the formaldehyde absorption spectrum is near to 1 in the far red NIR region (see also appendix A.8).

#### 4.1.3. Tissue characteristics

The measurements for tissue characterisation were done on 2.5 [mm] thick slabs of surgical resection or autopsy containing different type of tissues as fat, fibrose, glands, cancerous lesions or muscles. The measurements were made on five areas of each sample in order to obtain a rough anatomical mapping of the sample (Fig. 4.3). The histological study made afterwards was able to assess the kind of tissue analysed (Genton, 1992). The distribution of the measured

coefficients is shown in Fig. 4.4 and the mean values and standard deviation related to these measures are displayed in Table 3. Similarly to the results published by Peters et al. (1990), the cancerous tissues appear to be less absorbent than fatty tissues and glandular or fibrous tissues, whereas the absolute values differ of a factor 2 from those published.

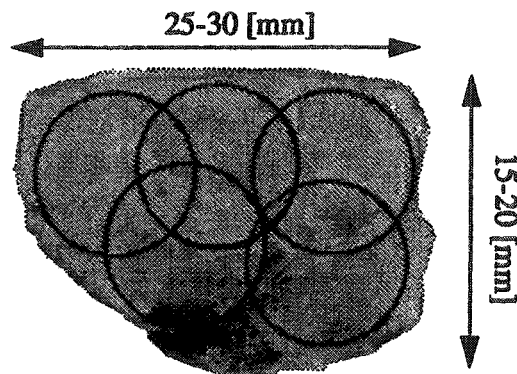


Fig. 4.3: picture of a sample. The 10 [mm] circles cover the measured areas.

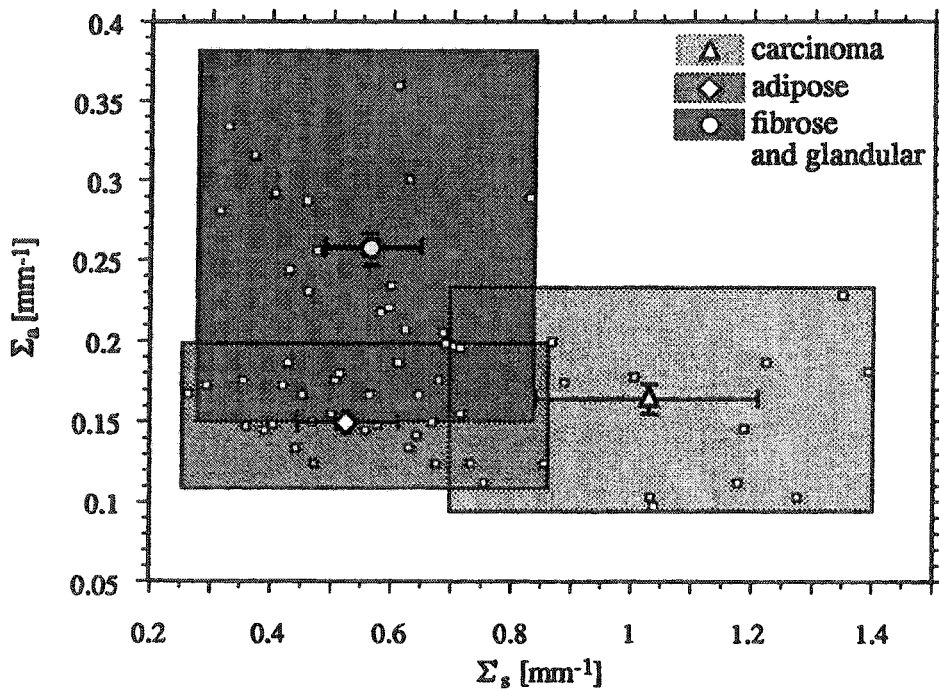


Fig. 4.4: distribution of the measured optical coefficients  $\Sigma_a$  and  $\Sigma'_s$  of tissues (small squares) at 632.8 [nm]. Up and left is the region of fibrose, bottom left the region of adipose and bottom right the region of carcinoma.

It is important to emphasise that these measurements were done on heterogeneous samples so that it was not possible to measure the exact

coefficients of a given tissue. In fact it is more adequate to speak about an average coefficient for a heterogeneous part of tissue with a high content in fat, fibrose or lesion.

		mean [ $\text{mm}^{-1}$ ]	std deviation [ $\text{mm}^{-1}$ ]
fatty tissues	$\Sigma_s'$	0.527	0.139
	$\Sigma_a$	0.157	0.0004
fibrous tissues	$\Sigma_s'$	0.542	0.153
	$\Sigma_a$	0.252	0.003
cancerous lesions	$\Sigma_s'$	1.04	0.242
	$\Sigma_a$	0.167	0.018

Table 3: mean values and standard deviation of the measured optical tissue coefficients for fatty tissues, fibrous tissues and cancerous lesions.

## 4.2. Time resolved imaging

The experimental setting for time resolved transillumination is not a simple task. The latest technology is able to supply ultra-fast sources as picosecond or even femtosecond pulsed lasers (the most common is now the self mode-locked Ti:AlO<sub>3</sub> laser), low-level IR cameras which are able to make an image out of residual light, or high speed streak cameras which give one dimensional images of fast events. There is a lack in ultra-fast gating. The fastest responding amplitude modulators are working at around 1 [GHz] (travelling wave amplitude modulators), giving a rise time of around 500 [ps]. The experimental setting we decided to use consists of a pulsed dye laser, an EO travelling wave modulator and a low-level IR camera as the detection device.

### 4.2.1. Source

The infrared source is a styryl-9M dye laser (Coherent CR-599) the cavity of which was enlarged to 1.979 [m] for pulsed operation. The dye laser is pumped by a mode-locked ion laser (Coherent innova 200 Argon, Mode Locker 468 AS) at 514 [nm] with 75.7676 [MHz] repetition rate. The styryl-9M has a fluorescence maximum at 840 [nm] and the pulses obtained were measured with an autocorrelator (Inrad, model 5-14). The pulse FWHM is around 5 [ps] (Fig.

4.5) and the average output power is around 50 [mW].

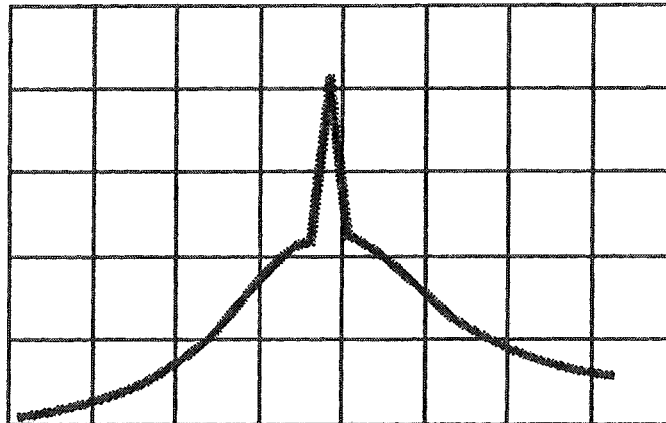


Fig. 4.5: picture of the signal from the autocorrelator.  
The basis of the square is 10 [ps]

#### 4.2.2. Electro-optic amplitude modulator

The electro-optic modulator is a travelling wave amplitude modulator (Quantum Technology, customised TWAM 11-1) tuned at 2 [GHz], thus giving a rise time of 250 [ps] (see also appendix A.11). This type of modulator is designed to modulate the amplitude, hence the intensity of a laser beam. The quiescent point, or state where no voltage is applied, has to be changed in order to get a linear modulation of the signal. This is made possible by the introduction of a quarter-wave plate between the modulator and the analyser, on the optical axis (Fig. 4.6). The quiescent point has to be half-way between the minimum and maximum applied voltage.

The modulator is composed of two 45°Z crystals of LiTaO<sub>3</sub> so that the optic axes are perpendicular to the direction of electrical conduction and the rotated Y axis is along the cylindrical axis of the modulator. The crystal faces are AR coated. The total length of the crystal is 25 [mm] and the aperture is 1×1 [mm<sup>2</sup>]. Thus

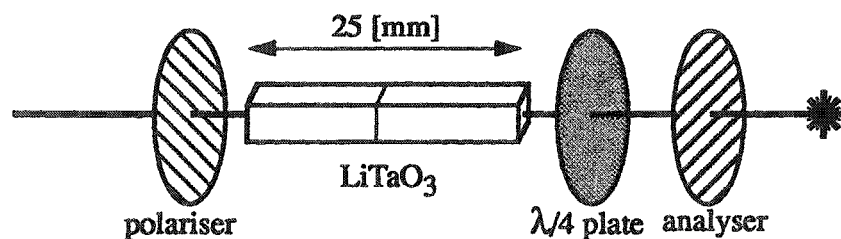


Fig. 4.6: setting of the amplitude modulator between the two polarisers and the quarter-wave plate.

the image transmission through the crystal is diffraction limited due to the small aperture. To mostly reduce the diffraction effects on the image transmission, the beam is focused on the crystal face with an achromat convergent lens (focal length  $f=400$  [mm],  $\phi=100$  [mm]), so that the beam waist centred in the middle of the crystal exhibits a size below the crystal aperture. After the crystal, a same lens is set to collimate the beam on the detector (Fig. 4.7). With this setting, the image of a needle illuminated by a 20 [mm] beam could be observed through the crystal and the resolution has been estimated at 100 [ $\mu\text{m}$ ].

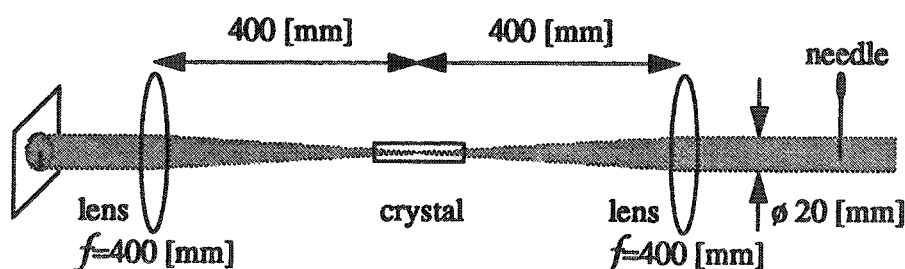


Fig. 4.7: optical setting to focus the beam in the crystal.

A simple simulation shows the 80% modulation at 2 [GHz] of a 200 [ps] wide pulse with the modulator (Fig. 4.8). The modulated pulse admits various shape

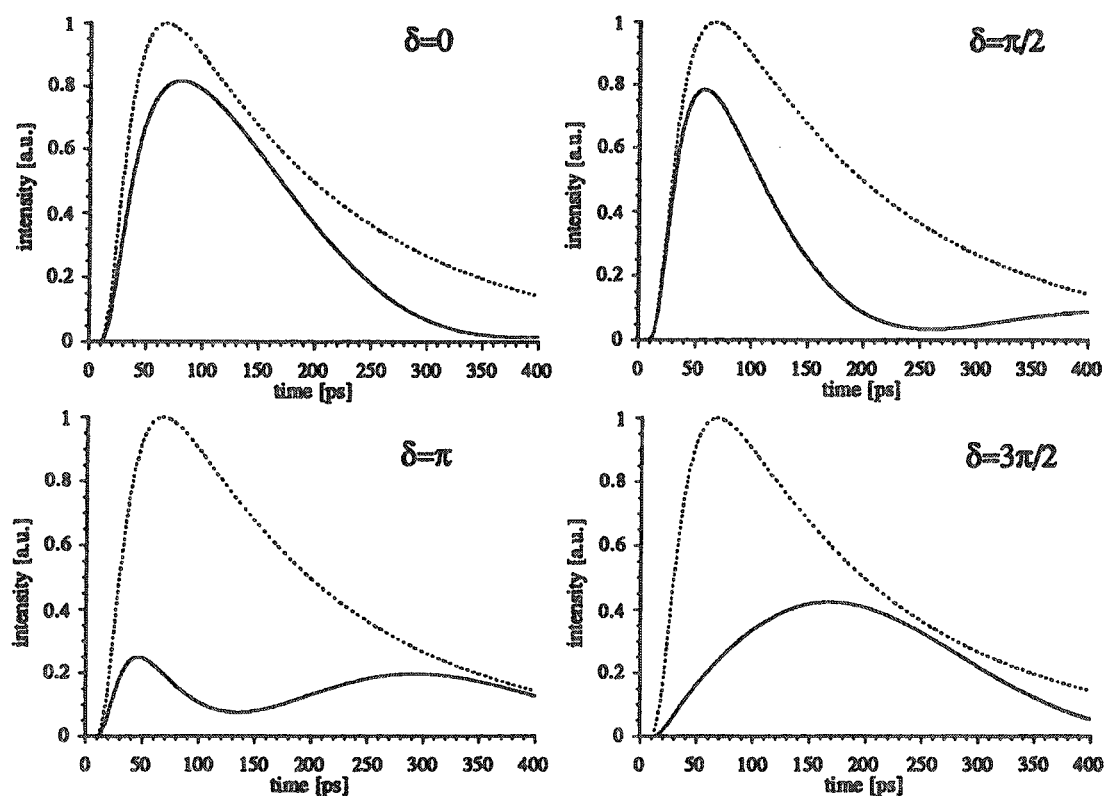


Fig. 4.8: plots of the 200 [ps] wide unmodulated pulse (dotted line) and the modulated pulse (solid line) for different phase shifts  $\delta$  corresponding to 0,  $\pi/2$ ,  $\pi$  and  $3\pi/2$ .

as a function of the phase shift  $\delta$ . An optimum has to be found in order to detect the most of the snake like photons ( $\delta$  around  $\pi/2$ ), but attention has to be paid to the second wave which contains multiple scattered photons ( $\delta$  around  $\pi$ ).

#### 4.2.3. Detector

The detection is supplied by a custom high-sensitive integrating IR camera. It consists in a  $512 \times 512$  pixel array from Tektronix (CCD imager TK512 CB, backside illuminated), plugged in a TK1DEV board also from Tektronix. The image acquisition is made via a standard I/O board driven by an acquisition program developed under LabVIEW<sup>®</sup> 2 (see also appendix A.12).

The CCD chip has a  $13.8 \times 13.8$  [mm<sup>2</sup>] imaging area, each pixel being a  $27 \times 27$  [ $\mu\text{m}^2$ ] surface. The CCD chip is cooled by three successive Peltier elements, the temperature range extends from 233 to 293 [°K] and the whole camera is immersed in dry argon (Ar) atmosphere to avoid condensation and frost build up. Preliminary images (Fig. 4.9) have been done with a vertical opaque grid as object and a 20 [mm] thick cuvette filled with a 5% solution of lipovenös as scattering medium. These images show that a colloidal suspension as scattering medium is not a realistic phantom for imaging, for a sufficiently sensitive camera is able to render the grid pattern even through the lipovenös solution.

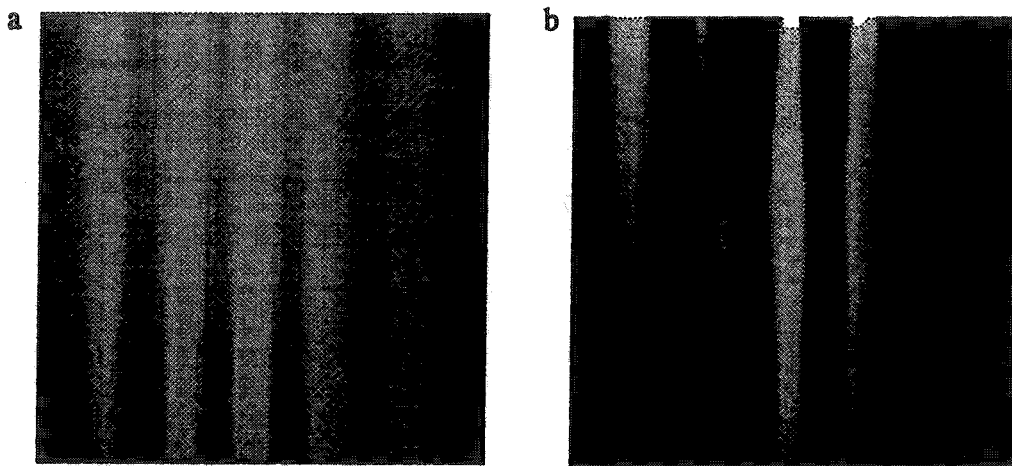


Fig. 4.9:  $20 \times 20$  [mm<sup>2</sup>] images of a vertical opaque grid through a 20 [mm] thick cuvette filled with a 5% solution of lipovenös: a-image of the grid taken with the IR camera; b-image of the grid taken with the IR camera and a spatial filtering (pinhole).

### 4.3. Results

Preliminary measurements were planned in order to confirm the analytical and numerical model. For this purpose, we used of a streak camera to observe and qualify the pulse transmission through turbid media. Similar measurements have been done by K.M. Yoo and R.R. Alfano (1990) (see also Yoo et al., 1990) and G. Zaccanti (1992). These measured output pulses have been compared to analytical and simulation results.

In a second step, the experimental setting for time resolved imaging has been set and tested in order to observe the gating of a pulse and to obtain a time resolved image of an object behind a turbid sample.

#### 4.3.1. Streak camera

We had the opportunity to use a Hamamatsu synchroscan streak camera to perform measures of the output pulses from various turbid media. In the transmission of a light pulse through a thick turbid medium, the scattering and absorption cause both attenuation of the transmitted intensity and distortion of the pulse, the shape of which becomes broadened. From these measurements, it should be possible to extract information on the turbid medium, particularly on the scattering properties of the transilluminated media (Wilson, 1992). These measurements were also of importance in order to settle the validity of the analytical and the simulation results.

The light beam is normally incident on a cuvette containing the investigated sample and the transmitted intensity reaches the streak camera through a diaphragm thus providing colinear detection. A triggering diode is driven by a reference beam (Fig. 4.10).

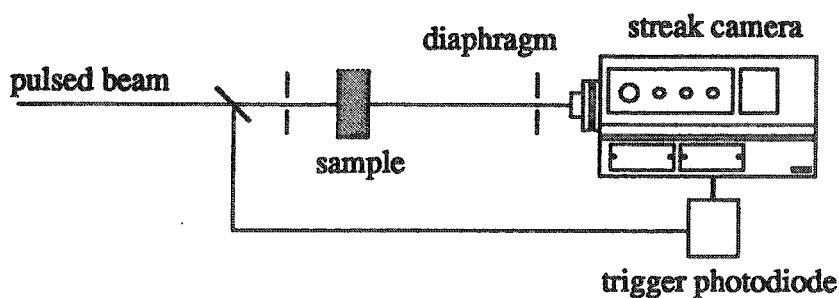


Fig. 4.10: experimental setting to measure the output pulses of scattering media.



The streak camera was a Hamamatsu C1587 Universal Streak Camera with a synchroscan unit M1955 set at 75.7474 [MHz] for an accurate triggering with the mode-locker driver.

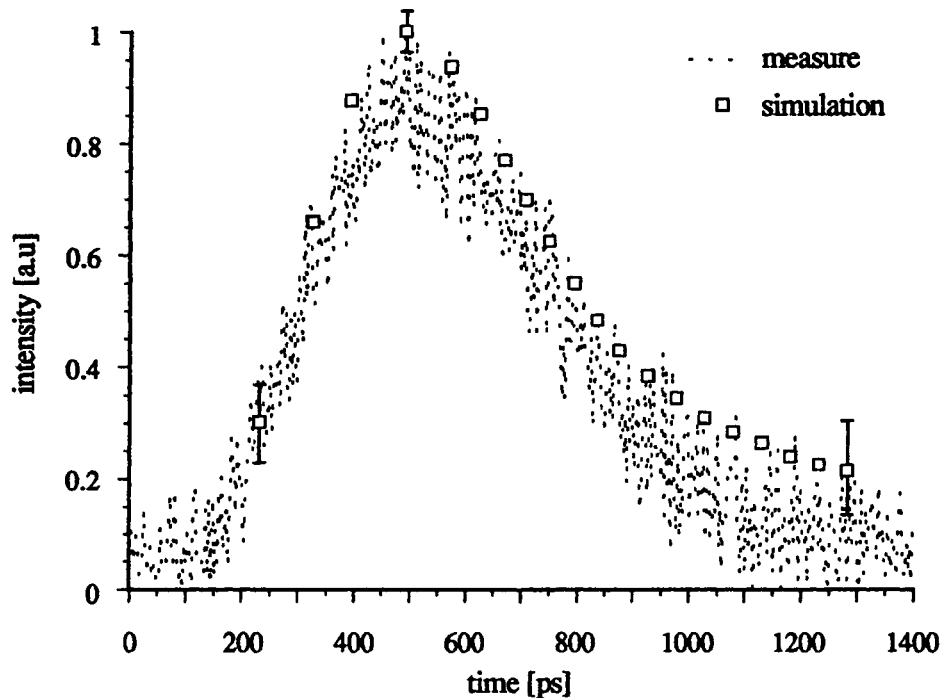


Fig. 4.11: plot of the measured output pulse (dotted line) and the simulated signal (data points) for a 20 [mm] thick slab of breast tissue containing mainly fat tissue.

The slight difference observable between the analytical curve and the measured curve (Fig. 4.11) is mainly due to the camera, indeed the camera gives a time-

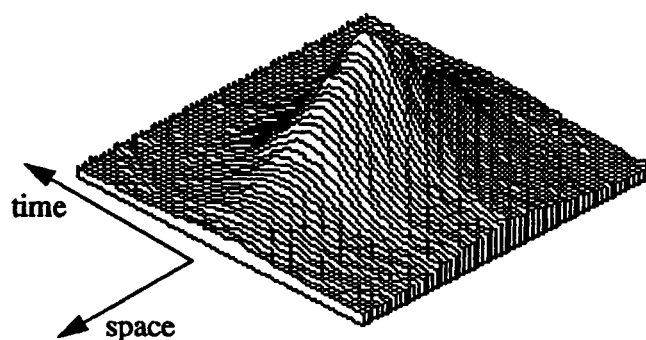


Fig. 4.12: profile of a measured pulse with the streak camera.

space image of the pulse, and the result is displayed as a spatial integral over the cross-section of the pulse. So that the slope looks slightly steeper than the one of the analytical curve.

Furthermore the mirror adjustment on the ion pump laser necessary to get the

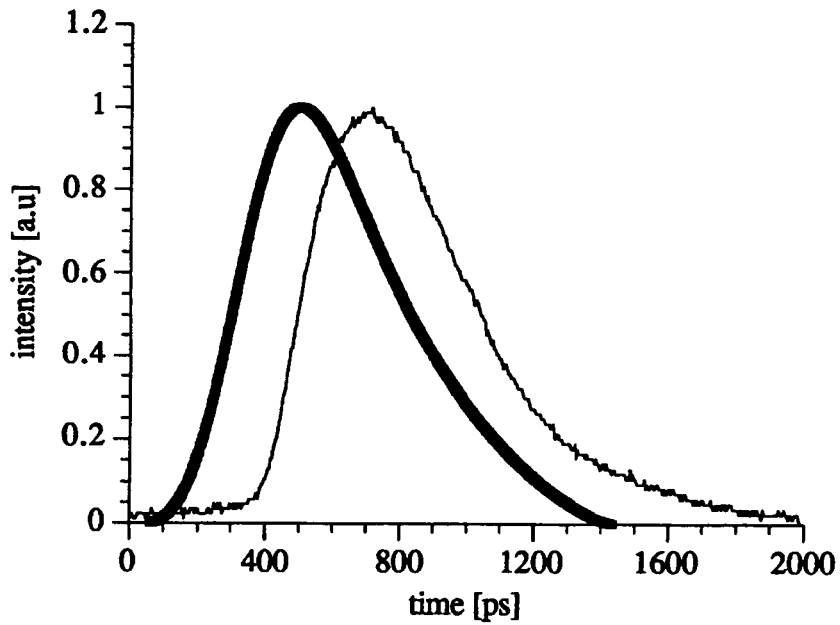


Fig. 4.13: plot of the measured output pulse through 10 [mm] of a 5% lipovenös solution (thin line) and the computed analytical solution (thick line).

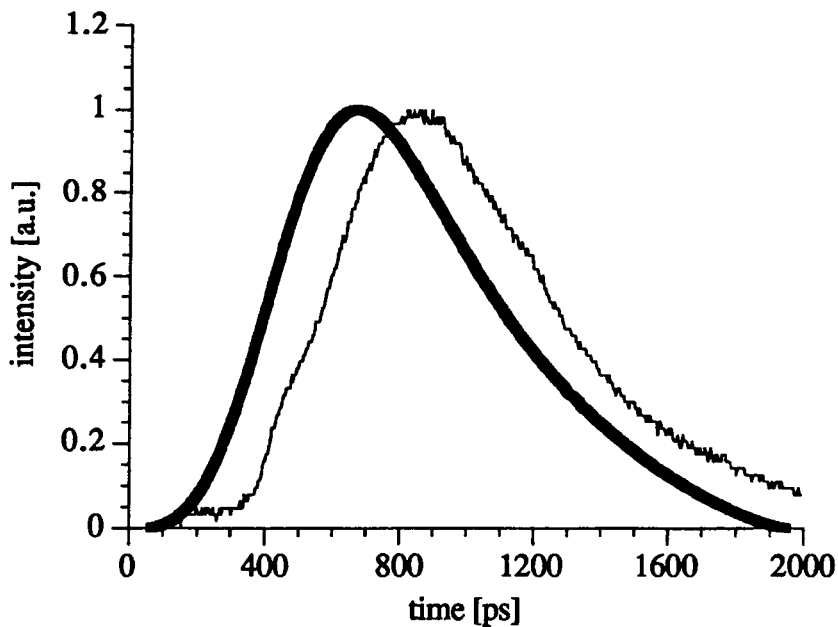


Fig. 4.14: plot of the measured output pulse through 10 [mm] of a 10% lipovenös solution (thin line) and the computed analytical solution (thick line).

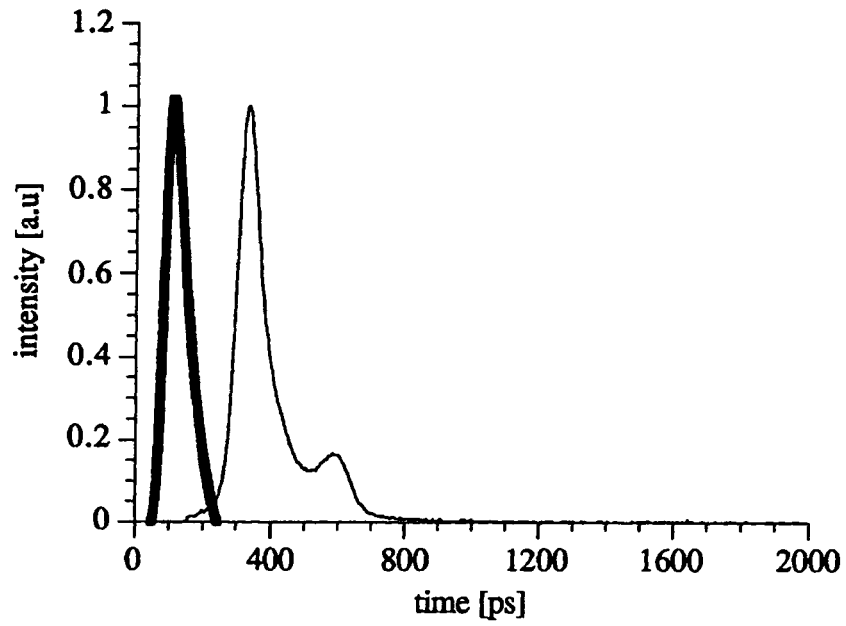


Fig. 4.15: plot of the measured output pulse through 5 [mm] of whole blood (thin line) and the computed analytical solution (thick line).

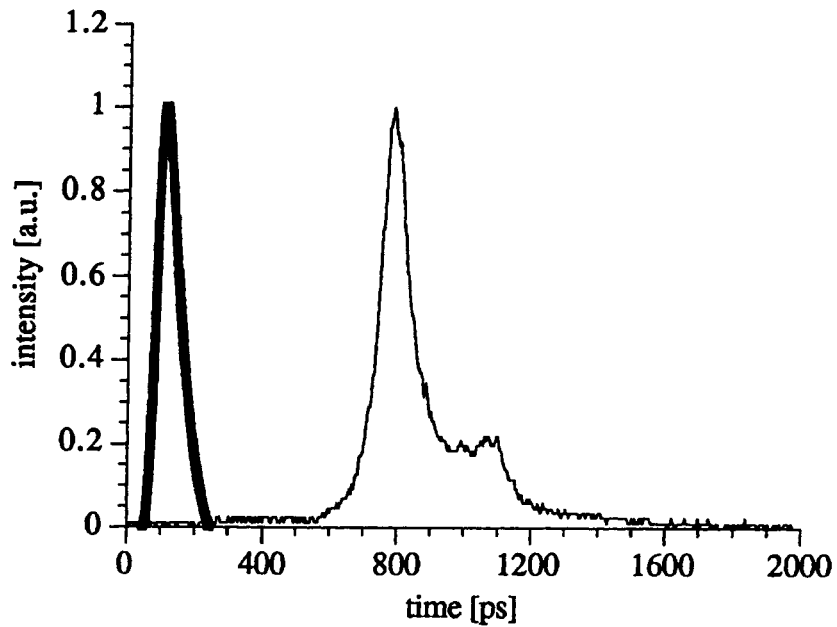


Fig. 4.16: plot of the measured output pulse through 10 [mm] of whole blood (thin line) and the computed analytical solution (thick line).

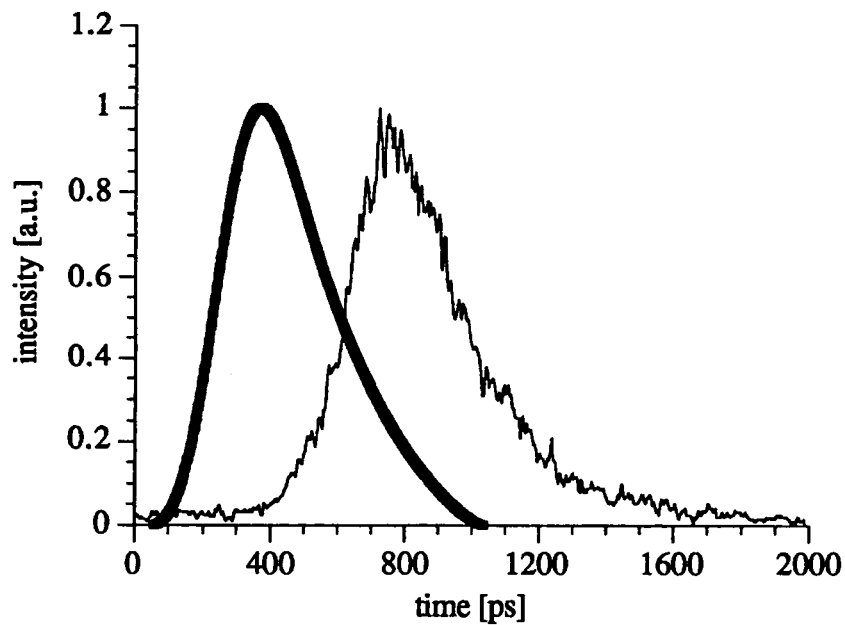


Fig. 4.17: plot of the measured output pulse through 20 [mm] of whole blood (thin line) and the computed analytical solution (thick line).

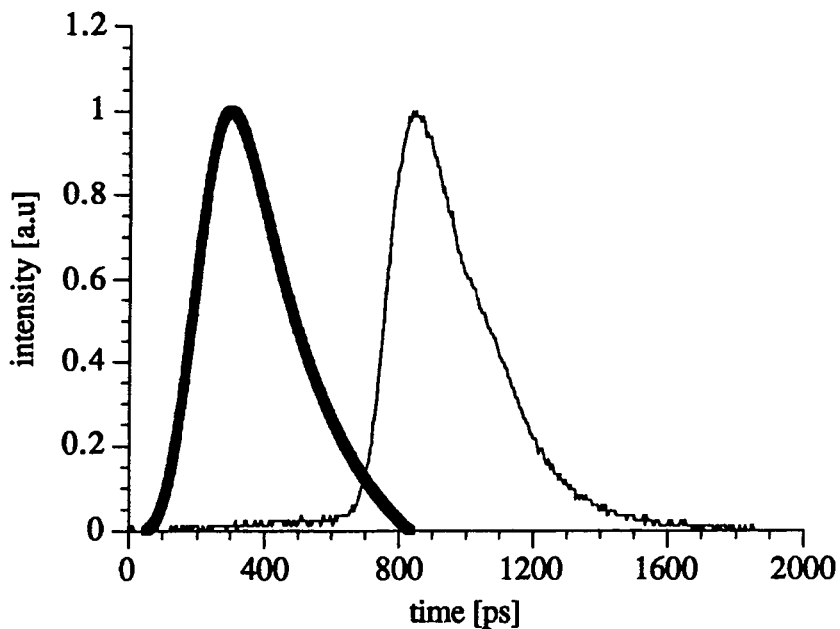


Fig. 4.18: plot of the measured output pulse through 10 [mm] of lung tissues (thin line) and the computed analytical solution (thick line).

towards a fast photodiode ( $\sim 70$  [ps] rise time) and the pulse is displayed on an oscilloscope with a sampling sweep unit and a 70 [ps] rise time sampling head. The travelling wave modulator is driven by a wave generator set at 2 [GHz] and a modulator driven by a delay generator which delivers 10 [ns] pulses. The signal is amplified by a 10 [W] power amplifier and finally delivered to the electro-optic modulator. In order to get a phase shift between the optical pulse and the modulation, the trigger signal from the mode-locker is delayed by a programmable delay generator. The whole electrical driving chain is triggered on the mode-locker driver.

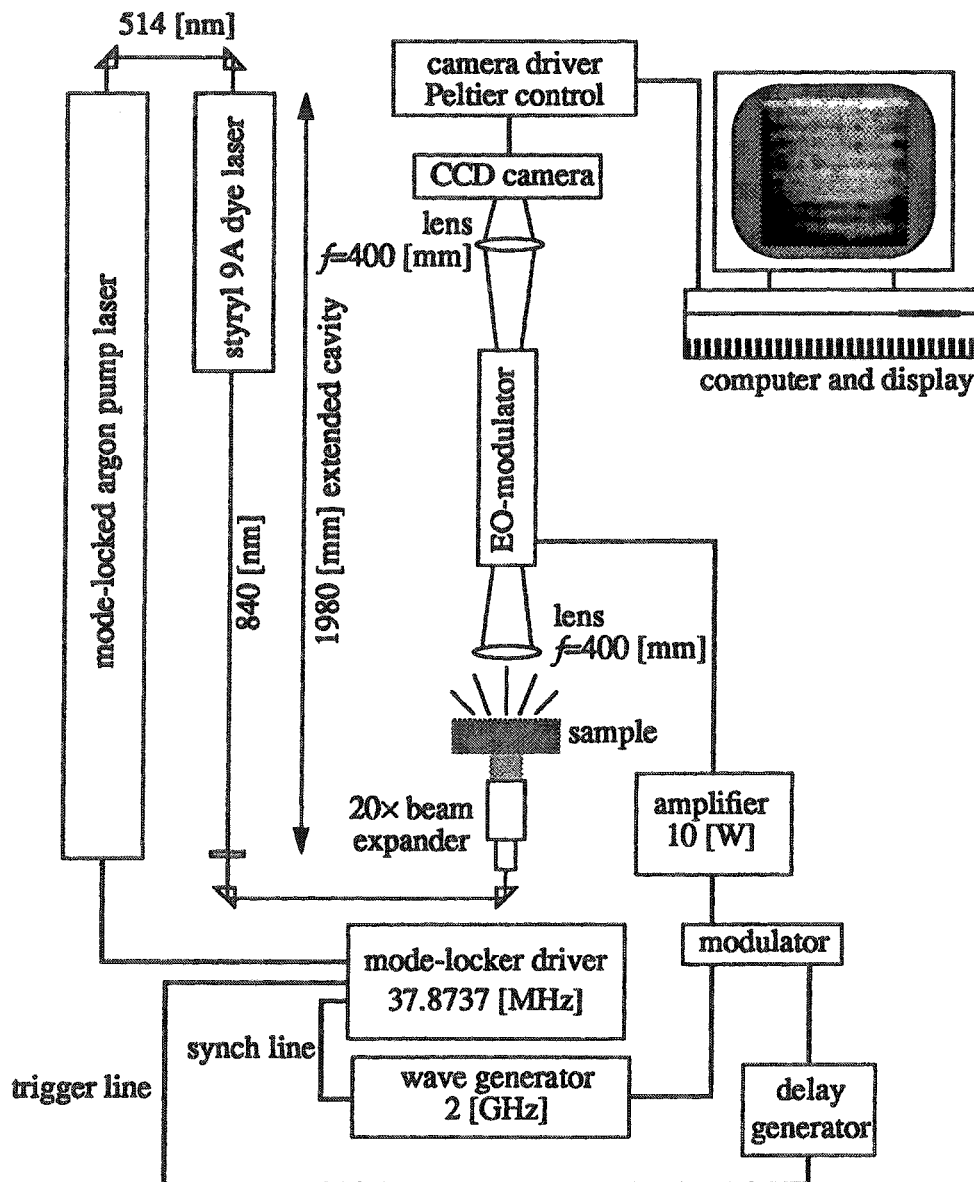


Fig. 4.20: experimental setting for time resolved transillumination.

narrowest incident pulse and the least jitter on the dye laser produced a secondary satellite pulse, which is observable on Fig. 4.13 to Fig. 4.18. The shift on the time scale between the theoretical and measured output pulses is due to the difficulty to have the 0 delay during measurements, which should be established from the ballistic transmission. Actually, no ballistic photons were detected by the streak camera, and the pulse had to be shifted in order to centre it on the display screen, so that only the pulse shape and pulsewidth are significant on the measurements.

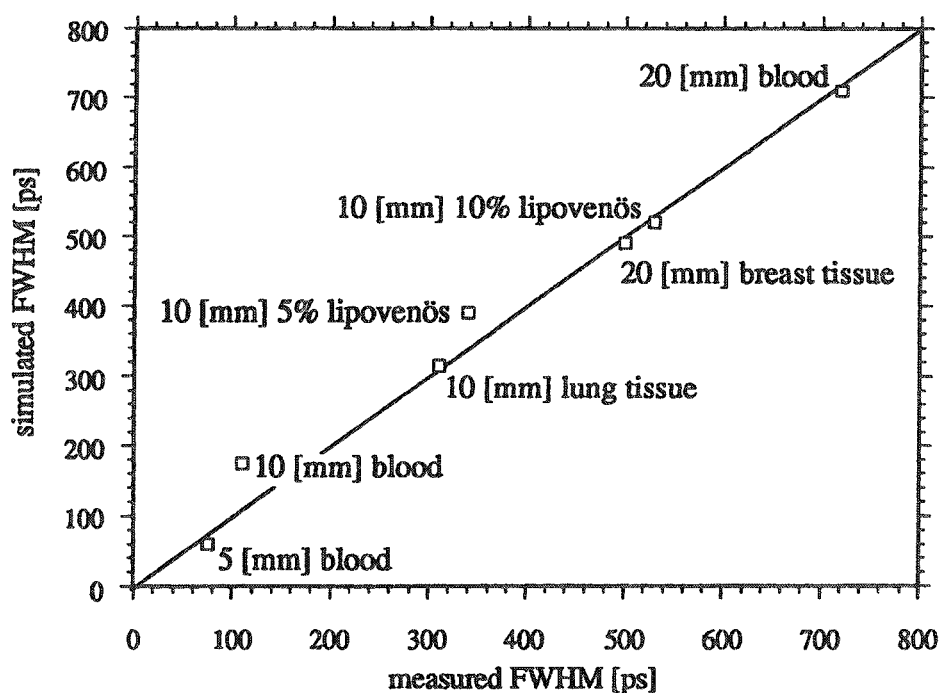


Fig. 4.19: comparative plot of the measured and simulated output pulse FWHM for the samples of the six preceding figures.

The comparative plot (Fig. 4.19) of the measured and simulated pulse FWHM show a good correspondency. The observable difference is mainly due to the laser jitter which was estimated at around 10 [ps] by measures of the source pulsewidth.

### 4.3.2. Pulse gating

With the experimental setting displayed in Fig. 4.20 and described in the preceding paragraphs, the gating of a 200 [ps] wide pulse has been made possible.

In order to detect the pulse, the principal beam is deviated by a beam splitter

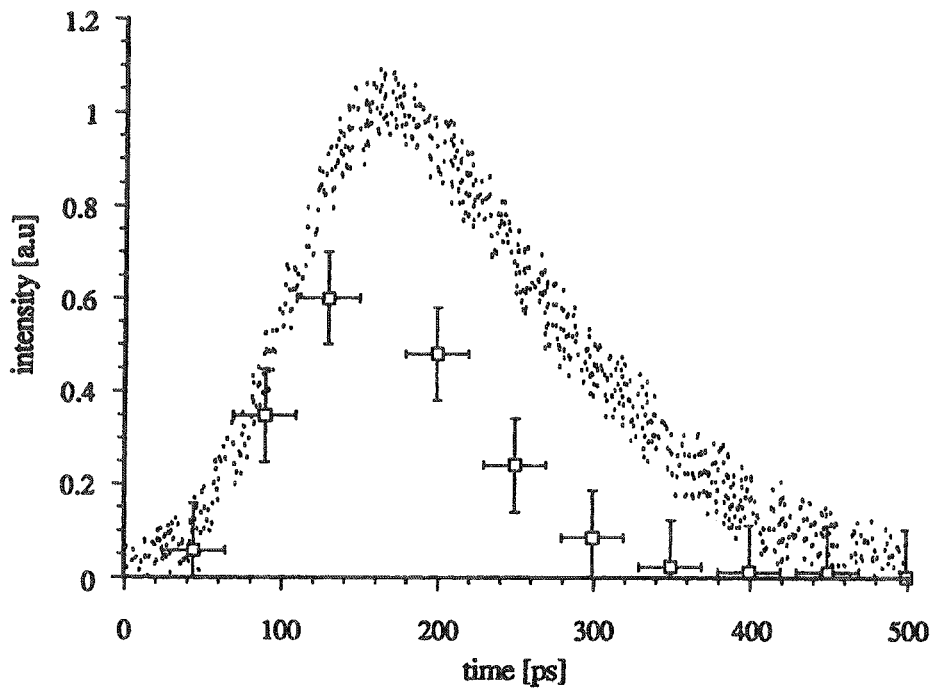


Fig. 4.21: plot of the measured modulated pulse (data points) for a delay estimated at 0 [ps] (0 phase shift).

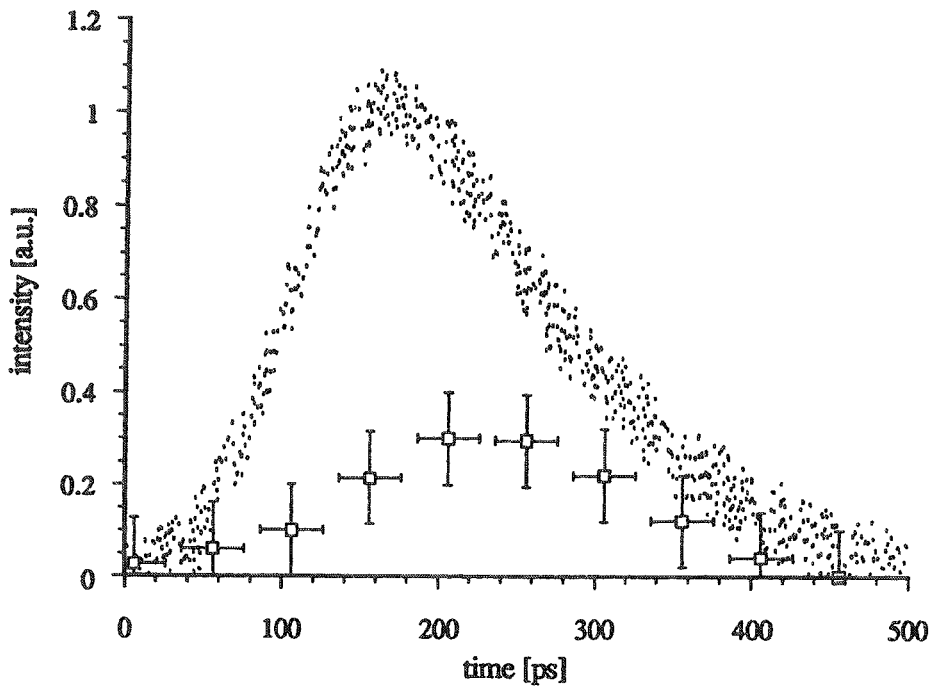


Fig. 4.22: plot of the measured modulated pulse (data points) for a delay estimated at 400 [ps] ( $3\pi/2$  phase shift).

The delay generator (Analog Device, AD9500, programmable delay generator) with a 10 [ps] resolution was able to give a  $\sim 25$  [ns] full-scale range delay with  $\sim 100$  [ps] increments, and the output pulses had an estimated FWHM of 10 [ns]. The circuit has been triggered at 37.87 [MHz], so that only one pulse out of two was modulated, thus giving a “modulated” signal as a combination between the unmodulated pulses and the modulated pulses (Fig. 4.21 and Fig. 4.22).

Further modulation tests have been done with various delays, but did not show significant changes in the shape of the modulated pulse, relatively to those displayed. According to the theoretical estimation of the delay (Fig. 4.8), the modulated pulse of Fig. 4.21 should correspond to a 0 [ps] delay or 0 phase shift and the modulated pulse of Fig. 4.22 to a  $\sim 400$  [ps] delay or  $3\pi/2$  phase shift. To get a more accurate determination of the gating, it would be necessary to use a jitter-free high frequency pulse generator with programmable delay in order to have a reliable modulation of the measured signal at 75.74 [MHz].

### 4.3.3. Image of a slit

To observe the effect of the modulation on the image resolution, a thin slit has been set on the illuminated surface of the breast sample (Fig. 4.23) and the image of the slit or the so called LSF has been recorded on the IR camera. The incident

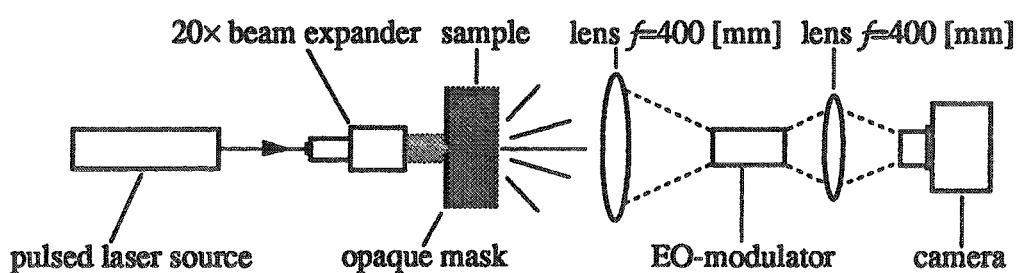


Fig. 4.23: experimental setting to observe the effect of time resolved imaging with the travelling wave modulator.

beam is broadened by a beam expander and illuminates the 20 [mm] thick breast sample through a 2 [mm] wide slit cut in an opaque mask. The transmitted light is collected by a lens focusing on the EO-modulator and finally the light is directed towards the IR camera by a second lens. The modulator acts as a spatial filter due to its small aperture and as a temporal filter when it is activated



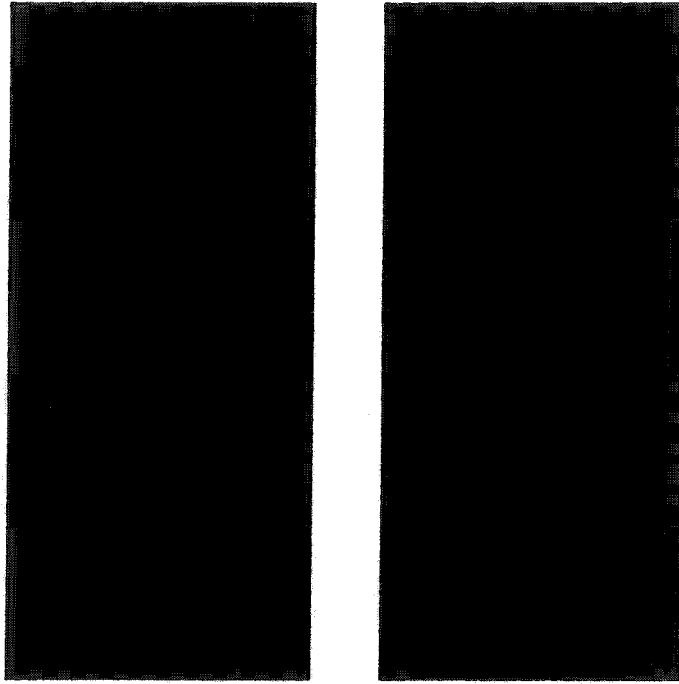


Fig. 4.24: image of a 2 [mm] slit or LSF.

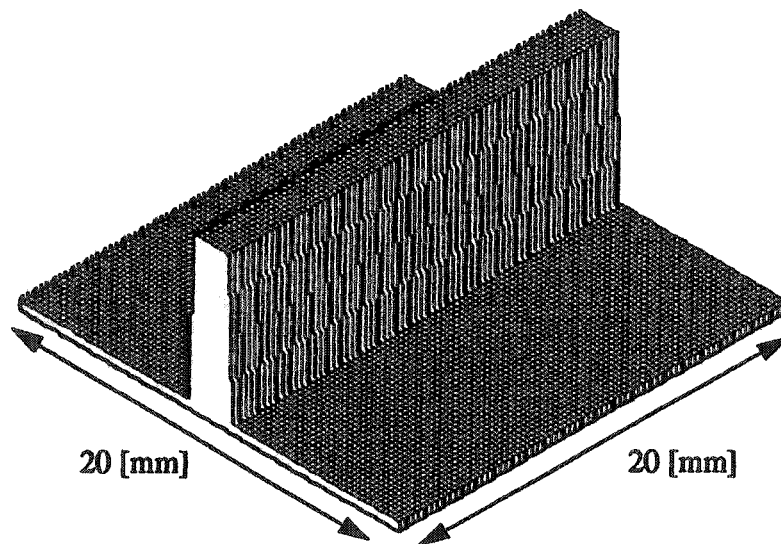


Fig. 4.25: perspective profile of the preceding image.

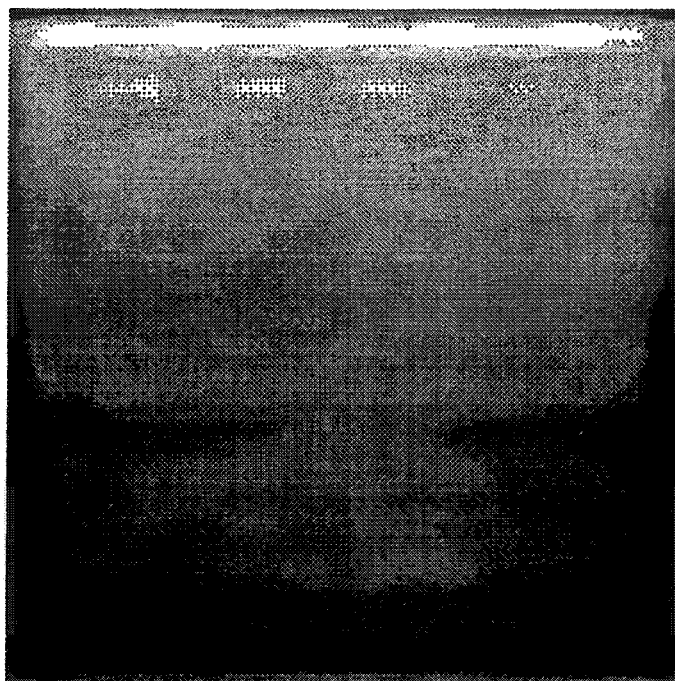


Fig. 4.26: image of a 2 [mm] slit or LSF for a 20 [mm] thick slab of breast tissue.

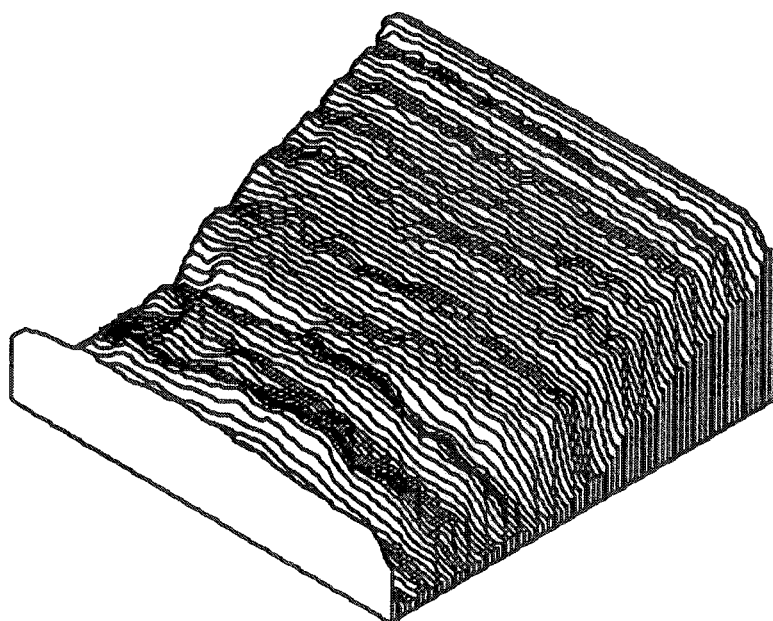
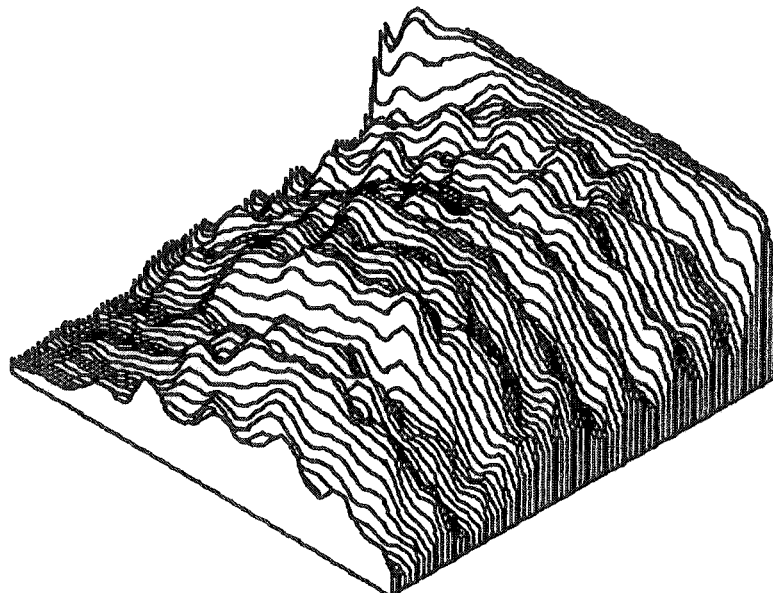


Fig. 4.27: perspective profile of the preceding image.



**Fig. 4.28:** time resolved image of a 2 [mm] slit or LSF for a 20 [mm] thick slab of breast tissue.



**Fig. 4.29:** perspective profile of the preceding image.

electrically.

The camera has been set with a gain of 50, approximately 10 [s] integration time and was cooled to 263 [°K]. The image of the slit has been recorded with the modulator in a passive state (no signal modulation, Fig. 4.26) and then with the most efficient modulation (Fig. 4.28) which has been estimated at 150 [ps]. The recorded images have been filtered in order to remove the unwanted high frequency noise by a low pass filtering, which gives a lower frequency aspect to the image. Furthermore, the images of the slit show a gradientlike behaviour on the slit axis. This is an artefact due to the camera. Actually the integration time is determined by the clock in the acquisition board, but the shutter which covers the CCD is manually driven, so that often the CCD is already in the read-out phase and it is still illuminated, so that irrelevant photons are recorded and contribute to the image principally in the last read lines. The wider part of the signal correspond to the most distant lines from the read-out line, the nearest appearing as the darkest one. The average equalised intensity profiles of the measured images (Fig. 4.26 and Fig. 4.28) are displayed in Fig. 4.30 to have a better illustration of the effect of time-gating.

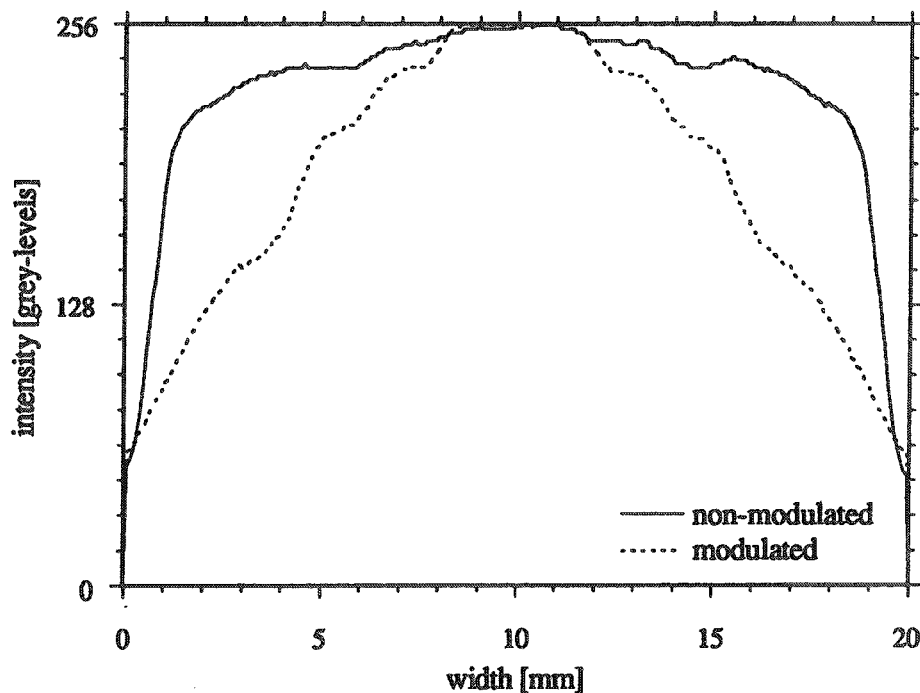


Fig. 4.30: average equalised intensity profiles of the non-modulated and modulated images of the 2 [mm] wide vertical slit through 20 [mm] of breast tissue.

Actually, shorter gating times than 150 [ps] could not be obtained due to the rise and fall time of the 2 [GHz] modulator, which is limited to 125 [ps] and only one pulse out of two were modulated, so that these results can not be associated to our theoretical predictions. Nevertheless, these results can be compared to the published data provided by Hebden and Kruger (1991) who measured with a streak camera, the edge spread function (ESF) of an opaque plane mask in the middle of a 50 [mm] wide cuvette filled with milk, as a function of the gating time. The estimated resolutions, which do not take into account the contrast and the noise, exhibit the same behaviour as our predictions except for the short gating times (below 120 [ps]), where the resolution decreases rapidly, suggesting that our predictions are pessimistic, probably due to a wrong evaluation of the noise contribution. Hebden and Kruger (1991) obtained an estimated resolution of 32 [mm] for the non time resolved signal and approximately 21.5 [mm] for a gating time of 150 [ps] which gives a 1.5 improvement compared to the 1.2 improvement of the FWHM of the intensity profiles displayed in Fig. 4.30, which are 19 [mm] for the non time resolved signal and 16 [mm] for the estimated 150 [ps] gating time in our measurements. The estimated FWHM for a 150 [ps] gating time with a modulation at the same repetition rate of the laser is approximately 13 [mm] (assuming that the measured time resolved signal is the mean between the non time resolved and the expected time resolved intensity profile), thus giving a 1.5 improvement, comparable to the published results.



## CHAPTER 5

# ***CONCLUSION***

This work has been dedicated to the study of light propagation through turbid media, and particularly of a light pulse through biological tissues, in order to illustrate the feasibility of a time resolved medical imaging device. This study has been directed by three main considerations:

- i) the *analytical modelling* based on the Boltzmann transport equation, which has given a preliminary qualitative description of the effect of a turbid medium on light propagation as well as the perturbative effect of an heterogeneity within a scattering slab,
- ii) then, the development of a *numerical Monte-Carlo simulation* has been able not only to describe precisely the multiple scattering process and the light pulse propagation but also to predict the effect of the noise during the imaging of an object embedded in a turbid medium,
- iii) finally *experimental measurements* on phantoms or biological tissues have confirmed both of the models and the theoretical predictions for time resolved imaging.

### **5.1. Analytical approach**

The analytical approach with the Boltzmann equation and the multiple scattering theory has been shown to be useful for providing qualitative informations about light transport through biological tissues. The solving of the Boltzmann equation with a collimated beam and the boundary conditions for a semi-infinite plane-parallel slab has provided a description of the transmitted and the backscattered light through simple equations. Then the perturbative effect of a spherical object within a slab has been determined and enabled the computing of the transmitted signal. Finally the pulse deformation due to scatterers and absorbers could be predicted with a fair accuracy. The analytical approach however, does not bring a precise quantitative description of the phenomenon, so that only the qualitative estimation could be made. Furthermore, the analytical solution takes in account the coherent transmission which is very weak through thick biological tissues, so that the accuracy of the analytical predictions is limited. Anyway, the equations are practical and versatile for the fast computing of the pulse form and the signal of an object embedded in a scattering medium.

### **5.2. Numerical approach**

A 3-D Monte-Carlo simulation has been developed to compute the photon distribution in biological tissues. This simulation has been tested with exact solutions and compared to preliminary exact measurements to assess its validity. The computing of the propagation of a light pulse enabled the confirmation of the analytical solution for the pulse form and the simulation of the time resolved detection showed that the blurring effect of multiple scattered photons could be improved by the time-gating, which conserve only the less scattered photons. However, the noise due to the small amount of detected photons because of the time-gating plays an important role in the degradation of the image quality, so that it has to be taken into consideration. With the image quality index theory combining the effect of the “natural” blurring due to scattering and the noise, the estimation of the smallest detectable spherical lesion could be computed and its value have been confirmed by published data. This value or IQI corresponding to a 4 [mm] lesion in a 40 [mm] thick slab is below the detection threshold



observed in classical diaphanography, which is around 15 to 20 [mm]. The limiting factor of our simulation has been the time consuming process and the modelling of the noise which could not be assessed by experimental data. Nevertheless, the Monte-Carlo simulation has shown to be a versatile and reliable tool for computing the light transport through biological tissue in various situation.

### **5.3. Experimental approach**

The measure of the optical properties of breast tissues showed that there is a differentiation between the healthy and the cancerous tissues. The exact values of the absorption and scattering coefficients have been compared to published data and are of the same order. Unfortunately it was impossible for us to get tissues containing only cancer, fat or fibrose, so that the measurements concerned particularly one type of tissue, but with presence of the others. Then the measurements of the transmitted pulses through various kinds and thicknesses of phantoms and biological tissues confirmed the simulation predictions. Finally the complete system for time resolved imaging with a travelling wave modulator enabled the observation of the pulse gating with different delays and the imaging of a slit showing an improvement with gated signals. The system has been limited by the gating system working at half the frequency of the pulsed source, so that only one pulse out of two has been modulated.

### **5.4. Perspective**

A further verification phase is necessary to evaluate experimentally the theoretical predictions. The Monte-Carlo simulation should be completed by adding some experimental data concerning the expected noise, as the anatomical noise or the eventual speckle noise, if any, thus making the IQI predictions more accurate and above all, more realistic.

For this purpose, the imaging system needs to be modified in order to allow use of a reliable, easy-to-use, medium power laser source as the Kerr mode-locked Ti:Sapphire in picosecond configuration (~1 [W] average power, 76 [MHz]

repetition rate and pulses 4 [ps] wide) as well as a jitter-free gating unit composed by the pulse generator at 76 [MHz] repetition rate so that every laser output pulse is gated.

Save these experimental considerations, a more fundamental study of laser-tissue interaction is necessary. Actually many investigators are only concerned by time-gated detection and often do not take into account the light transmission process through biological tissues. Thus, a systematic study of pulse propagation (at different wavelengths) through various types and thicknesses of biological samples should provide invaluable information on the real process of the pulse deformation during its flight through tissues as well as a new mean to characterise optically biological tissues by analysing the shape and amplitude of the output pulses. This conjugate time-of-flight and spectral study could not only concern breast tissues or breast lesions but also cerebral tissues, muscles, gonads, in order not only to provide information about the tissue itself and enable an early detection of lesions as haemorrhage, hypoxemia or cancer by differentiation of healthy and morbid tissues but also to investigate in metabolic changes by differential spectrophotometric studies. Furthermore, microscopic investigation of the multiple scattering process in tissue should provide a better comprehension of the phenomenon, hence the distribution, size and type of scatterers as well as absorbers.

Furthermore, investigation in the frequency-domain could be an interesting way to get another method for time-gated imaging or more precisely object location in scattering media. This method, compared to the time-domain imaging, which is based on measurements of only one parameter which is the time, provides two parameters which are the phase-shift and the amplitude modulation. With both of these parameters other useful information about the biological tissues and the propagation type of a modulated signal through tissues could be investigated. For example, it seems that the absorption coefficient, which is the most difficult coefficient to get due to its small value, could be exactly determined with frequency domain measurements.

Anyway, from my point of view, the fundamental study of the interaction between laser light and tissue is far more important than the development of a

time-gated imaging device. Actually a better comprehension of the light transport process through biological tissue would probably lead to new investigation methods or improve both sensitivity and specificity of imaging systems.



# **BIBLIOGRAPHY**

Anderson, R.R. and Parrish, J.A. (1981) The Optics of Human Skin. *The Journal of Investigative Dermatology*, 77, 13-19.

Andersson-Engels, S., Berg, R., Svanberg, S. and Jarlman, O. (1990) Time-resolved transillumination for medical diagnostics. *Optics Letters*, 15, 1179-1181.

Angquist, K.-A., Holmlund, D., Liliequist, B., Lindqvist, M. and Salemark, L. (1981) Diaphanopscopy and diaphanography for breast cancer detection in clinical practice. *Acta Chir. Scand.*, 147, 231-238.

Arfken, G. (1970) *Mathematical Methods for Physicists*. Academic Press, New-York.

Arnfield, M.R., Tulip, J. and McPhee, M.S. (1988) Optical Propagation in Tissue with Anisotropic Scattering. *IEEE Transactions on Biomedical Engineering*, 35, 372-381.

Arridge, S.R., van der Zee, P., Cope, M. and Delpy, D.T. (1990) New results for the development of infrared absorption imaging. *SPIE Biomedical Image processing*, 1245, 92-102.

Bachem, A. and Reed, C.I. (1931) The penetration of light through human skin. *Am J Physiol*, 97, 86-91.

Ballowitz, L. and Avery, M.E. (1970) Spectral reflectance of the skin. *Biol Neonate*, 15, 348-360.

Bartrum, R.J. and Crow, H.C. (1984) Transillumination Lightscanning to Diagnose Breast Cancer: a Feasibility Study. *AJR*, 142, 409-414.

Bays, R., Winterhalter, L., Funakubo, H., Monnier, P., Savary, M., Wagnières, G., Braichotte, D., Châtelain, A., van den Bergh, H., Svaasand, L. and Burckhardt, C.W. (1991) Clinical optical dose measurement for PDT: Invasive and non-invasive techniques. ,

Benaron, D.A. (1992) Two-D and three-D images of thick tissue using time-constrained times of flight and absorbance (tc-TOFA) spectrophotometry. *SPIE*, 164, 35-45.

Bevilacqua, F. (1991) Etude expérimentale de la lumière retrodiffusée à travers la peau. Diploma Work, Ecole Polytechnique Fédérale de Lausanne.

Blichert-Toft, M. (1984) Breast Conserving Treatment in Breast Cancer: Clinical and Psychological Aspects. In *Recent Results in Cancer Research*. (Eds.), Springer-Verlag Berlin, Heidelberg, 141-147.

Bohren, C.F. and Huffman, D.R. (1983) *Absorption and Scattering of Light by Small Particles*. J. W. a. Sons, New York.

Bolin, F.P., Preuss, L.E., Taylor, R.C. and Sandu, T.S. (1987) A Study of the Three-Dimensional Distribution of Light (632.8 nm) in Tissue. *IEEE Journal of Quantum Electronics*, QE 23, 1734-1738.

Bonner, R.F., Nossal, R., Havlin, S. and Weiss, G.H. (1987) Model for photon migration in turbid biological media. *JOSA A*, 4, 423-432.

Boreman, G.D. (1987) Fourier spectrum techniques for characterization of spatial noise in

imaging arrays. *Opt. Eng.*, 26, 985-991.

Browning, C.H. and Russ, S. (1917) The germicidal action of ultra-violet radiation, and its correlation with selective absorption. *Proc R Soc*, 90B, 33-38.

Brunsting, L.A. and Sheard, C. (1929) The color of the skin as analysed by spectrophotometric methods II. The rôle of pigmentation. *J Clin Invest*, 7, 575-591.

Brunsting, L.A. and Sheard, C. (1929) The color of the skin as analysed by spectrophotometric methods III. The rôle of superficial blood. *J Clin Invest*, 7, 593-613.

Buckley, W.R. and Grum, F. (1961) Reflectin spectrophotometry. *Arch Dermatol*, 83, 249-261.

Burns, D.A., Barlow, C.H., Maris, M., Holtom, G., Leigh, J.S. and Chance, B. (1989) Optical Tomography in Scattering Media: Image Enhancement using Redundant Apertured Optics. *IEEE Engineering in Medicine & Biology Society 11th annual international conference*, 367-368.

Carlsen, E. (1982) Transillumination Light Scanning. *Diagnostic Imaging*, 4, 26-60.

Chambettaz, F., Clivaz, X., Marquis, F. and Salathé, R.P. (1991) Temperature variations of reflection, transmission, and fluorescence of the arterial wall. , *Laser-Tissue Interaction II*, 1427, 134-140.

Chan, H.P., Doi, K., Galhotra, S., Vyborny, C.J., MacMahon, H. and Jokich, P.M. (1987) Image feature analysis and computed-aided diagnosis in digital radiography. I. Automated detection of microcalcifications in mammography. *Med. Phys.*, 14, 538-548.

Chen, H., Chen, Y., Dilworth, D., Leith, E., Lopez, J. and Valdmanis, J. (1991) Two-Dimensional Imaging through Diffusing Media Using 150-fs Gated Electronic Holography Technique. *Optics Letters*, 16, 487-489.

Cheong, W.-F., Prah, S.A. and Welch, A.J. (1990) A Review of the Optical Properties of Biological Tissues. *IEEE Journal of Quantum Electronics*, 26, 2166-2185.

Clivaz, X. (1992) Private communications.

Cope, M., Delpy, D.T., Reynolds, E.O.R., Wray, S., Wyatt, J. and van der Zee, P. (1988) Methods of quantitating cerebral near infrared spectroscopy data. *Adv. Exp. Med. Biol.*, 222, 183-189.

Cope, M. and Delpy, D.T. (1988) System for long-term measurement of cerebral blood and tissue oxygenation on newborn infants by near infra-red transillumination. *Med. & Biol. Eng. & Comput.*, 26, 289-294.

Cutler, M. (1929) Transillumination as an aid in the diagnosis of breast lesions. *Surg., Gynecol. Obstet.*, 48, 721-730.

Dawson, J.B., Barker, D.J., Ellis, D.J., Grassam, E., Cotterill, J.A., Fisher, G.W. and Feather, J.W. (1980) A theoretical and experimental study of light absorption and scattering by in vivo skin. *Phys Med Biol*, 25, 695-709.

de Haller, E.B. and Depeursinge, C. (1991) A sensor for cutaneous oximetry. *Innov. Tech. Biol. Med.*, 12, 89-97.

de Haller, E.B. and Depeursinge, C. (1992) Timer Resolved Breast Transillumination: a Preliminary Comparison between Monte Carlo Simulation and Measurements. *International*

Conference on Quantum Electronics Technical Digest series 1992, 9, 410.

de Haller, E.B. and Depeursinge, C. (1992) Time Resolved Transillumination: Simulation and Comparative Results. Proceedings of the 14th Annual International Conference of the IEEE EMBS, 14, 334-335.

de Haller, E.B. and Depeursinge, C. (1993) Simulation of the Time Resolved Breast Transillumination. Med. & Biol. Eng. & Comp., 31, in press.

Delpy, D.T., Cope, M., van der Zee, P., Arridge, S., Wray, S. and Wyatt, J. (1988) Estimation of optical pathlength through tissue from direct time of flight measurement. Phys. Med. Biol., 33, 1433-1442.

den Outer, P.N. (1992) Private communications.

DePalma, J.J. and Gasper, J. (1972) Determining the optical properties of photographic emulsions by the Monte Carlo method. Photogr. Sci. Eng., 16, 181-191.

Depeursinge, C., Desponds, L., Grecescu, M., Hessler, C., Raimondi, S., Sartoretti, P., Samiri, A. and Valley, J.-F. Theory and experience in the use of an image quality index in mammography and chest radiography.

Desponds, L. (1990) Private communications.

Desponds, L. (1991) Analyse de la performance de système d'imagerie radiologique avec application aux techniques mammographiques. Thesis No 928, Ecole Polytechnique Fédérale de Lausanne.

Desponds, L., Depeursinge, C., Grecescu, M., Hessler, C., Samiri, A. and Valley, J.-F. (1991) Image quality index (IQI) for screen-film mammography. Phys. Med. Biol., 36, 19-33.

DeVelis, J.B. and Reynolds, G.O. (1979) Fresnel Holography. in *Handbook of Optical Holography*, (Eds) Caulfield, H.J., Academic Press, New York, 139-155.

Dhawan, A.P., Gordon, R. and Rangayyan, R.M. (1984) Nevoscopy: Three-Dimensional Computed Tomography of Nevi and Melanomas In Situ by Transillumination. IEEE Transactions on Medical Imaging, MI-3, 54-61.

Diaspro, A., Bertolotto, M., Vergani, L. and Nicolini, C. (1991) Polarized Light Scattering of Nucleosomes and Polynucleosomes-In Situ and In Vitro Studies. IEEE Transactions on Biomedical Engineering, 38, 670-677.

Diels, J.-C. and Fontaine, J.J. (1983) Imaging with Short Optical Pulses. In *Optics and Lasers in Engineering*. (Eds.), 145-165.

Dilworth, D.S., Leith, E.N. and Lopez, J.L. (1990) Imaging absorbing structures within thick diffusing media. Appl. Opt., 29, 691-698.

Dingus, R.S. and Shafer, B.P. (1990) Laser-induced shock wave effects in materials. , *Laser-Tissue Interaction*, 1202, 36-45.

Drexler, B., Davis, J.L. and Schofield, G. (1985) Diaphanography in the Diagnosis of Breast Cancer. *Radiology*, 157, 41-44.

Dubois, F. and Ebbeni, J. (1984) Breast inspection by diaphanoscopy improved by use of optical fiber and pseudocolor processing. , *ECOOSA '84*, 492, 513-517.

- Duck, F.A. (1990) Optical Properties of Tissues. In Physical Properties of Tissues. (Eds.), New-York, 43-71.
- Duguay, M.A. and Hansen, J.W. (1969) An Ultrafast Light Gate. *Applied Physics Letters*, 15, 192-194.
- Duguay, M.A. and Hansen, J.W. (1969) Direct Measurement of Picosecond Lifetime. *Optics Communications*, 1, 254-256.
- Duguay, M.A. and Mattick, A.T. (1971) Ultrahigh Speed Photography of Picosecond Light Pulses and Echoes. *Applied Optics*, 10, 2162-2170.
- Edwards, E.A. and Duntley, S.Q. (1939) The pigments and color of living human skin. *Am J Anat*, 65, 1-33.
- Egan, W.G. and Hilgman, T.W. (1979) Absorbtion and Scattering Measurment Techniques. In *Optical Properties of Inhomogeneous Materials*. A. Press (Eds.), New-York, 61-72.
- Ehrhardt, J.C. (1986) Generation of pseuorandom numbers. *Med. Phys.*, 13, 240-241.
- Eichler, J., Knopf, J. and Lenz, H. (1977) Measurments on the Depth of Penetration of Light (0.35-1.0  $\mu\text{m}$ ) in Tissue. *Rad. and Environm. Biophys.*, 14, 239-242.
- Ertefai, S. and Profio, A.E. (1985) Spectral transmittance and contrast in breast diaphanography. *Med. Phys.*, 12, 393-400.
- Feig, S.A. (1984) Hypothetical Breast Cancer Risk from Mammography. In *Recent Results in Cancer Research*. (Eds.), Springer-Verlag Berlin, Heidelberg, 1-10.
- Feig, S.A. (1984) Benefits and Risks of Mammography. In *Recent Results in Cancer Research*. (Eds.), Springer-Verlag Berlin, Heidelberg, 12-27.
- Ferrari, M., De Marchis, C., Giannini, I., Di Nicola, A., Agostino, R., Nodari, S. and Bucci, G. (1986) Cerebral blood volume and hemoglobin oxygen saturation monitoring in neonatal brain by near IR spectroscopy. *Adv. Exp. Med. Biol.*, 200, 203-211.
- Ferrari, M., De Blasi, R.A., Bruscaioni, P., Barilli, M., Carraresi, L., Gurioli, M., Quaglia, E. and Zaccanti, G. (1991) Near infrared time-resolved spectroscopy and fast scanning spectrophotometry in ischemic human forearm. *SPIE proceedings on Time-Resolved Spectroscopy and Imaging of Tissues*, 1431, 276-283.
- Findlay, G.H. (1970) Blue skin. *Br J Dermatol*, 83, 127-134.
- Flock, S.T., Wilson, B.C. and Patterson, M.S. (1987) Total attenuation coefficient and scattering phase functions of tissues and phantom materials at 633 nm. *Med. Phys.*, 14, 835-841.
- Flock, S.T., Wilson, B.C. and Patterson, M.S. (1988) Hybrid Monte Carlo-Diffusion Theory Modelling of Light Distribution in Tissue. *SPIE Laser Interaction with Tissue*, 908, 20-28.
- Flock, S.T. (1988) Optical properties of tissues and light dosimetry at 633 nm. Thesis, MacMaster University.
- Flock, S.T., Patterson, M.S., Wilson, B.C. and Wyman, D.R. (1989) Monte-Carlo Modeling of Light Propagation in Highly Scattering Tissues-I: Model Predictions and Comparison with Diffusion Theory. *IEEE Transactions on Biomedical Engineering*, 36, 1162-1168.



- Flock, S.T., Wilson, B.C. and Patterson, M.S. (1989) Monte-Carlo Modeling of Light Propagation in Highly Scattering Tissues-II: Comparison with Measurements in Phantoms. *IEEE Transactions on Biomedical Engineering*, 36, 1169-1173.
- Flock, S.T. (1991) Private communications.
- Fodor, J., Malott, J.C. and Moskowitz, M. Diaphanography: Transillumination of the Breast. *Radiological Technology*, 55, 97-100.
- Fox, S.H., Moskowitz, M., Saenger, E.L., Kereiakes, J.G., Milbrath, J. and Goodman, M.W. (1978) Benefit/Risk Analysis of Aggressive Mammographic Screening. *Radiology*, 128, 359-365.
- Genton, C. (1992) Private communications.
- Geslien, G.E., Fisher, J.R. and DeLaney, C. (1985) Transillumination in Breast Cancer Detection. *AJR*, 144, 619-622.
- Gijsberg, G.H.M., Breederveld, D., van Gemert, M.J.C., Boon, T.A., Langelaar, J. and Rettschnick, P.H. (1986) In Vivo Fluorescence Excitation and Emission Spectra of Haematoporphyrin-Derivative. *Lasers in the Life Science*, 1, 29-48.
- Girolamo, R.F. and Gaythorpe, J.V. Clinical Diaphanography-Its Present Perspective. *CRC Critical Reviews in Oncology/Hematology*, 2, 1-31.
- Gisvold, J.J., Brown, L.R., Swee, R.G., Raygor, D.J., Dickerson, N. and Ranfranz, M.K. (1986) Comparison of Mammography and Transillumination Light Scanning in the Detection of Breast Lesions. *AJR*, 147, 191-194.
- Gold, R.H., Bassett, L.W. and Kimme-Smith, C. (1986) Progress in Clinical Radiology. *Investigative Radiology*, 21, 298-304.
- Gordy, E. and Drabkin, D.L. (1957) Spectrophotometric studies. *J. Biol. Chem.*, 285-299.
- Gradshteyn, I.S. and Ryzhik, I.M. (1965) Table of Integrals, Series and Products. Academic Press, New-York.
- Greene, F.L., Hicks, C., Eddy, V. and Davis, C. (1985) Mammography, Sonography, and Diaphanography (Lightscanning). *The American Surgeon*, 51, 58-60.
- Groenhuis, R.A.J., Ferwerda, H.A. and Ten Bosch, J.J. (1983) Scattering and absorption of turbid materials determined from reflection measurements. 1:Theory. *Applied Optics*, 22, 2456-2462.
- Groenhuis, R.A.J., Ten Bosch, J.J. and Ferwerda, H.A. (1983) Scattering and absorption of turbid materials determined from reflection measurements. 2:Measuring method and calibration. *Applied Optics*, 22, 2463-2467.
- Grossweiner, L.I., Karagiannes, J.L., Johnson, P.W. and Zhang, Z. (1990) Gaussian beam spread in biological tissues. *Applied Optics*, 29, 379-383.
- Guha, S.K. and Mahajan, S. (1983) Infrared reflectance from whole blood soaked filter paper and implications in haemoglobinometry. *Med. & Biol. Eng. & Comput.*, 21, 97-100.
- Gullino, P.M. (1977) Natural History of Breast Cancer. *Cancer*, 39, 2697-2703.
- Hardy, J.D. and Muschenheim, C. (1935) Radiation of heat from the human body. V. The

- transmission of infra-red radiation through the body. *J Clin Invest*, 15, 1-9.
- Hardy, J.D. (1939) The radiating power of human skin in the infra-red. *Am J Physiol*, 127, 454-462.
- Harris, J.L. (1964) Resolving power and decision theory. *JOSA*, 54, 606-611.
- Haselgrove, J.C., Leigh, J.S., Yee, C., Wang, N., Maris, M.B. and Chance, B.§. (1991) Monte Carlo and diffusion calculation of photon migration in noninfinite highly scattering media. *SPIE*, *SPIE Time-Resolved Spectroscopy and Imaging of Tissues*, 1431, 30-41.
- Hassab, J.C. and Boucher, B. (1975) Analysis of Signal Extraction, Echo Detection and Removal by Complex Cepstrum in Presence of Distortion and Noise. *Journal of Sound and Vibration*, 40, 321-335.
- Hasselbalch, K.A. (1911) Quantitative Untersuchungen über die Absorption der menschlichen Haut von ultravioletten Strahlen. *Skand Arch Physiol*, 25, 5-68.
- Hazeki, O., Seiyama, A. and Tamura, M. (1987) Near-Infrared Spectrophotometric Monitoring of Haemoglobin and Cytochrome a, a<sub>3</sub> in situ. *Adv. Exp. Med. Biol.*, 215, 283-289.
- Hebden, J.C. and Kruger, R.A. (1990) Transillumination imaging performance: Spatial resolution simulation studies. *Med. Phys.*, 17, 41-47.
- Hebden, J.C. and Kruger, R.A. (1990) Time-of-flight imaging of a simple breast phantom. , *Annual International Conference of the IEEE Engineering in Medicine and Biology Society*, 12, 1124-1125.
- Hebden, J.C. and Kruger, R.A. (1990) Transillumination imaging performance: A time-of-flight imaging system. *Med. Phys.*, 17, 351-356.
- Hebden, J.C. and Kruger, R.A. (1991) A time-of-flight breast imaging system: spatial resolution performance. *SPIE proceedings of Time-Resolved Spectroscopy and Imaging of Tissues*, 1431, 225-231.
- Hemenger, R.P. (1977) Optical properties of turbid media with specularly reflecting boundaries: applications to biological problems. *Applied Optics*, 16, 2007-2012.
- Henye, L.G. and Greenstein, J.L. (1941) *Diffuse Radiation of the Galaxy*.
- Hessler, C., Depeursinge, C., Grecescu, M., Pochon, Y., Raimondi, S. and Valley, J.-F. (1985) *Objective Assessment of Mammography Systems*  
Part I: Method. *Radiology*, 156, 215-219.
- Hessler, C., Depeursinge, C., Grecescu, M., Pochon, Y., Raimondi, S. and Valley, J.-F. (1985) *Objective Assessment of Mammography Systems*  
Part II: Implementation. *Radiology*, 156, 221-225.
- Inaba, H., Toida, M. and Ichimura, T. (1990) Optical Computer Assisted tomography realized by Coherent Detection Imaging (CDI) incorporating laser heterodyne method for biomedical applications. *SPIE Optical Systems in Adverse Environments*, 1399, 108-115.
- Isard, H.J. (1981) A Preliminary Appraisal of Diaphanography in Diseases of the Breast. *Cancer Detection and Prevention*, 4, 565-569.
- Isard, H.J. (1982) *Breast Disease and Correlation of Images: Mammography-Thermography-*

- Diaphanography. In *Biomedical Thermology*. I. Alan R. Liss (Eds.), New-York, 321-328.
- Ishimaru, A. (1978) *Wave Propagation and Scattering in Random Media*. Editor (Eds.), London.
- Jackson, P.C., Stevens, P.H., Smith, J.H., Kear, D., Key, H. and Wells, N.T. (1987) The development of a system for transillumination computed tomography. *The British Journal of Radiology*, 60, 375-380.
- Jacques, S.L., Alter, C.A. and Prahl, S.A. (1987) Angular Dependence of HeNe Laser Light Scattering by Human Dermis. *Lasers in Life Sciences*, 1, 309-333.
- Jacques, S.L. (1989) Time-Resolved Reflectance Spectroscopy in Turbid Tissues. *IEEE Transactions on Biomedical Engineering*, 36, 1155-1161.
- Jacques, S.L. (1989) Simple theory, measurements, and rules of thumb for dosimetry during photodynamic therapy. *SPIE Photodynamic Therapy: Mechanisms*, 1065, 100-108.
- Jacques, S.L. and Flock, S.T. (1991) Effect of surface boundary on time-resolved reflectance: measurements with a prototype endoscopic catheter. , *SPIE OE'Las'91*, 1431,
- Jain, R.K. and Ward-Hartley, K. (1984) Tumor Blood Flow-Characterization, Modifications, and Role in Hyperthermia. *IEEE Transactions on Sonics and Ultrasonics*, SU-31, 504-526.
- Johnson, C.C. (1970) Optical Diffusion in Blood. *IEEE Transactions on Bio-Medical Engineering*, BME-17, 129-133.
- Jones, C.H. (1982) Methods of Breast Imaging. *Phys. Med. Biol.*, 27, 463-499.
- Jöbsis, F.F. (1977) Noninvasive, Infrared Monitoring of Cerebral and Myocardial Oxygen Sufficiency and Circulatory Parameters. *Science*, 198, 1264-1267.
- Jöbsis-Vander Vliet, F.F. Non-invasive, near infrared monitoring of cellular oxygen. 833-841.
- Kalos, M.H. and Whitlock, P.A. (1986) *Monte Carlo Methods*. W. & sons, Editor (Eds.), New York.
- Kanamori, H. and Matsumoto, M. (1984) The information spectrum as a measure of radiographic image quality and system performance. *Phys. Med. Biol.*, 29, 303-313.
- Kaneko, M., Goto, S., Fukaya, T., Naito, M., Isoda, H., Kubota, G., Kitanaka, H., Takai, M., Hayashi, T., Hayakawa, T., Yamashita, Y. and Ohta, K. (1988) Fundamental Studies of Breast Tumor Detection with Narrow Beam Laser Scanning. *Radiation Medicine*, 6, 61-65.
- Karu, T.I., Kalendo, G.S., Lethokov, V.S. and Lobko, V.V. (1983) Biological action of low-intensity visible light on HeLa cells as a function of the coherence, dose, wavelength, and irradiation regime. II. *Sov. J. Quantum Electron.*, 13, 1169-1172.
- Karu, T.I. (1987) Photobiological Fundamentals of Low-Power Laser Therapy. *IEEE Journal of Quantum Electronics*, QE-23, 1703-1717.
- Karu, T.I. (1988) Molecular Mechanism of the Therapeutic Effects of Low-Intensity Laser Radiation. *Lasers in the Life Sciences*, 2, 53-74.
- Kawata, S., Touki, Y. and Minami, S. (1985) Optical Microscopic Tomography. *SPIE Inverse Optics II*, 558, 15-20.
- Kawata, S. and Minami, S. (1986) The principle and applications of optical microscope

- tomography. *Acta Histochem. Cytochem.*, 19, 73-81.
- Kemerait, R.C. and Childers, D.G. (1972) Signal Detection and Extraction by Cepstrum Techniques. *IEEE Transactions on Information Theory*, IT-18, 745-759.
- Knill, R.L., Clement, J.L., Kieraszewicz, H.T. and Dodgson, B.G. (1982) Assessment of Two Noninvasive Monitors of Arterial Oxygenation in Anaesthetized Man. *Anesth. Analg.*, 61, 582-586.
- Kollias, N. and Baqer, A. (1986) On the assessment of melanin in human skin in vivo. *Photochem Photobiol.*, 43, 49-54.
- Kopans, D.B. (1987) Nonmammographic Breast Imaging Techniques: Current Status and Future Developments. *The Radiologic Clinics of North America*, 25, 961-971.
- Kottler (1960) Turbid Media with Plane-Parallel Surfaces. *JOSA*, 50, 483-490.
- Kruger, R.A. and Hebden, C.H. (1990) Scanning methods for time-of-flight optical imaging. , Annual International Conference of the IEEE Engineering in Medicine and Biology Society, 12, 1122-1123.
- Kubelka, P. and Munk, F. (1931) Ein Beitrag zur Optik der Farbanstriche. *Zeitschrift für technische Optik*, II a, 593-601.
- Kubelka, P. (1948) New contribution to the optics of intensely light-scattering materials. Part I. *Journal of the Optical Society*, 38, 448-457.
- Kuznetov, A.I., Nadezdinsky, A.I. and Stepanov, E.V. (1990) Computerized infrared fiberoptic system for gas analysis based on diodes lasers. *SPIE Laser Surgery: Advanced Characterization, Therapeutics, and Systems II*, 1200, 476-479.
- Lafreniere, R., Ashkar, F.S. and Ketcham, A.S. (1986) Infrared Light Scanning of the Breast. *The American Surgeon*, 52, 123-128.
- Lamarque, J.L., Pujol, J., Guerrin, B., Cherif-Cheikh, J., Boulet, P., Laurent, J.C. and Mouron, M.Y. (1992) L'imagerie médicale dans le diagnostic des petits cancers. In *Certificat International des Maladies du Sein*. (Eds.), 146-154.
- Leith, E., Chen, H., Chen, Y., Dilworth, D., Lopez, J., Masri, R., Rudd, J. and Valdmanis, J. (1991) Electronic Holography for Imaging through Tissue using Picosecond Gated Pulses. *Optics & Photonics News*, 2, 39-40.
- Lenz, P. (1987) Light distributor for endoscopic photochemotherapy of tumors. *Appl. Opt.*, 26, 4452-4456.
- Lenz, P. (1987) High-efficiency Light Distributor for Endoscopic Photodynamic Therapy. *Lasers in Medical Science*, 2, 113-115.
- Lenz, P. (1989) Spatial light distribution in tumors: Phantom measurements. *Med. Phys.*, 16, 326-332.
- Lester, R.G. (1984) The contributions of radiology to the diagnosis, management, and cure of breast cancer. *Radiology*, 151, 1-7.
- Linford, J., Shalev, S. and Bews, J. (1986) Development of a tissue-equivalent phantom for diaphanography. *Med. Phys.*, 13, 869-875.

- Lippitsch, M.E. (1989) Organic dyes as nonlinear optical materials. *Applied Fluorescence Technology*, 1, 11-12.
- Longini, R.L. and Zrojkowski, R. (1968) A Note on the Theory of Backscattering of Light by Living Tissue. *IEEE Transactions on Bio-Medical Engineering*, BME-15, 4-10.
- Loo, L.N., Doi, K. and Metz, C.E. (1984) A comparison of physical image quality indices and observer performance in the radiographic detection of nylon beads. *Phys. Med. Biol.*, 29, 837-856.
- Lucas, N.S. (1931) IX The permeability of human epidermis to ultra-violet irradiation. *Biochem J*, 25, 57-70.
- Maarek, J.M., Jarry, G., de Cosnac, B., Lansart, A. and Bui, M.-H. (1984) A simulation method for the study of laser transillumination of biological tissues. *Annals of Biomedical Engineering*, 12, 281-304.
- Maarek, J.M., Jarry, G., Crowe, J., Bui, M.-H. and Laurent, D. (1986) Simulation of laser tomography in a heterogeneous biological medium. *Med. & Biol. Eng. & Comput.*, 24, 407-414.
- Marks, F.A. (1992) Optical determination of the hemoglobin oxygenation state of breast biopsies and human breast cancer xenografts in nude mice. *SPIE proceedings*, 1641, 227-237.
- Marquet, P. (1991) Etude théorique par la méthode de Monte Carlo de la lumière retrodiffusée à travers la peau. Diploma Work, Ecole Polytechnique Fédérale de Lausanne.
- Marshall, V., Williams, D. and Smith, K. (1984) Diaphanography as a Means of Detecting Breast Cancer. *Radiology*, 150, 339-343.
- Martin, J.E. (1983) Breast Imaging Techniques. *Radiologic Clinics of North America*, 21, 149-153.
- Marynissen, J.P.A. and Star, W.M. (1984) Phantom measurements for light dosimetry using isotropic and small aperture detectors. In *Porphyrin Localization and Treatment of Tumors*. I. Alan R. Liss (Eds.), 133-148.
- McCormick, P.W., Melville, S., Dujovny, M. and Ausman, J.I. (1990) Clinical Application of Diffuse Near Infrared Transmission Spectroscopy. *Hospimedica*, 39-47.
- McIntosh, D.M.F. (1983) Breast light scanning: A real time breast-imaging modality. *Journal of the Canadian Association of Radiologists*, 34, 288-290.
- McKenzie, A.L. and Carruth, J.A.S. (1984) Lasers in surgery and medicine. *Phys Med Biol*, 29, 619-641.
- McSweeney, M.B., Sprawls, P. and Egan, R.L. (1984) Enhanced-Image Mammography. In *Recent Results in Cancer Research*. (Eds.), Springer-Verlag, Heidelberg, 79-89.
- McSweeney, M.B. and Egan, R.L. (1984) Breast Cancer in the Younger Patient: A Preliminary Report. In *Recent Results in Cancer Research*. (Eds.), Springer-Verlag Berlin, Heidelberg, 36-40.
- Mendelson, Y. and Ochs, B.D. (1988) Noninvasive Pulse Oximetry Utilizing Skin Reflectance Photoplethysmography. *IEEE Transactions on Biomedical Engineering*, 35, 798-805.
- Merrit, C.R.B., Sullivan, M.A., Segaloff, A. and McKinnon, W.P. (1984) Real-time

- transillumination light scanning of the breast. *RadioGraphics*, 4, 989-1009.
- Metz, C.E. and Doi, K. (1979) Transfer Function Analysis of Radiographic Imaging Systems. *Phys. Med. Biol.*, 24, 1079-1106.
- Millis, R.R., Path, M.R.C., Davis, R. and Stacey, A.J. (1976) The detection and significance of calcifications in the breast: a radiological and pathological study. *British Journal of Radiology*, 49, 12-26.
- Monnier, P., Savary, M., Fontolliet, C., Waghières, G., Chatelain, A., Cornaz, P., Depeursinge, C. and van den Bergh, H. (1990) Photodetection and Photodynamic Therapy of "Early" Squamous Cell Carcinomas of the Pharynx, Oesophagus and Tracheo-bronchial Tree. *Lasers in Medical Science*, 5, 148-169.
- Monsees, B., Destouet, J.M. and Gersell, D. (1987) Light Scan Evaluation of Nonpalpable Breast Lesions. *Radiology*, 163, 467-470.
- Monsees, B., Destouet, J.M. and Totty, W.G. (1987) Light Scanning versus Mammography in Breast Cancer Detection. *Radiology*, 163, 463-465.
- Monsees, B., Destouet, J.M. and Gersell, D. (1987) Light Scan Evaluation of Nonpalpable Breast Lesions. *Radiology*, 163, 467-470.
- Monsees, B., Destouet, J.M. and Gersell, D. (1988) Light Scanning of Nonpalpable Breast Lesions: Reevaluation. *Radiology*, 167, 352.
- Morin, R.L., Raeside, D.E. and Goin, J.E. (1979) Monte carlo advice. *Med. Phys.*, 6, 305-306.
- Moskowitz, M., Feig, S.A., Cole-Beuglet, C., Fox, S.H., Habermann, J.D., Libshitz, H.I. and Zermeno, A. (1983) Evaluation of New Imaging Procedures for Breast Cancer: Proper Process. *AJR*, 140, 591-594.
- Muirhead, A. and Seright, W. (1984) Clinical experience with the diaphanograph machine. *Annals of the Royal College of Surgeons of England*, 66,
- Nakagawa, M., Arai, T., Suda, A., Kirushi, M., Murakoshi, S., Nakagawa, K., Hashimoto, M., Ueda, Y. and Shidara, M. (1990) Ablation Characteristics of Menisci by Various Laser Irradiation (193 nm-10.6 um), Pulsed and Continuous Wave. , *Laser Surgery: Advanced Characterization, Therapeutics and Systems II*, 1200, 190-196.
- Navarro, G.A. and Profio, A.E. (1988) Contrast in diaphanography of the breast. *Med. Phys.*, 15, 181-187.
- Nossal, R., Bonner, R.F. and Weiss, G.H. (1989) Influence of path length on remote optical sensing of properties of biological tissue. *Appl. Opt.*, 28, 2238-2244.
- Ohlsson, B., Gundersen, J. and Nilsson, D.-M. (1980) Diaphanography: A Method for Evaluation of the Female Breast. *World J. Surg.*, 4, 701-707.
- Orr, J.H. and Sliker, T.R. (1964) Linear Electro-Optic Effects in  $KH_2PO_4$  and Its Isomorphs. *Journal of the Optical Society of America*, 54, 1442-1444.
- Parsa, P., Jacques, S.L. and Nishioka, N.S. (1989) Optical properties of rat liver between 350 and 2200 nm. *Appl. Opt.*, 28, 2325-2329.
- Patterson, M.S., Chance, B. and Wilson, B.C. (1989) Time resolved reflectance and transmittance for the non-invasive measurement of tissue optical properties. *Appl. Opt.*, 28,

2331-2336.

Pearson, A.R. and Norris, R.E. (1933) The transmission of infra-red radiation through the horny layer of human skin. *Br J Radiol*, 6, 480-486.

Pedersen, G.D., McCormick, N.J. and Reynolds, L.O. (1976) Transport calculations for light scattering in blood. *Biophysical Journal*, 16, 199-207.

Peters, V.G., Wyman, D.R., Patterson, M.S. and Frank, G.L. (1990) Optical properties of normal and diseased human tissues in the visible and near-infrared. *Phys. Med. Biol.*, 35, 1317-1334.

Petrov, P.G. and Lopatin, V.V. (1986) Diffraction approximation in the tomography of absorbing objects. *Opt. Spectrosc.*, 61, 709-711.

Pochon, Y., Depeursinge, C., Hessler, C., Raimondi, S. and Valley, J.-F. (1982) Simultaneous objective measurements of dose and image quality in mammography. , *Applications of Optical Instrumentation in Medicine X*, 347, 238-245.

Pochon, Y. (1983) Objective criteria of quality in radiological images. Thesis No 479, Ecole Polytechnique Fédérale de Lausanne.

Prahl, S.A., Cheong, W.F., Yoon, G. and Welch, A.J. (1988) Optical properties of human aorta during low power argon laser irradiation. , *Laser Interaction with Tissue*, 908, 29-33.

Profio, A.E. and Khoury, T.F. (1988) Propagation of light in tissue for photodynamic therapy. , *Laser Interaction with Tissue*, 908, 94-97.

Quet, K.Y.T. (1990) Développement d'un modèle de propagation de la lumière visible et proche infrarouge dans les tissus: prévisions théoriques et vérifications expérimentales. Diploma Work, Ecole Polytechnique Fédérale de Lausanne.

Radda, G. (1983) Potential and limitations of nuclear magnetic resonance for the cardiologist. *Br Heart J*, 50, 197-201.

Rajagopalan, B., Blackledge, M., McKenna, W.J., Bolas, N. and Radda, G.K. Measurements of Phosphocreatine to ATP Ratio in Normal and Diseased Human Heart by Magnetic Resonance Spectroscopy Using the Rotating Frame-Depth Selection Technique. *Annals New-York Academy of Sciences*,

Rastegar, S., Motamedi, M., Welch, A.J. and Hayes, L.J. (1989) A Theoretical Study of the Effect of Optical Properties in Laser Ablation of Tissue. *IEEE Transactions on Biomedical Engineering*, 36, 1180-1187.

Reynolds, L., Johnson, C. and Ishimaru, A. (1976) Diffuse reflectance from a finite blood medium: application to the modeling of fiber optic catheter. *Applied Optics*, 15, 2059-2067.

Rol, P., Niederer, P., Frankhauser, F., Arigoni, M. and de Haller, E. (1990) Q-switched pulses and optical breakdown generation through optical fibers. *Laser and Light in Ophthalmology*, 3, 213-219.

Rose, A. (1948) The sensitivity performance of the human eye on an absolute scale. *J. Opt. Soc. Am.*, 38, 196-208.

Rose, A. (1973) *Vision: Human and Electronic*. Optical Physics and Engineering, W. L. Wolf, Editor (Eds.), New York.

- Rothenberg, L.N., Feig, S.A., Haus, A.G., Jans, R.G., Logan, W.W., Shore, R.E., Sickles, E.A., Stanton, L., Snyder, R.E., Masterson, M.E., Dodd, G.D., Gorson, R.O., Webster, E.W. and Spahn, J.A. (1986) *Mammography-A User's Guide*. NCRP Report No. 85, N. C. o. R. P. a. Measurements, Editor (Eds.), Bethesda.
- Russell, E.H. and Russell, W.K. (1933) *Ultra-violet Radiations and Actinotherapy*. Livingstone, Editor (Eds.), Edinburgh.
- Rymer, W.Z., Lin, S.F. and Wesselman, U. (1990) Therapeutic implications of nonablative laser application neurosurgery: future possibilities. *Laser Surgery: Advanced Characterization, Therapeutics, and Systems II*, 1200, 343-465.
- Saleh, B.E.A. and Teich, M.C. (1991) *Fundamentals of Photonics*. (Eds.) John Wiley and Sons, Inc., 72-78.
- Samid, D., Flessate, D.M., Miller, A.C. and Rimoldi, D. (1990) DNA damage and altered gene expression in cultured human skin fibroblasts exposed to 193 nm excimer laser radiation. , *Laser Tissue Interaction*, 1202, 281-285.
- Sandrik, J.M., Wagner, R.F. and Hanson, K.M. (1982) Radiographic screen-film noise power spectrum: calibration and intercomparison. *Appl. Opt.*, 21, 3597-3601.
- Schmitt, J.M., Mihm, F.G. and Meindl, J.D. (1986) New method for whole blood oximetry. *Annals of Biomedical Engineering*, 14, 35-52.
- Schmitt, J.M., Zhou, G.X. and Walker, E.C. (1990) Multilayer model of photon diffusion in skin. *JOSA A*, 7, 2141-2153.
- Schwartz, G.F., Feig, S.A., Rosenberg, A.L., Patchevsky, A.S. and Shaber, G.S. (1984) Localization and Significance of Clinically Occult Breast Lesions: Experience with 469 Needle-Guided Biopsies. In *Recent results in Cancer Research*. (Eds.), Springer-Verlag Berlin, Heidelberg, 125-132.
- Schwartz, G.F., Danoff, B.F., Feig, S.A., Rosenblum, H.M., Bloss, J.D. and Gall, J.R. (1984) The Selective Treatment of "Early" Carcinoma of the Breast by Lumpectomy, Level I Axillary Dissection, and Radiation Therapy. In *Recent results in Cancer Research*. (Eds.), Springer-Verlag Berlin, Heidelberg, 133-140.
- Seiyama, A., Hazeki, O. and Tamura, M. (1987) Simultaneous measurement of haemoglobin oxygenation of brain and skeletal muscle of rat in vivo by near-infrared spectrophotometry. *Adv. Exp. Med. Biol.*, 215, 291-295.
- Shalev, S., Linford, J., Bews, J. and Arenson, J. (1984) A close view at diaphanography. *IEEE Frontiers of Engineering and Computing Health Care*, 523-527.
- Shalev, S., Linford, J., Bews, J. and Arenson, J. (1985) The physical basis of diaphanography. , *Medical Imaging and Instrumentation*, 555, 109-115.
- Shapiro, S., Venet, W., Strax, P., Venet, L. and Roeser, R. (1982) Ten- to Fourteen-Year Effect of Screening on Breast Cancer Mortality. *JNCI*, 69, 349-355.
- Sherk, H.H., Rhodes, A. and Meller, M. (1990) *Lasers in Orthopedics*. , *Laser Surgery: Advanced Characterization, Therapeutics, and Systems II*, 1200, 221-223.
- Shimizu, K. and Ishimaru, A. (1978) Scattering Pattern Analysis of Bacteria. *Opt. Eng.*, 17, 129-134.



- Sickles, E.A. (1984) Breast Cancer Detection with Transillumination and Mammography. *AJR*, 142, 841-844.
- Sickles, E.A. (1985) Breast Imaging: A View from the Present to the Future. *Diagn. Imag. clin. Med.*, 54, 118-125.
- Sickles, E.A. (1987) Computed Tomography Scanning, Transillumination, and Magnetic Resonance Imaging of the Breast. In *Recent Results in Cancer Research*. S. Verlag (Eds.), Heidelberg, 31-36.
- Siegman, A.E. (1966) The Antenna Properties of Optical Heterodyne Receivers. *Appl. Opt.*, 5, 1588-1594.
- Sliney, D. and Wolbarsht, M. (1980) *Safety with Lasers and Other Optical Sources*. P. Press, Editor (Eds.), New York.
- Spears, K.G., Serafin, J., Abramson, N.H., Zhu, X. and Bjelkhagen, H. (1989) Chrono-Coherent Imaging for Medicine. *IEEE Transactions on Biomedical Engineering*, 36, 1210-1221.
- Splinter, R., Cheong, W.F., van Gemert, M.J.C. and Welch, A.J. (1989) In Vitro Optical Properties of Human and Canine Brain and Urinary Bladder Tissues at 633 nm. *Lasers in Surgery and Medicine*, 9, 37-41.
- Steinke, J.M. and Shepherd, A.P. (1986) Role of Light Scattering in whole Blood Oximetry. *IEEE Transactions on Biomedical Engineering*, BME-33, 294-301.
- Steinke, J.M. and Shepherd, A.P. (1987) Diffuse Reflectance of Whole Blood: Model for a Diverging Light Beam. *IEEE Transactions on Biomedical Engineering*, BME-34, 826-834.
- Steinke, J.M. and Shepherd, A.P. (1988) Comparison of Mie theory and the light scattering of red blood cells. *Appl. Opt.*, 27, 4027-4033.
- Sullivan, B.J. and A., H.J. (1989) Modeling and Analysis of CCI Holography. , *Engineering in Medicine & Biology Society*, 1181-1182.
- Svaasand, L.O. and Ellingen, R. (1985) Optical penetration in human intracranial tumors. *Photochem. & Photobiol.*, 41, 73-76.
- Tamura, T., Hazeki, O., Takada, M. and Tamura, M. Absorbance profile of red blood cell suspension in vitro and in situ. 211-217.
- Taylor, M.B. and Whitwam, J.G. (1986) The current status of pulse oximetry. *Anaesthesia*, 41, 943-949.
- Toida, M., Kondo, M., Ichimura, T. and Inaba, H. (1990) Experimental verification of image detection in highly scattering media using antenna properties of optical heterodyne microscope scheme. *Electronics Letters*, 26, 700-702.
- Toida, M., Kondo, M., Ichimura, T. and Inaba, H. (1991) Two-Dimensional Coherent Detection Imaging in Multiple Scattering Media Based on the Directional Resolution Capability of the Optical Heterodyne Method. *Appl. Phys. B*,
- Toida, M., Ichimura, T. and Inaba, H. (1991) The First Demonstration of Laser Computed Tomography Achieved by Coherent Detection Imaging Method for Biomedical Applications. *IEICE Transactions*, E 74, 1692-1694.

- Twersky, V. (1979) Propagation in Pair-Correlated Distributions of Small-Spaced Lossy Scatterers. *JOSA*, 69, 1567.
- van de Hulst, H.C. (1980) Multiple Light Scattering, Tables, Formulas, and Applications. Jovanovich, H.B., Academic Press (Eds.), London, Vol. 1 and Vol. 2.
- van der Zee, P. and Delpy, D.T. Simulation of the point spread function for light in tissue by a Monte Carlo method. 179-191.
- van der Zee, P. and Delpy, D.T. Computed point spread function for light in tissue using measured volume scattering function.
- van Gemert, M.J.C. and Star, W.M. (1987) Relations Between the Kubelka-Munk and the Transport Equation Models for Anisotropic Scattering. *Lasers in the Life Sciences*, 1, 287-298.
- van Gemert, M.J.C., Welch, A.J., Star, W.M. and Motamedi, M. (1987) Tissue Optics for a Slab Geometry in the Diffusion Approximation. *Lasers in Medical Science*, 2, 295-302.
- van Gemert, M.J.C., Jacques, S.L., Sterenborg, H.J.C.M., Star, W.M. and Welch, A.J. (1988) Analysis of light distribution in tissue. *SPIE*, 908, 12-19.
- van Gemert, M.J.C., Schets, G.A.C., Bishop, M.S., Cheong, W.-F. and Welch, A.J. (1988) Optics of Tissue in a Multi-Layer Slab Geometry. *Lasers in the Life Sciences*, 2, 1-18.
- van Gemert, M.J.C., Jacques, S.L., Sterenborg, H.J.C.M. and Star, W.M. (1989) Skin Optics. *IEEE*, 36, 1146-1154.
- Vaupel, P. (1990) Oxygenation of human tumors. *Strahlenther. Onkol.*, 166, 377-386.
- Wallberg, H., Alveryd, A. and Carlsson, K. (1985) Breast carcinoma and benign breast lesions. *Acta radiol. Diagnosis*, 26, 535-541.
- Wallberg, H. (1985) Diaphanography in various breast disorders. *Acta radiol. Diagnosis*, 26, 271-276.
- Wallberg, H., Alveryd, A., Nasiell, K., Sundelin, P., Bergvall, U. and Troell, S. (1985) Diaphanography in benign breast disorders. *Acta radiol. Diagnosis*, 26, 129-136.
- Wallberg, H., Alveryd, A., Bergvall, U., Nasiell, K., Sundelin, P. and Troell, S. (1985) Diaphanography in breast carcinoma. *Acta radiol. Diagnosis*, 26, 33-44.
- Wallberg, H., Alveryd, A., Sundelin, P. and Troell, S. (1986) The value of diaphanography as an adjunct to mammography in breast diagnostics. *Acta Chir. Scand.*, suppl., 530, 83-87.
- Wallis, C. (1991) A Puzzling Plague. *Time*, January 14, 32-36.
- Wan, S., Anderson, R.R. and Parrish, J.A. (1981) Analytical modelling for optical properties of the skin with in vitro and in vivo applications. *Photochem. & Photobiol.*, 34, 493-499.
- Wan, S., Parrish, J.A., Anderson, R.R. and Madden, M. (1981) Transmittance of nonionizing radiation in human tissues. *Photochem. & Photobiol.*, 34, 679-681.
- Wang, L., Ho, P.P., Liu, C., Zhang, G. and Alfano, R.R. (1991) Ballistic 2-D Imaging Through Scattering Walls Using an Ultrafast Optical Kerr Gate. *Science*, 253, 769-771.
- Wang, L., Liu, Y., Ho, P. and Alfano, R.R. (1991) Ballistic imaging of biomedical samples using picosecond optical Kerr gate. *SPIE*, *SPIE Time-Resolved Spectroscopy and Imaging of*

Tissues, 1431, 97-101.

Watmough, D.J. (1982) Diaphanography. *Acta Radiol. Oncol.*, 21, 11-15.

Watmough, D.J. (1983) Transillumination of Breast Tissue: Factors Governing Optimal Imaging of Lesions. *Radiology*, 147, 89-92.

Wichmann, B. and Hill, D. (1987) Building a random number. *Byte*, 127-128.

Wilksch, P.A. and Jacka, F. (1984) Studies of Light Propagation through Tissue. In *Porphyrim Localization and Treatment of Tumors*. I. Alan R. Liss (Eds.), 149-161.

Wilson, B.C., Patterson, M.S., Flock, S.T. and Wyman, D.R. Tissue optical properties in relation to light propagation models and in vivo dosimetry. In *Photon Migration in Tissues*. B. Chance (Eds.), New-York, 25-42.

Wilson, B.C. and Adam, G. (1983) A Monte Carlo model for the absorption and flux distribution of light in tissue. *Med. Phys.*, 10, 824-830.

Wilson, B.C., Jeeve, W.P. and Lowe, D.M. (1985) In vivo and post mortem measurements of the attenuation spectra of light in mammalian tissues. *Photochem. & Photobiol.*, 42, 153-162.

Wilson, B.C. and Patterson, M.S. (1986) The physics of photodynamic therapy. *Phys. Med. Biol.*, 31, 327-360.

Wilson, B.C., Patterson, M.S. and Flock, S.T. (1987) Indirect versus direct technologies for the measurement of the optical properties of tissues. *Photochem. & Photobiol.*, 36, 601-608.

Wilson, B.C. (1992) Private communications.

Wray, S., Cope, M., Delpy, D.T., Wyatt, J.S. and Reynolds, E.O.R. (1988) Characterization of the near infrared absorption spectra of cytochrome aa3 and haemoglobin for the non-invasive monitoring of cerebral oxygenation. *Biochim. & Biophys. Acta*, 933, 184-192.

Wyatt, P.J. (1968) Differential Light Scattering: a Physical Method for Identifying Bacterial Cells. *Appl. Opt.*, 7, 1879-1896.

Wyman, D.R., Patterson, M.S. and Wilson, B.C. (1989) Similarity Relations for anisotropic Scattering in Monte Carlo Simulations of Deeply Penetrating Neutral Particles. *Journal of Computational Physics*, 81, 137-150.

Yoo, K.M., Liu, F. and Alfano, R.R. (1990) Angle and time resolved studies of backscattering of light from biological tissues. *Laser-Tissue Interaction*, 1202, 260-271.

Yoo, K.M. and Alfano, R.R. (1990) Time-resolved coherent and incoherent components of forward light scattering in random media. *Optics Letters*, 15, 320-322.

Yoshiya, I., Shimada, Y. and Tanaka, K. (1980) Spectrophotometric monitoring of arterial oxygen saturation in the fingertip. *Med. & Biol. Eng. & Comput.*, 18, 27-32.

Zaccanti, G. (1991) Monte Carlo study of light propagation in optically thick media: point source case. *Applied Optics*, 30, 2031-2041.

Zaccanti, G., Brusaglioni, P., Ismaelli, A., Carraresi, L., Gurioli, M. and Wei, Q. (1992) Transmission of a pulsed thin light beam through turbid media: experimental results. *Applied Optics*, 31, 2141-2147.



# APPENDIX

## A.1. Tissue spectroscopy

Biological tissues can be characterised by their optical properties. Actually the light will propagate in different ways within tissues according to the kind of tissue and the wavelength. These properties are characterised by the absorption and the scattering. Light absorption occurs on discrete locations of the cells known as chromophores. Chromatin, cytochrome-aa<sub>3</sub>, haemoglobin or myoglobin are the most interesting pigments in the domain of tissue spectroscopy. Chromatin is located in the nucleus of the cell and is made of chromosomes during the cellular division. The cytochrome-aa<sub>3</sub> is localised in the mitochondrion and is the last link of the respiratory chain. Haemoglobin is the pigment of the red cells and binds oxygen for an active transport within the body. Myoglobin is the pigment of muscular cells and binds oxygen too, but its affinity for oxygen is higher in order to enable muscles to work during anaerobic cycles. The spectrum of myoglobin is fairly near to the haemoglobin spectrum. The three last cited pigments offer a supplementary property: their optical characteristics change as a function of the metabolism, whether the pigment is oxidised or reduced (Brunori et al., 1981, Wray et al., 1988, Fig. A.1).

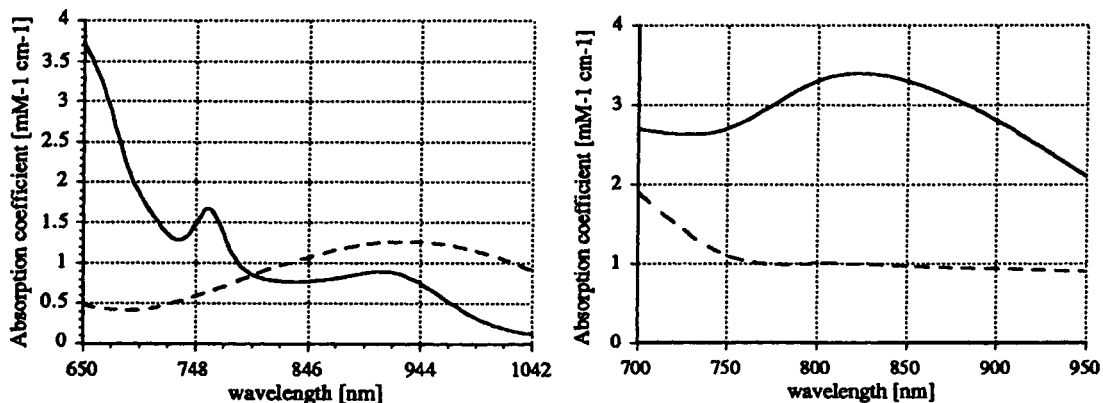


Fig. A.1: spectrum of both haemoglobin (Wray et al., 1988) and cytochrome (Brunori et al., 1981). The solid line describes the reduced state and the dashed line the oxidised state.

The study of the optical properties of biological tissue has a history of many decades and F.A. Duck (1990) did a concise review. K.A. Hasselbalch (1911) made early studies of ultraviolet transmission through the skin. C.H. Browning

and S. Russ (1917) noted the greater light penetration in the range 290 [nm] to 380 [nm] in comparison with that at shorter wavelengths. The penetration through skin by ultraviolet radiation was studied further by N.S. Lucas (1930), and by A. Bachem and C.I. Reed (1931), and by the early 1930s good data on optical transmission, absorption and fluorescence of tissue were available (Russell and Russell, 1933). Early studies on the properties of skin in the IR range were reported by Hardy (Hardy and Muschenheim, 1935, Hardy, 1939), and by Pearson and Norris (1933). Spectrophotometric studies of the colour of human skin were widely reported, including its dependence on pigmentation (Brunsting and Sheard, 1929, Edwards and Duntley, 1939), and on blood supply (Brunsting and Sheard, 1929, Gordy and Drabkin, 1957). The investigation of skin pigmentation and the estimation of melanin concentration has continued to attract considerable interest (Buckley and Grum, 1961, Findlay, 1966, Ballowitz and Avery, 1970, Dawson et al., 1980, Kollias and Baqer, 1986). Whilst the early studies were instructive in establishing the general spectral characteristics of skin, their use as quantitative sources of data must be questioned. This mainly results from the use of inadequate instrumentation failing to account precisely for the diffuse nature of the transmission of light through tissue. There are two main sources of inaccuracy. Firstly off-axis scattered radiation may be totally internally reflected within the sample, and so be lost to the measurement. The second problem is that of autofluorescence.

A lot of useful reviews of the optical properties of tissue have been published, generally written in a particular clinical context. Wilson and Patterson (1986) reviewed the physics of photodynamic therapy, and McKenzie and Carruth (1984) have discussed aspects of the use of lasers in medicine. The optical properties of the tissues of the skin and the eye have been discussed in the context of safety by Sliney and Wolbarsht (1980), and skin optics was reviewed by Anderson and Parrish (1981, 1982), and by van Gemert et al. (1989).

## A.2. Optical oximetry

Optical oximetry is a method to determine the oxygen saturation of blood or tissues in order to control metabolism. Former techniques were based on blood sample gasometry or tissue oxygen determination with Clark electrodes in needles (Taylor and Whitwam, 1986). These both techniques are invasive and do not allow an accurate continuous monitoring. With the increasing knowledge on tissue optics and spectroscopy (Wood and Geraci, 1949, Gordy and Drabkin, 1956, van Assendelft, 1970, Stryer, 1975) a spectrophotometric study of tissue is made possible. Since certain pigments possess a redox dependent absorption band in the spectral range from far red to NIR frequencies, it is useful to exploit that property to develop a non-invasive method to monitor oxygen delivery to tissues. Optical oximetry is then non-invasive, convenient, safe and allows a continuous monitoring at the bedside.

Hypoxemia or oxygen deficiency of tissues is a major cause of morbidity and lead to death in most humans. Respiratory dysfunction inducing hypoxemia may depend on oxygen supply, cardiac output and oxygen affinity of red cells which depend on functional haemoglobin and oxygen partial pressure. The risk of hypoxemia is encountered in surgery, where the anaesthetist has to continually control oxygen supply and to detect respiratory failure as soon as possible. Furthermore, hypoxemia is the major cause of handicap or death in the newborns. Thus a continuous monitoring of brain oxygenation allows an early prevention of irreversible damage.

Two measuring techniques has to be distinguished, the pulsed oximetry and the tissular oximetry (Fig. A.2). The former is widely applied to blood oxygen

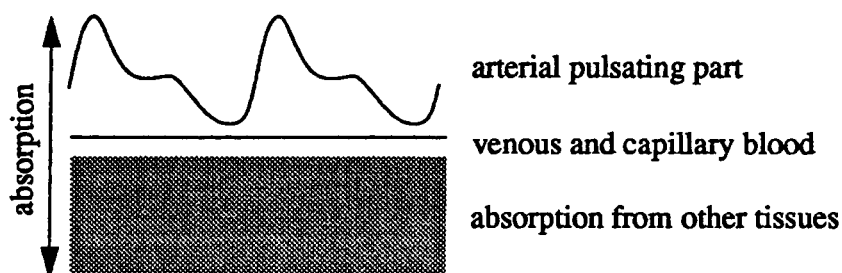


Fig. A.2: absorption and modulation of incident light through body tissues.

saturation determination. In this case, only a pulsating signal is detected (Nakajima et al., 1975, Yoshiya et al., 1980, Knill et al., 1982). Pulsed oximetry allows not only oxygen saturation monitoring but also qualitative plethysmography is simultaneously performed (Taylor and Whitwam, 1986, Mendelson and Ochs, 1988). The latter is a new technique aiming at a reliable determination of the effective oxygenation of tissues, using the AC (plethysmographic) component of blood. Most of the tissues are well irrigated, thus a tissular measure is blurred by the blood signal. This method enables the evaluation of brain oxygenation (Jöbsis and Vliet, 1977, Taylor and Whitwam, 1986, Cope and Delpy, 1988) as well as muscle oxygenation (Seiyama et al., 1987).

In practice, the method relies on the Beer-Lambert law  $I=I_0 10^{-\epsilon cz}$  (where  $I$  is the transmitted intensity,  $I_0$  the incident intensity,  $\epsilon$  the extinction coefficient,  $c$  the concentration of pigments and  $z$  the slab thickness) and the definition of the optical density  $D=-\log I/I_0$ . Thus the oxygen saturation is determined by transillumination on two or more wavelengths with Eq. A.1.

$$S_{O_2} = 100 \frac{\frac{D_1}{D_2} - \frac{\epsilon_{1A}}{\epsilon_{2B}}}{\frac{D_1}{D_2} \left(1 - \frac{\epsilon_{2A}}{\epsilon_{2B}}\right) + \left(\frac{\epsilon_{1A} - \epsilon_{1B}}{\epsilon_{2B}}\right)} \quad \text{Eq. A.1}$$

The indices of the optical density  $D$  and the extinction  $\epsilon$  are related to the metabolic state ( $A$  for oxidised and  $B$  for reduced) and to the wavelength (1 for wavelength 1 and 2 for wavelength 2). In the case of haemoglobin, there is an isobestic point at 805 [nm], i.e. the curves of the oxidised and the reduced state crosses each other ( $\epsilon_A=\epsilon_B$ , see Fig. A.1). Thus Eq. A.1 is simplified and the expression for the oxygen saturation is:

$$S_{O_2} = 100 \frac{\frac{D_1}{D_2} - \frac{\epsilon_{1A}}{\epsilon_{2B}}}{\left(\frac{\epsilon_{1A} - \epsilon_{1B}}{\epsilon_{2B}}\right)} \quad \text{Eq. A.2}$$



## Oximeter:

The oximeter consists of a probe, a processor and display components (Fig. A.3). The *probe* includes two or more sequenced pulsed light sources (bulbs with filters, LED or laser diodes) which illuminates a portion of tissue via a fibre optics bundle to avoid heating of the investigated area, and a photodiode which collects the transmitted or backscattered light simultaneously. The *processor* is part of the switching device and drives the light sources. It sequences alternate pulses to each source and collect the signal from the photodiode with distinction of each wavelength. The commutation board is connected to a microcomputer which allows the computing of the oxygen saturation and the *display* of the results. The wavelengths are chosen according to the most significant pigment

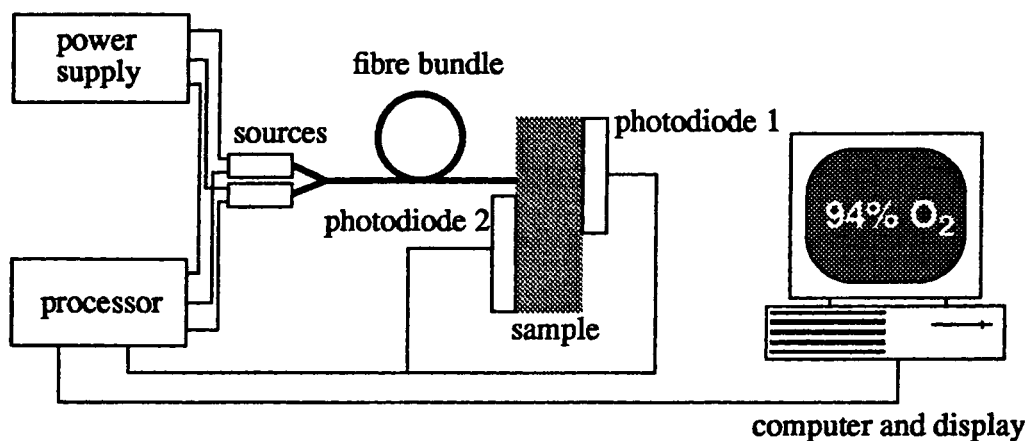


Fig. A.3: schematic of the optical oximeter with setting for transmission oximetry (photodiode 1) and reflectance oximetry (photodiode 2).

found in the illuminated cells.

A tissular transmission oximeter has been developed to detect oxygen insufficiency in rat muscles (de Haller and Depeursinge, 1991). A host of rats had their left femoral artery ligatured in order to induce ischaemia in the left paw, the right paw approximating the healthy state. To avoid disturbing movements of rats, the animals were anaesthetised before measuring and maintained at a constant temperature (room temperature). The thickness of the rat paw (approximately 15 [mm]) damps efficiently the pulsated part of arterial circulation, so that the muscle oxygenation is measured with the blood perfusion.

To get significant results (rats are supposed to grow peripheral circulation in case of lesions) the rats were forced to run on a mill-machine. The comparative measure between left and right paw was done on anaesthetised rats before and after running (Fig. A.4). The results show a difference due to effort. Further the

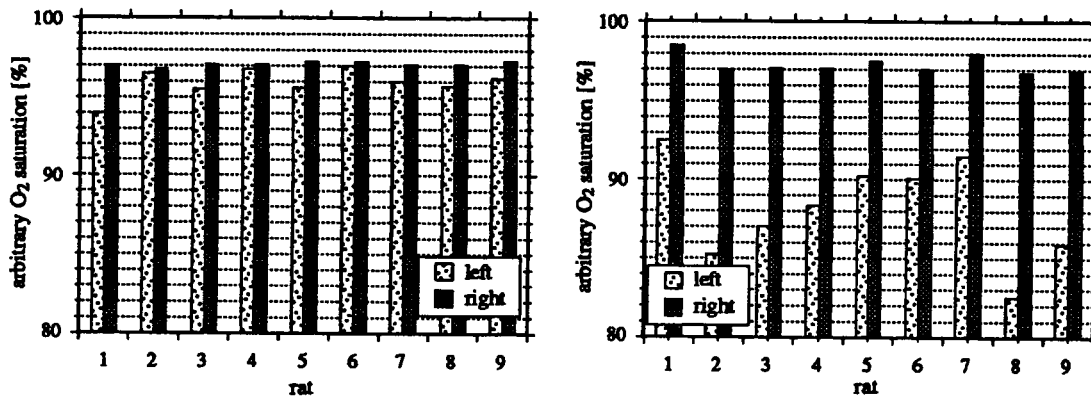


Fig. A.4: plot of the  $O_2$  saturation of both left and right paw of rats before (at right) and after (at left) effort (from de Haller and Depeursinge, 1991).

oximeter has been transformed to a reflectance oximeter to get muscular oxygenation on humans. In order to have reliable results with Eq. A.1 or Eq. A.2, the reflectance oximeter had to follow a Beer-Lambert law as a function of the

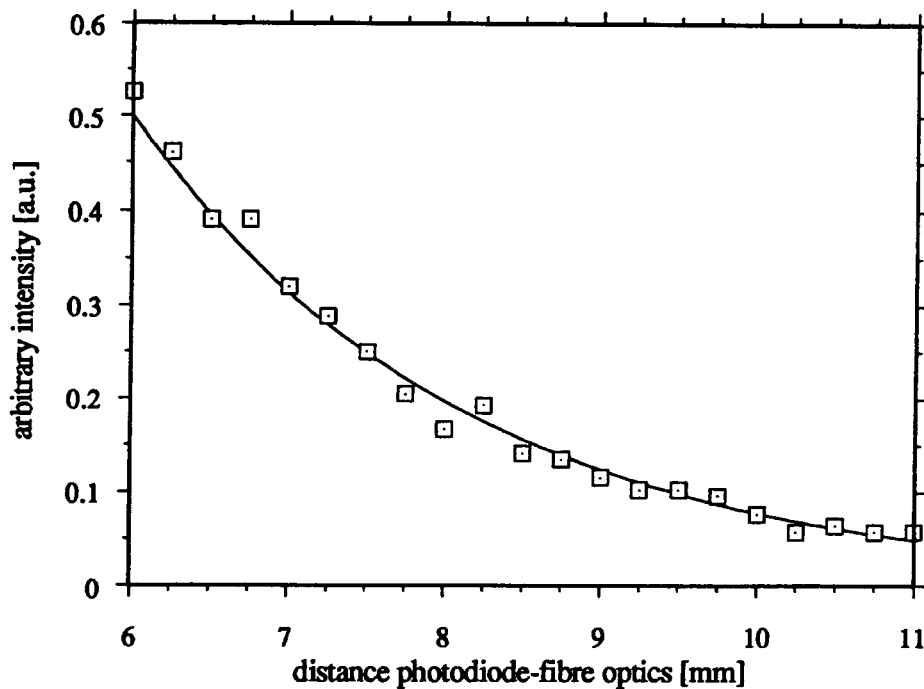


Fig. A.5: plot of the measured backscattered (relative) intensity as a function of the distance between the fibre optics and the detection photodiode (from de Haller and Depeursinge, 1991).

distance between the light input and the detector (Fig. A.5). Then the oximeter was put on the forearm before and after compression of the brachial artery. The compression was released after 70 [s] (Fig. A.6).

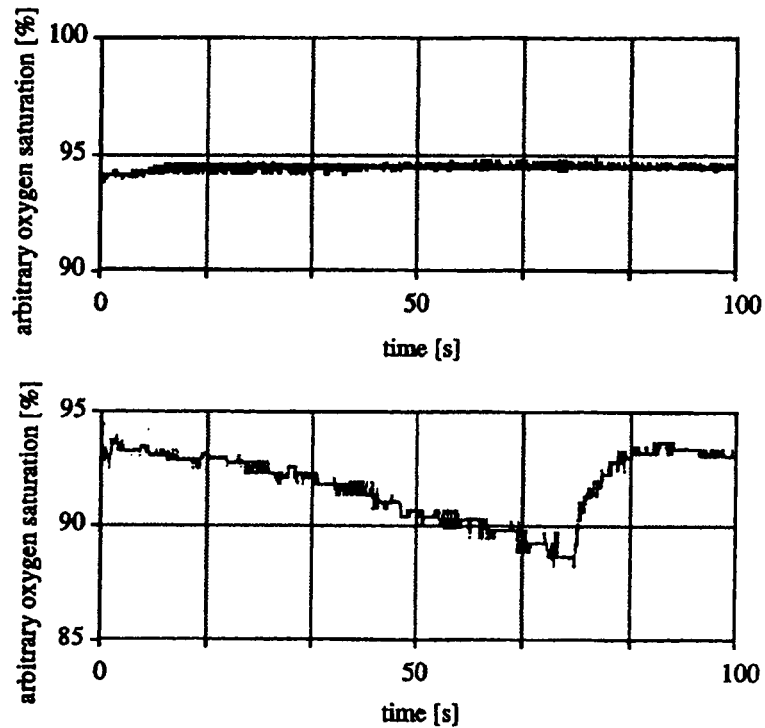


Fig. A.6: plots of the measured oxygen saturation in the human forearm before (top) and during (bottom) brachial artery compression. The compression is released after 75 [s] (from de Haller and Depeursinge, 1991).

### A.3. The two-flux Kubelka-Munk model

The K-M model describes the light transmission through a plane-parallel infinite slab of thickness  $d$  considering the forward and backward transmitted intensity. This model differs from the Beer law because of the consideration of the backscattering. The source is diffuse and its extent is infinite (Fig. A.7). The

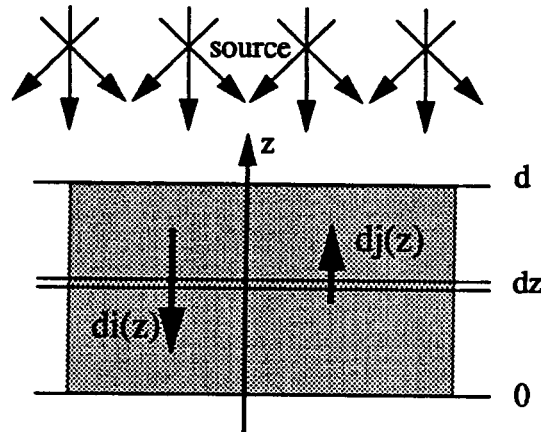


Fig. A.7: K-M model

bottom of the slab is at 0 and the illuminated surface is at  $d$ . The bottom is supposed totally absorbing, i.e.  $j(0) = 0$ . The differential equations describe the intensity  $di$  and  $dj$  forwards and backwards scattered by the element  $dz$  at a thickness  $z$  (Eq. A.3).

$$\begin{aligned} -di &= -(S + K) idz + Sjdz \\ dj &= -(S + K) jdz + Sidz \end{aligned} \quad \text{Eq. A.3}$$

The solution of these equations are:

$$\begin{aligned} i(z) &= i_0 \cdot \frac{a \sinh(Sbz) + b \cosh(Sbz)}{a \sinh(Sbd) + b \cosh(Sbd)} & a &= \frac{S + K}{S} \\ j(z) &= i_0 R_0 \cdot \frac{\sinh(Sbz)}{\sinh(Sbd)} & b &= \sqrt{a^2 - 1} \end{aligned} \quad \text{Eq. A.4}$$

with  $R_0 = \frac{j_0}{i_0}$  as the reflectance of the sample for a absorbing background ( $R(z=0) = 0$ ).

With  $T$  (diffuse transmittance) defined as  $\frac{i(z)}{i_0}$ ,  $R$  (diffuse reflectance) defined as  $\frac{j(z)}{i_0}$  and  $r$  defined as  $\frac{j(z)}{i(z)}$

$$R_{\infty} = \lim_{z \rightarrow \infty} r = a - b \quad \text{Eq. A.5}$$

For biological tissues,  $S$  and  $d$  are large enough to have  $b \cdot S \cdot d \gg 1$  so that with

$$R_{\infty} \cong R_0 + \frac{T^2}{2b} \cong R_0$$

$$a = \frac{1 + R_0^2 - T^2}{2R_0}$$

and

$$b = \sqrt{a^2 - 1}$$

the scattering and absorbing coefficients could be derived (van Gemert et al., 1987):

$$S = \frac{1}{bd} \ln \left( \frac{1 - R(a - b)}{T} \right)$$

$$K = (a - 1) S \quad \text{Eq. A.6}$$

and finally the K-M two-flux model is in relation with the diffusion approximation and the parameters  $\Sigma_s$  and  $\Sigma_a$  could be determined from  $S$  and  $K$ .

$$S = \frac{3}{4} \Sigma_s (1 - g) - \frac{1}{4} \Sigma_a$$

$$K = 2 \Sigma_a \quad \text{Eq. A.7}$$

These relations (Eq. A.7) are important in the determination of the optical properties of biological tissues.  $R_0$  and  $T$  are measurable values and thus  $\Sigma_s$  and  $\Sigma_a$  can be determined.

### A.4. The Boltzmann equation

To get the time independent radiative transport equation known as Boltzmann equation, we should consider the flux of photons (assumed as particles) through a finite volume  $dV$  with the optical properties described by  $\Sigma_a$  and  $\Sigma_s$  and a phase function  $p(\hat{s} \cdot \hat{s}')$ . The conservation of flux implies that the sum of the source in the volume  $dV$ , the photons entering the volume  $dV$  and the photons scattered in  $V$  from direction  $\omega'$  to  $\omega$  is equal to the sum of the photons going out of the volume  $dV$ , the photons absorbed and scattered out of direction  $\omega$  (Fig. A.8). So

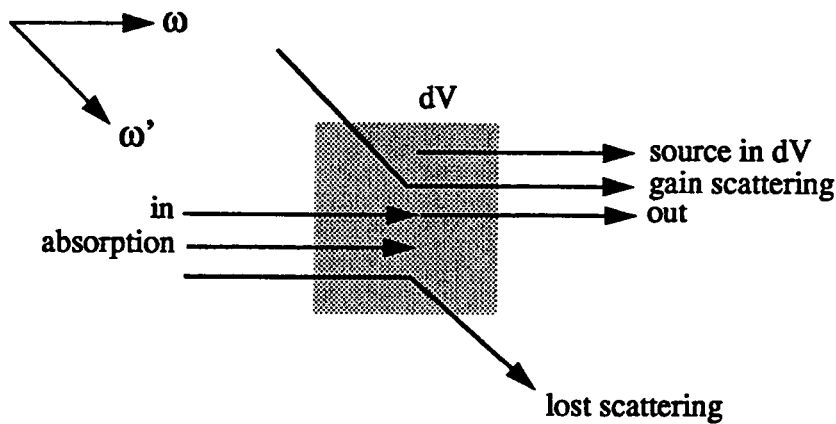


Fig. A.8: flux conservation in the volume  $dV$

the amount of photons in the volume  $dV$  set at  $\hat{r}$  in the direction  $\omega$  in the solid angle  $d\omega$  is  $\sigma(\hat{r}, \hat{s}) dV d\omega$  which is a source term. The amount of photons expressed by the radiance  $L(\hat{r}, \hat{s})$  through a surface  $dS$  is  $L(\hat{r}, \hat{s}) dS$  so that the photon losses minus the photon gain through the entire surface  $S$  of the volume  $V$  is

$$\int_S L(\hat{r}, \hat{s}) \hat{s} dS \quad \text{Eq. A.8}$$

which gives, with the Gauss theorem,

$$\int_V \hat{s} \nabla L(\hat{r}, \hat{s}) dV \quad \text{Eq. A.9}$$

Considering the scattered photons in the volume  $V$  from  $\omega$  to  $\omega'$ , proportional to the phase function and the radiance in the direction  $\omega'$ , it leads with the previous considerations to Eq. A.10 which has the form of the Boltzmann equation.

$$\hat{s} \nabla L(\hat{r}, \hat{s}) = -\Sigma_t L(\hat{r}, \hat{s}) + \int_{4\pi} \Sigma_s p(\hat{s} \cdot \hat{s}') L(\hat{r}, \hat{s}') d\omega' + \sigma(\hat{r}, \hat{s}) \quad \text{Eq. A.10}$$

## A.5. Diffusion approximation

According to the Boltzmann equation

$$\hat{s} \nabla L(\hat{r}, \hat{s}) = -\Sigma_t L(\hat{r}, \hat{s}) + \int_{4\pi} \Sigma_s p(\hat{s} \cdot \hat{s}') L(\hat{r}, \hat{s}') d\omega' + \sigma(\hat{r}, \hat{s}) \quad \text{Eq. A.11}$$

the left term could be expressed by

$$\hat{s} \nabla L(\hat{r}, \hat{s}) = \text{div}(L(\hat{r}, \hat{s}) \cdot \hat{s}) \quad \text{Eq. A.12}$$

Assuming that fluorescence is negligible, the source term  $\sigma(\mathbf{r}, \mathbf{s}) = 0$  and integrating over the full space (i.e.  $4\pi$ ) one gets

$$\text{div} \vec{F}(\hat{r}) = -\Sigma_a \int_{4\pi} L(\hat{r}, \hat{s}) d\omega \quad \text{Eq. A.13}$$

which verify the conservation of the flux ( $\Sigma_a = 0 \text{ div} \Rightarrow \vec{F}(\hat{r}) = 0$ ).

It is useful to separate the flux into two components  $L_d(\hat{r}, \hat{s})$  as the scattered flux of photons and  $L_{ir}(\hat{r}, \hat{s})$  as the reduced flux of photons or flux of photons which were not scattered ( $L_{ir}(\hat{r}, \hat{s}) \ll L_d(\hat{r}, \hat{s})$ ):

$$\begin{aligned} L(\hat{r}, \hat{s}) &= L_d(\hat{r}, \hat{s}) + L_{ir}(\hat{r}, \hat{s}) \\ \frac{dL_{ir}(\hat{r}, \hat{s})}{d\omega} &= -(\Sigma_t \cdot L_{ir}(\hat{r}, \hat{s})) \end{aligned} \quad \text{Eq. A.14}$$

so that the Boltzmann equation is

$$\frac{dL_d(\hat{r}, \hat{s})}{d\omega} = -\Sigma_t \cdot L_d(\hat{r}, \hat{s}) + \Sigma_s \int_{4\pi} p(\hat{s} \cdot \hat{s}') L_d(\hat{r}, \hat{s}') d\omega' + \epsilon_{ir}(\hat{r}, \hat{s}) \quad \text{Eq. A.15}$$

$$\text{where: } \epsilon_{ir}(\hat{r}, \hat{s}) = \int_{4\pi} p(\hat{s} \cdot \hat{s}') L_{ir}(\hat{r}, \hat{s}') d\omega'$$

The boundary conditions implies that the scattered flux  $L_d(\hat{r}, \hat{s}) = 0$  on the boundary, meaning that scattering occurs only within the medium.

The diffusion approximation implies that the scattered flux is only composed of the photon density and the photon current at this very location, i.e. the scattered flux has undergone multiple scattering:

$$L_d(\hat{r}, \hat{s}) = U_d(\hat{r}) + \frac{3}{4\pi} \cdot \vec{F}_d(\hat{r}) \cdot \hat{s} \quad \text{Eq. A.16}$$

with:

$$\begin{aligned}\vec{F}_d(\hat{r}) &= \int_{4\pi} L_d(\hat{r}, \hat{s}) \hat{s} d\omega \\ U_d(\hat{r}) &= \frac{1}{4\pi} \int_{4\pi} L_d(\hat{r}, \hat{s}) d\omega \\ U_{ir}(\hat{r}) &= \frac{1}{4\pi} \int_{4\pi} L_{ir}(\hat{r}, \hat{s}) d\omega\end{aligned}$$

Eq. A.17

Integrating over the whole solid angle and using Eq. A.16 in Eq. A.15 the transfer equation takes the form of:

$$\nabla U_d(\hat{r}) = -\frac{3}{4\pi} \vec{F}_d \hat{r} [\Sigma_t - \Sigma_s \bar{u}] + \frac{3}{4\pi} \int_{4\pi} \epsilon_{ir}(\hat{r}, \hat{s}') d\omega' \quad \text{Eq. A.18}$$

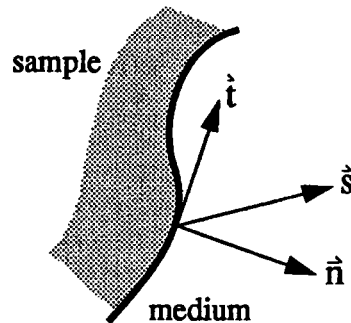
where  $\bar{u}$  is  $\int_{4\pi} p(\hat{s}, \hat{s}') (\hat{s} \cdot \hat{s}') d\omega'$  and  $\Sigma_{tr} = \Sigma_t - \Sigma_s \bar{u}$  the transport cross section.

Finally with Eq. A.18 in Eq. A.13:

$$\nabla^2 U_d(\hat{r}) - 3\Sigma_a \Sigma_{tr} U_d(\hat{r}) = -3\Sigma_a \Sigma_{tr} U_{ir}(\hat{r}) + \frac{3}{4\pi} \nabla \int_{4\pi} \epsilon_{ir}(\hat{r}, \hat{s}') d\omega' \quad \text{Eq. A.19}$$

### Boundary Conditions:

The exact boundary conditions are determined by  $L_d(\hat{r}, \hat{s})=0$  with  $\hat{s}$  outward directed on the surface of the sample. In the diffusion approximation, the boundary conditions are expressed by  $\int_{2\pi} L_d(\hat{r}_s, \hat{s}) (\hat{s} \cdot \hat{n}) d\omega = 0$  with  $(\hat{s} \cdot \hat{n}) > 0$ .



These boundary conditions could be expressed as a function of  $U_d(\hat{r})$  only

$$\vec{F}_d(\hat{r}) = F_{dn}(\hat{r}_s) \hat{n} + F_{dt}(\hat{r}_s) \hat{t} \quad \text{Eq. A.20}$$



by substitution of Eq. A.20 in Eq. A.16 then in the boundary equation expressed above and then integrating, it follows

$$\frac{1}{2}U_d(\hat{r}_s) + \frac{1}{4\pi} \cdot F_{dn}(\hat{r}_s) = 0 \quad \text{Eq. A.21}$$

and with Eq. A.18

$$F_{dn}(\hat{r}) = \hat{n}\vec{F}_d(\hat{r}) = -\frac{4\pi}{3}\hat{n}\nabla U_d(\hat{r}) + \hat{n}\frac{1}{\Sigma_{tr}}\int \epsilon_{ir}(\hat{r})\hat{s}d\omega \quad \text{Eq. A.22}$$

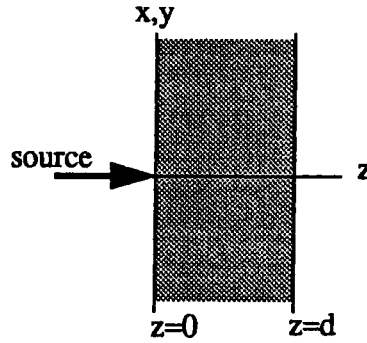
so the boundary conditions are formulated with

$$U_d(\hat{r}) = -\frac{2}{3\Sigma_{tr}}\frac{\partial}{\partial n}U(\hat{r}) + 2\hat{n}\frac{1}{\Sigma_{tr}}\frac{1}{4\pi}\int \epsilon_{ir}(\hat{r})\hat{s}d\omega = 0 \quad \text{Eq. A.23}$$

The last term express the anisotropy of the scattering, so if the scattering is isotropic,  $p(\hat{s} \cdot \hat{s}')$  is a constant and the last term is equal to 0.

### Collimated Beam:

In the case of a narrow collimated beam (i.e. a laser source) incident on a plane parallel slab containing absorbing and scattering particles homogeneously



distributed, the source is described by  $L_{ir}(\hat{r}, \hat{s})=L_0\delta(\omega-\omega_0)$ , the reduced intensity is then within the slab

$$L_{ir}(\hat{r}, \hat{s}) = L_0 \cdot e^{-\Sigma_t z} \delta(\omega - \omega') \quad \text{Eq. A.24}$$

In reference to Eq. A.19

$$U_{ir}(\hat{r}) = \frac{L_0}{4\pi} \cdot e^{-\Sigma_t z} \quad \epsilon_{ir}(\hat{r}) = \Sigma_s p(\hat{s} \cdot \hat{s}') L_0 e^{-\Sigma_t z} \quad \text{Eq. A.25}$$

so that

$$\nabla^2 U_d(\hat{r}) - 3\Sigma_a \Sigma_{tr} U_d(\hat{r}) = -\frac{3}{4\pi} (\Sigma_s \Sigma_{tr} + \Sigma_s \Sigma_t g) L_0 e^{-\Sigma_t z} \quad \text{Eq. A.26}$$

The boundary conditions are then according to Eq. A.23

$$U_d(\hat{r}) - \frac{2}{3} \Sigma_{tr} \frac{\partial}{\partial z} U_d(\hat{r}) + \frac{\hat{z}}{2\pi} \cdot \frac{1}{\Sigma_{tr}} \int \epsilon_{ir}(\hat{r}) \hat{s} d\omega = 0 \quad (z = 0)$$

$$U_d(\hat{r}) + \frac{2}{3} \Sigma_{tr} \frac{\partial}{\partial z} U_d(\hat{r}) - \frac{\hat{z}}{2\pi} \cdot \frac{1}{\Sigma_{tr}} \int \epsilon_{ir}(\hat{r}) \hat{s} d\omega = 0 \quad (z = d) \quad \text{Eq. A.27}$$

To solve Eq. A.26 with the boundary conditions expressed above, a Green function  $G(\hat{r}, \hat{r}')$  has to satisfy

$$\nabla^2 G(\hat{r}, \hat{r}') - 3\Sigma_a \Sigma_{tr} \cdot G(\hat{r}, \hat{r}') = -\delta(\hat{r}, \hat{r}')$$

$$G(\hat{r}, \hat{r}') - \frac{2}{3} \Sigma_{tr} \frac{\partial}{\partial z} G(\hat{r}, \hat{r}') = 0 \quad (z = 0)$$

$$G(\hat{r}, \hat{r}') + \frac{2}{3} \Sigma_{tr} \frac{\partial}{\partial z} G(\hat{r}, \hat{r}') = 0 \quad (z = d)$$

Eq. A.28

with the Green identity,  $U_d$  is expressed by  $G$

$$U_d(\hat{r}) = \int_V G(\hat{r}, \hat{r}') \left( \frac{3}{4\pi} (\Sigma_s \Sigma_{tr} + \Sigma_s \Sigma_t g) L_0 e^{-\Sigma_t z} \right) dV + \frac{3}{4\pi \Sigma_{tr} S} \int G(\hat{r}, \hat{r}') dS$$

Eq. A.29

In the case of a symmetrical collimated source in the direction  $\hat{z}$ , the Green function  $G(\hat{r}, \hat{r}')$  is

$$G(\hat{r}, \hat{r}') = \sum_{n=1}^{\infty} \frac{Z_n(z) Z_n(z')}{2\pi N_n^2} K_0(\lambda_n \sqrt{x^2 + y^2}) I_0(\lambda_n \sqrt{x'^2 + y'^2}) \quad \text{Eq. A.30}$$

where  $K_0$  and  $I_0$  are the modified Bessel function,  $Z_n$  an eigen-function satisfying the boundary conditions and  $N_n$  a normalisation factor

$$N_n^2 = \int_0^d [Z_n(z)]^2 dz$$

The coefficients are defined as follows:

$$Z_n(z) = \sin(k_n z + \gamma_n)$$

$$\gamma_n = \text{atan} \left( \frac{2}{3} \Sigma_{tr} \cdot k_n \right)$$

$$\tan(k_n d) = \frac{2 \frac{2}{3} \Sigma_{tr} k_n}{\left[ \left( \frac{2}{3} \Sigma_{tr} \cdot k_n \right)^2 - 1 \right]}$$

$$\lambda_n^2 = k_n^2 + \kappa_d^2$$

where  $\kappa_d$  is an attenuation constant.

So by substitution in Eq. A.29 and  $r = \sqrt{x^2 + y^2}$

$$U_d(\hat{r}) = 2\pi \int_0^\infty r' dr' \int_0^d G(r, z, r', z') \left( \frac{3}{4\pi} (\Sigma_s \Sigma_{tr} + \Sigma_s \Sigma_t g) L_0 e^{-\Sigma_t z} \right) dz +$$

$$+ \frac{3}{2\Sigma_{tr}} \int_0^\infty G(r, z, r', 0) \left[ \frac{1}{\Sigma_{tr}} \int \epsilon_{ir}(r', 0) s d\omega \right] r' dr'$$

Eq. A.31

### A.6. The diffuse intensity

With the diffusion approximation and smooth boundaries for medium and object, one could determine the diffuse transmitted intensity through a plan-parallel semi-infinite slab of thickness  $z_{\max}$  containing a spherical object of radius  $r_0$  located at  $z_0$  (Fig. A.9). An extended source  $S(x,y)$ , plane wave, is set at the

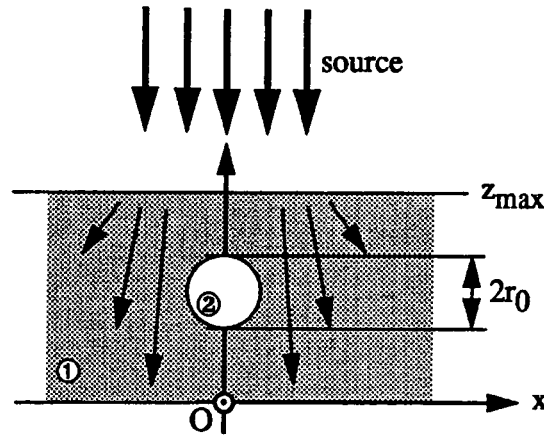


Fig. A.9: lateral view of the sample enclosed in the sample. The sample is characterized by a scattering coefficient  $D_1$  and the object by  $D_2$ .

thickness  $z$  and the confined sphere is centred on  $x$ -axis. The stationary diffusion equation for the sample is then the well known Laplace equation:

$$\nabla^2 I(\vec{r}) = 0 \quad \text{Eq. A.32}$$

with the boundary conditions:

$$I(x, y, z_{\max}) = S(x, y) \quad I(x, y, 0) = 0 \quad \text{Eq. A.33}$$

$I(\vec{r})$  being the incident diffuse intensity.

The diffusion equation inside the absorbing object is:

$$\nabla^2 I(\vec{r}) = \kappa^2 I(\vec{r}) \quad \text{Eq. A.34}$$

To get the transmitted light, one should solve Eq. A.32 and Eq. A.34 with the boundary conditions Eq. A.33. The solving of these equations necessitate further boundary conditions on the surface of the object to conserve the continuity and the flux.

$$I_{\text{OUT}} = I_{\text{IN}} \quad \text{Eq. A.35}$$

$$D_1 \frac{\partial I_{\text{OUT}}}{\partial n} = D_2 \frac{\partial I_{\text{IN}}}{\partial n} \quad \text{Eq. A.36}$$

where  $\frac{\partial}{\partial n}$  is the normal derivative on the surface of the object. If the object absorbs only on its surface,  $\alpha I_{IN}$  is added to the left term of Eq. A.36 and Eq. A.32 would describe scattering in the object.  $\alpha$  describes absorption.

Since Eq. A.32 is the Laplace equation it is practical to use the formalism of electrodynamics and introduce the concepts of charges, dipoles and mirror images, in order to get a solution. Assuming a potential for a point charge with a plane wave  $S(x,y,z)=I_0$  incident on the slab and a spherical object set at  $\vec{z}_0=(0,0,z_0)$ , this results in a summation over mirror images, the outcome being the propagator for the medium, and the potential for a dipole is obtained. The solution of Eq. A.32 describing light in the slab is for the three first terms:

$$I(\vec{r}) = I_0 \frac{z}{z_{\max}} + a \sum_{-\infty}^{\infty} \left\{ \frac{1}{|\vec{r} - \vec{z}_0 + 2z_{\max} i \vec{z}|} - \frac{1}{|\vec{r} + \vec{z}_0 + 2z_{\max} i \vec{z}|} \right\} +$$

$$+ s \sum_{-\infty}^{\infty} \left\{ \frac{z - z_0 + 2iz_{\max}}{\left( (z - z_0 + 2iz_{\max})^2 + |\vec{r}|^2 \right)^{\frac{3}{2}}} - \frac{z + z_0 + 2iz_{\max}}{\left( (z + z_0 + 2iz_{\max})^2 + |\vec{r}|^2 \right)^{\frac{3}{2}}} \right\} \quad \text{Eq. A.37}$$

where  $\vec{z}$  is the unit vector in the z-axis. The first term describes the unscattered intensity (which is near to 0 for tissue scattering conditions), the second term describes the absorption and the third term the scattering. Higher terms of the solution would describe the disturbance of the object in the far field, but the contribution is smaller enough to ignore these terms when the object size is much smaller than the slab thickness.

For a uniform absorbing object (Eq. A.34), the light inside the object is given by the two spherical Bessel functions:

$$I_{IN}(\vec{r}) = A \frac{\sinh \kappa |r|}{\kappa |r|} - \frac{3B}{\kappa} \left( \frac{\sinh \kappa |r|}{\kappa^2 |r|^2} - \frac{\cosh \kappa |r|}{\kappa |r|} \right) J_{10}(\theta, \varphi) \quad \text{Eq. A.38}$$

When the object absorbs on its boundary, Eq. A.38 takes the form of:

$$I_{IN}(\vec{r}) = A + B(z - z_0) \quad \text{Eq. A.39}$$

The value of A is:

$$A = \frac{D_1 s}{\alpha r_0^2 \frac{\sinh \kappa r_0}{\kappa r_0} + r_0 D_2 \left( \cosh \kappa r_0 - \frac{\sinh \kappa r_0}{\kappa r_0} \right)} \quad \text{Eq. A.40}$$

of B:

$$B = \frac{1}{3} \frac{\kappa^2 r_0^2}{\frac{\sinh \kappa r_0}{\kappa r_0} - \cosh \kappa r_0} \left( \frac{I_0}{z_{\max}} + \frac{s}{r_0^3} \right) \quad \text{Eq. A.41}$$

of a:

$$a = -I_0 \frac{r_0 z_0}{z_{\max}} \frac{D_2 \left( \cosh \kappa r_0 - \frac{\sinh \kappa r_0}{\kappa r_0} \right) / \frac{\sinh \kappa r_0}{\kappa r_0} + \alpha r_0}{D_1 + D_2 \left( \cosh \kappa r_0 - \frac{\sinh \kappa r_0}{\kappa r_0} \right) / \frac{\sinh \kappa r_0}{\kappa r_0} + \alpha r_0} \quad \text{Eq. A.42}$$

and of s:

$$s = I_0 \frac{r_0^3}{z_0} \frac{D_1 - D_2 \frac{2 \cosh \kappa r_0 - \frac{2 \sinh \kappa r_0}{\kappa r_0} - \kappa r_0 \sinh \kappa r_0}{\frac{\sinh \kappa r_0}{\kappa r_0} - \cosh \kappa r_0} - \alpha r_0}{2D_1 + D_2 \frac{2 \cosh \kappa r_0 - \frac{2 \sinh \kappa r_0}{\kappa r_0} - \kappa r_0 \sinh \kappa r_0}{\frac{\sinh \kappa r_0}{\kappa r_0} - \cosh \kappa r_0} + \alpha r_0} \quad \text{Eq. A.43}$$

When  $\kappa \ll D_i$ , the values for A, B, a and s are reduced to:

$$A = \frac{D_1 a}{\alpha r_0^2}$$

$$B = \frac{I_0}{z_{\max}} + \frac{s}{r_0^3}$$

$$a = -\frac{z_0 r_0}{z_{\max}} \frac{\alpha r_0}{D_1 + \alpha r_0}$$

$$s = \frac{r_0^3}{z_{\max}} \frac{D_1 - D_2 - \alpha r_0}{2D_1 + D_2 + \alpha r_0}$$

Eq. A.44

Within the diffusion approximation and  $\kappa \ll D_i$ , the transmitted light will be defined at  $z=1$  mfp.

## A.7. Free pathlength

In the Beer Lambert approximation, the transmitted intensity follows  $\frac{d}{dz}I(z) = -\Sigma_t \cdot I(z)$  so that the intensity of the unscattered photons could be expressed by  $I(z) = I(0) e^{-\Sigma_t z}$

On the other hand, one could define:

$$P_1(\hat{r}) = \frac{\Phi'(\hat{r})}{\Phi(\hat{r})} = \Sigma_t \quad \text{Eq. A.45}$$

as the probability of a photon to be absorbed or scattered in  $\hat{r}$  and

$$P_2(\hat{r}) = \frac{\Phi(\hat{r})}{\Phi(0)} = e^{-\Sigma_t \hat{r}} \quad \text{Eq. A.46}$$

as the probability to reach  $\hat{r}$  without collisions. These two events being independent, the probability density of a collision in  $\hat{r}$  is

$$P(\hat{r}) = P_1(\hat{r}) \cdot P_2(\hat{r}) = \Sigma_t e^{-\Sigma_t \hat{r}} \quad \text{Eq. A.47}$$

assuming  $L = |\mathbf{r}|$  the partition function is

$$\overline{P(L)} = \int_0^L P(x) dx = 1 - e^{-\Sigma_t L} \quad \text{Eq. A.48}$$

$\overline{P(x)}$  is then the probability to have a free pathlength between  $]0...x]$ . The free pathlength is then expressed through:

$$\boxed{L = -\frac{\ln(1 - \overline{P(L)})}{\Sigma_t}} \quad \text{Eq. A.49}$$

where  $0 \leq \overline{P(L)} < 1$ . The mean free path is then given by

$$\bar{L} = \int_0^{\infty} P(x) x dx = \frac{1}{\Sigma_t} \quad \text{Eq. A.50}$$

On the basis of the Eq. A.49, the free pathlength is easily determined in the Monte-Carlo simulation by drawing a random number  $\alpha_i$ ,  $0 < \alpha_i \leq 1$ , and solving the following equation:

$$L = -\frac{\ln(\alpha_i)}{\Sigma_t} \quad \text{Eq. A.51}$$

### A.8. Image parameters and Image Quality Index

An image is generally characterised by its contrast, its resolution and its noisy background. The contrast renders the difference in light transmission, the resolution determines the capability of the system to show tiny details and the noise is the statistical variation of the transmission of light.

- The *contrast*  $C$  is the difference of transmission of an object and its surrounding medium. The optical density OD is expressed through  $OD = -\log(I/I_0)$  where  $I$  is the total transmitted intensity and  $I_0$  the total incident intensity. The temporal optical density  $OD_t$  is given as  $OD_t = -\log(I_t/I_0)$ , where  $I_t$  is the total transmitted intensity up to time  $t$  and  $I_0$  the total incident intensity. It depends on the system and the integration time. We used the contrast  $C$  defined as the difference of transmission per length unit.

$$C = \frac{|\Delta OD|}{\Delta z} \quad \text{Eq. A.52}$$

- The *resolution* could be described by the MTF which is the system response to a one-dimensional point source or LSF. The MTF is the modulus of the spatial spectrum of the LSF.

$$MTF(f_x) = |\mathcal{F}(LSF(x))| \quad \text{Eq. A.53}$$

The  $MTF(f_x, f_y)$  is usually normalised to 1 at frequency zero. In the practice, the  $LSF(x)$  is derived from the  $PSF(x, y)$  which is the system response to a one-dimensional point source.

$$LSF(x) = \int PSF(x, y) dy \quad \text{Eq. A.54}$$

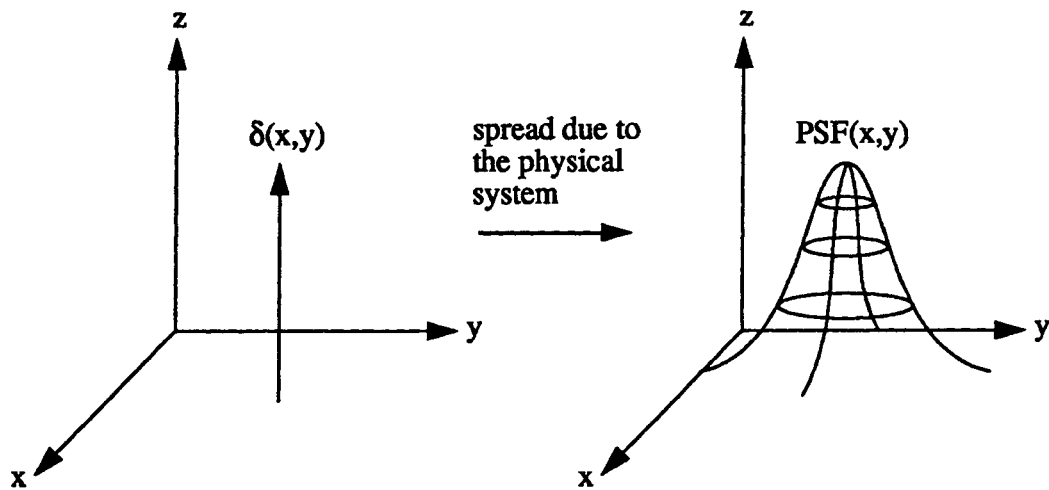
$$\begin{aligned} MTF(f_x, 0) &= |\mathcal{F}(PSF)|_{f_y=0} = |\mathcal{F}(\int PSF(x, y) dy)| = \\ &= |\mathcal{F}(LSF(x))| = MTF(f_x) \end{aligned} \quad \text{Eq. A.55}$$

then

$$MTF(f_x, f_y) = |\mathcal{F}(PSF(x, y))| \quad \text{Eq. A.56}$$



The physical system, generally composed of the source, the medium and the detector, spread out the dirac function, and thus the system is limited in the rendering of too small details.



The optimal situation is a system rendering a dirac by a dirac, the MTF being the constant function  $MTF(f) = 1$  over the whole spatial frequency range. In reality, the MTF is a continuously decreasing function and thus gives the resolution of an imaging system.

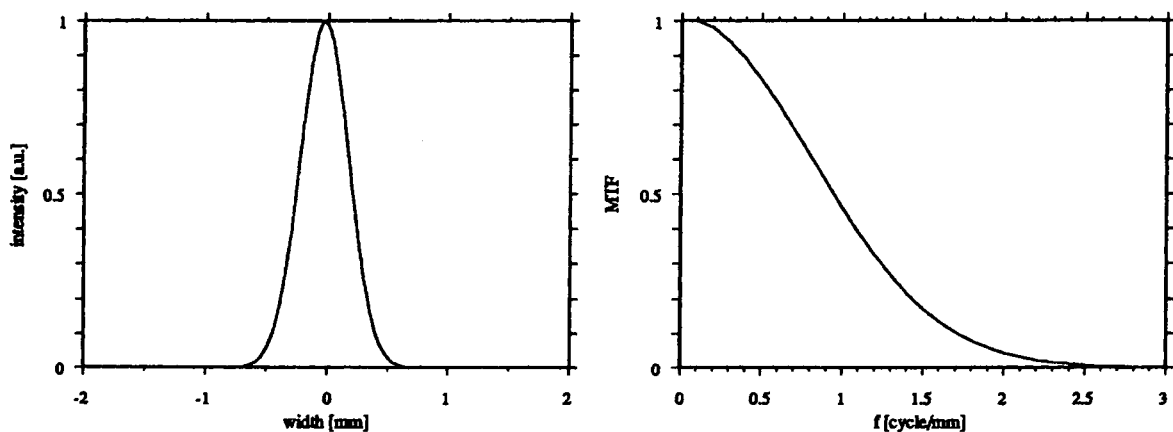


Fig. A.10: example of a typical gaussian PSF and its corresponding MTF which exhibits also a gaussian shape.

- The *noise* is expressed through the Wiener spectrum (Dainty and Shaw, 1974):

$$W(f_x, f_y) = \lim_{L_x, L_y \rightarrow \infty} \frac{1}{4L_x L_y} \left| \mathcal{F} \left( \int_{-L_x}^{L_x} dx \int_{-L_y}^{L_y} dy \Delta OD(x, y) \right) \right|^2 \quad \text{Eq. A.57}$$

For an uniformly exposed surface  $4L_x L_y$ . The Wiener spectrum could also be

defined as the Fourier transform of the autocorrelation function of the variation of the OD. In the simulation, the Wiener spectrum was derived from the noise obtained by illuminating the entire detector from an expanded source of radius 25 mm through adipose tissue. Quantum noise and simulated speckle and anatomical noise were added. With the hypothesis of a gaussian MTF(f) and a white noise, the Wiener spectrum could be expressed through the variance  $\sigma_A^2$  of the noise for an aperture A, or illuminated area A (corresponding to the previous  $4L_xL_y$ ).

$$W(f) = A \cdot \sigma_A^2 \quad \text{Eq. A.58}$$

## A.9. Program

The program has been compiled in Pascal language during the first part of the thesis to work on an Apollo DN 3500 station, and then for practical necessity and

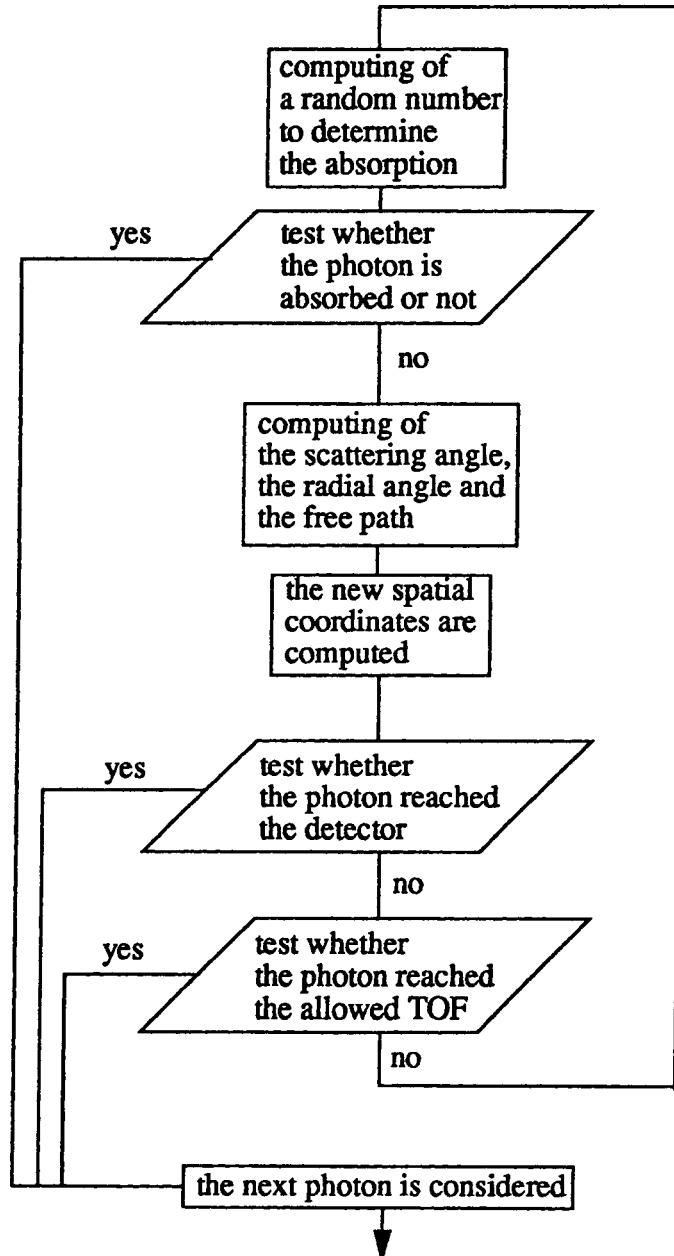


Fig. A.11:organigram of the single photon history. The detector position, the TOF and the absorption condition are input values of the program

speed gain, it was compiled in C language in order to work on different machines such as the HP series 700, Apollo DN 5500 or Cray-2 computers without compiler troubleshooting. Cray-2 computing necessitated a drastic change in

architecture of the program, thus only the workstations were used for Monte Carlo computing after preliminary tests with C language.

The random generator function `rand()` uses a multiplicative congruential random-number generator with a period of  $2^{32}$  that returns successive pseudo-random numbers from 0 to  $2^{15}-1$ . The first seed is arbitrarily determined between 0 and 1. The mean value of `rand()/215-1` as well as the variance over  $10^5$  tests are given in Table 4.

seed	$\overline{\text{random}}$	variance
0.0	0.500034	0.083326
0.1	0.498703	0.083525
0.2	0.500702	0.083705
0.3	0.500431	0.083625
0.4	0.499322	0.083304
0.5	0.501495	0.083763
0.6	0.499520	0.083262
0.7	0.498285	0.083290
0.8	0.502411	0.082875
0.9	0.499986	0.083078
1	0.500014	0.082933
ideal	0.50000	0.083333

Table 4: generation of pseudo-random numbers

The two main functions in the Monte Carlo simulation of light transport are the function computing the scattering angle for a given phase function and the function computing the new spatial coordinates of the photon after each interaction.

Following part of the program is the function giving the scattering angle `angle` according to the H-G phase function and the radial angle `phi`. This function was tested over  $10^5$  loops and the mean value of the computed `g` as well as the variance are shown in Table 5.

```
double scattering_angle(double g)
{
double w,dir,angle,phi,a,b,signe;
```

```

dir=rand();
if (dir<=0.5) signe=1;
else signe=-1;
w=rand();
a=(1+g)/(2*g);
b=(1-g*g)/(2*g);
angle=signe*acos((1+g*g-(b/(a-w))*(b/(a-w)))/(2*g));
phi=rand48*2*pi;
}

```

g	$\bar{g}$	variance
0.99	0.990095	0.006479
0.95	0.949747	0.032484
0.90	0.899409	0.063550
0.85	0.849239	0.092780
0.80	0.798928	0.120655
0.75	0.746674	0.146674
0.55	0.548639	0.233818

Table 5: convergence of the mean cosine

The convergence of the computed  $g$ 's is good, however, for a small value of  $g$ , the convergence is weaker than for values of  $g$  near to 1.

The following function gives the new spatial coordinates of the photon according to the relations described by Kalos and Whitlock (1986):

```

lieu(double position[3])
{
double denominator,test_cdz,cdnew[3],cd[3];

denominator=sqrt(1-(cd[2]*cd[2]));
cdnew[2]=sin(angle)*denominator*cos(phi)+cd[2]*cos(angle);
cdnew[1]=(sin(angle)/denominator)*(-cd[0]*sin(phi)-cd[2]*cd[1]*-
cos(phi))+cd[1]*cos(angle);
cdnew[0]=(sin(angle)/denominator)*(cd[1]*sin(phi)-cd[2]*cd[0]*-
cos(phi))+cd[0]*cos(angle);
cd[0]=cdnew[0];
cd[1]=cdnew[1];
cd[2]=cdnew[2];
position[2]=position[2]+l*cd[2];
position[1]=position[1]+l*cd[1];
position[0]=position[0]+l*cd[0];
test_cdz=fabs(cd[2]-1);
}

```

```
if (test_cdz<0.000001) cd[2]=0.999999;  
}
```

### A.10. Formaldehyde, hematoxylin and eosin

**Formaldehyde** or  $\text{HCHO}$   $\text{CH}_2\text{O}$  is widely used in medicine for the fixation and conservation of large samples of biological tissues. Small amount of cells could be fixed with red carmin. Formaldehyde is optically transparent to visible light, slightly absorbent in the blue region (Fig. A.12). Formaldehyde has not only the

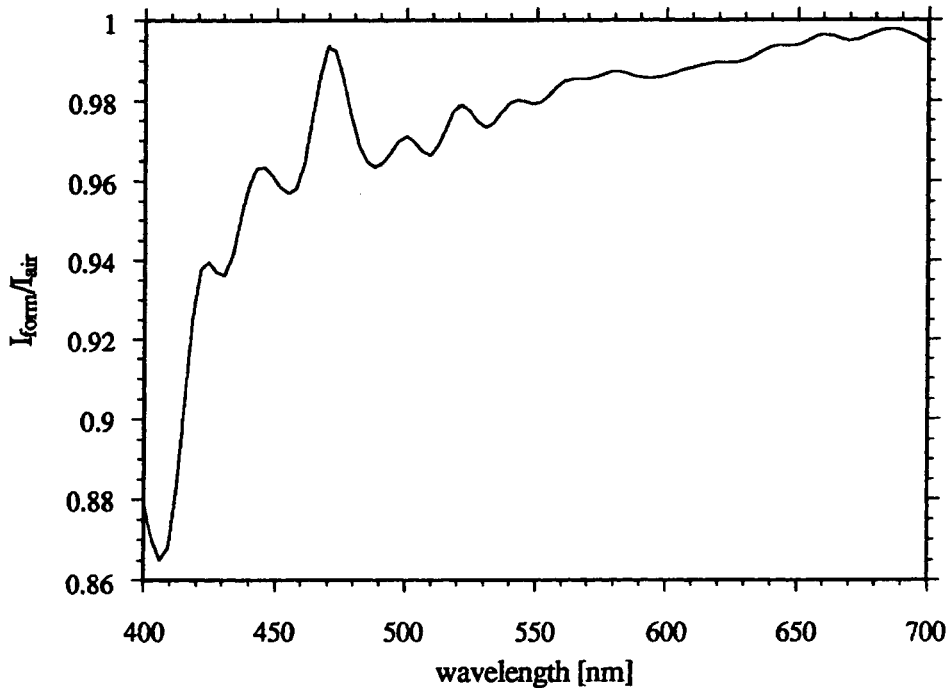


Fig. A.12:transmission spectrum of the formaldehyde 4% vol.

advantage to fix and conserve living tissues, but it is known as an efficient disinfectant which destroys HIV, B-hepatitis or other highly infectious viruses. The sample will be then sterilised and free of any contamination danger. Wearing protecting gloves is however necessary to protect the skin against the high fixative property of formaldehyde.

The principle of formaldehyde is its small molecule size which enable an easy penetration in the cells through the cytoplasmic membrane and obviously its better affinity, so that water is inexorably expelled and totally replaced by the formaldehyde solution.

The samples we received from the Institute of Pathology were conserved in a solution of formaldehyde 4% vol. which is enough to guarantee a good prophylaxis.

**Hematoxylin** (or hemalin),  $C_{16}H_{14}O_6$  aq., is a standard histological dye which has a great affinity to acids and will give a blue colour to the nucleus acids in a cell.

**Eosin** is also an histological dye and has an affinity to bases and gives a red colour to cells.



### A.11. Modulator test data sheet

Factory setting (Quantum Technology, Inc.)

Model: TWAM-11-1-26-2000-530/850	Serial No: E91-565R-1
Test wavelength: 514 [nm]	Crystal type: LiTaO <sub>3</sub>
Halfwave voltage: 82 [VDC] @ 514 [nm]	Crystal size: 1×1×13 [mm <sup>3</sup> ]
Extinction ratio: >31:1	Crystal quantity: 2
Aperture: 1 [mm]	Fluid type: none
Transmission:AR: > 76% AR 530-850 [nm]	Connector: SMA
VSWR: 1.1:1 @ 2000 [MHz]	50 [Ω]
Max DC Voltage: 600 [VDC]	Response: 1.95-2.1 [GHz]

The modulator is DC coupled and is resonantly tuned. This is a resonant device which is tuned for 2 [GHz] operation with approximate Q of 10:1. The single RF SMA connector is for the RF input. None is provided for the RF output.

Material	LiTaO <sub>3</sub>	Units
n <sub>0</sub>	2.176	
n <sub>e</sub>	2.180	
r <sub>41</sub> or r <sub>33</sub> E/O constant	30.5	10 <sup>-12</sup> m/V
Phase sensitivity	1.7	mrاد/V × L/b

Table 6: list of some useful parameters for LiTaO<sub>3</sub>.

The modulator has been tested with a CW (continuous wave) He:Ne laser at 632.8 [nm]. The modulator was driven by a wave generator at 2 [GHz], the signal being amplified by a 10 [W] power amplifier. The driver output amplitude has been set at 750 [mV] and 1.5 [V] (Fig. A.13).

Test wavelength: 632.8 [nm]

Halfwave voltage: 105 [VDC] @ 632.8 [nm]

Extinction ratio: >25:1

VSWR: 1.3:1 @ 2000 [MHz]

50 [Ω]

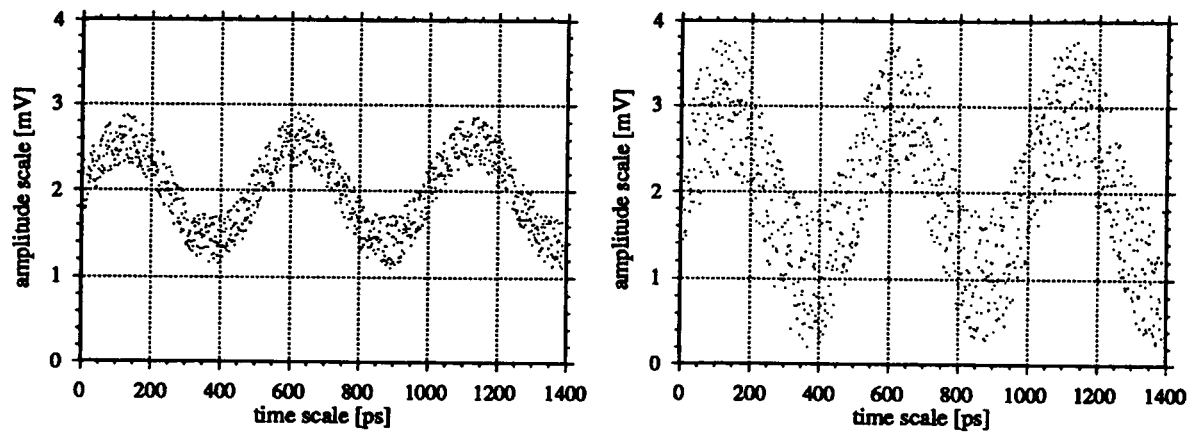


Fig. A.13: plot of the modulation signal of a CW He:Ne laser for 750 [mV] (left) and 1.5 [V] (right) driving amplitude.

## A.12. CCD imager

The Tektronix TK512 imager is a silicon charge-coupled device designed to efficiently image scenes at low light level in the NIR. The CCD is 512×512 pixels 13.8×13.8 [mm] full frame with 27×27 [μm] pixel size. Typical quantum efficiency is plotted in Fig. A.14, the dark current (20 [°C] equivalent) is around 1.0 [nA/cm<sup>2</sup>] (Fig. A.15), the read-out noise is around 8 electrons with a maximum at 10 electrons, the full well signal is at 4×10<sup>5</sup> electrons and the dynamic range (relative to the read-out noise) is 40000:1.

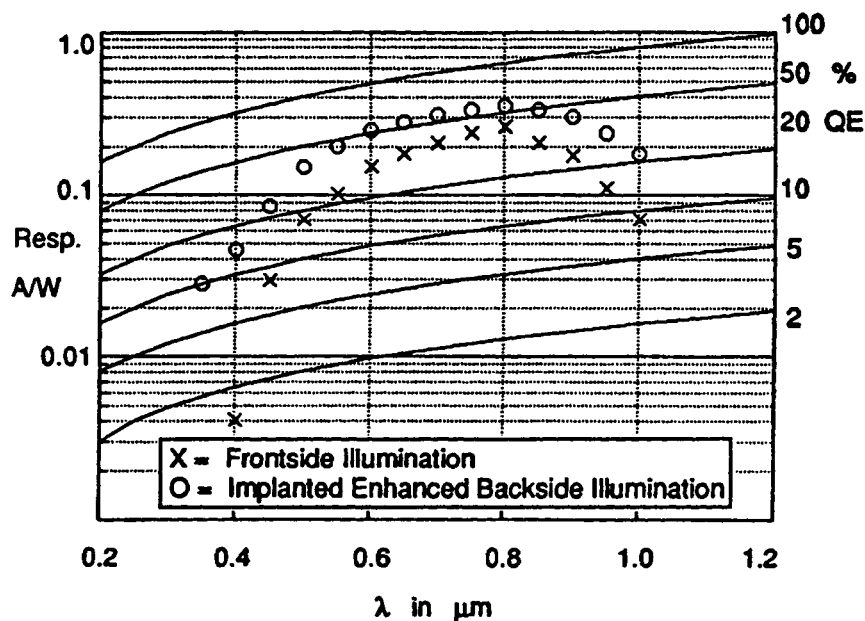


Fig. A.14: quantum efficiency of the CCD imager frontside illuminated (cross) and backside illuminated (circle).

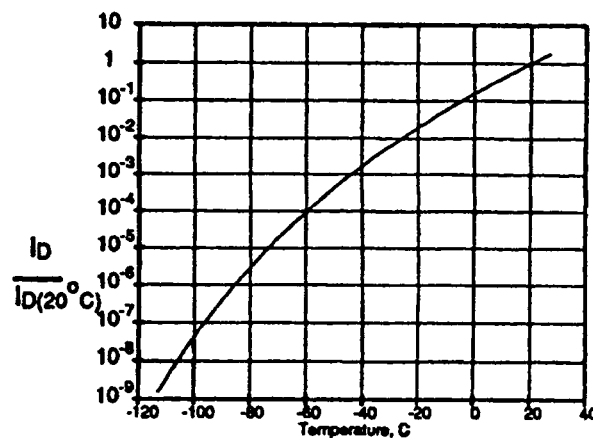


Fig. A.15: dark current variation as a function of the temperature.

The CCD is cooled by three Peltier elements with a temperature range from 233 to 293 [°K] and maintained in a dry atmosphere of argon to avoid condensation on the sensitive surface. The acquisition is made through a Lab-NB (National Instruments<sup>®</sup>) 12-bit ADC board plugged in a Macintosh II fx. The program has been developed with LabVIEW<sup>®</sup> 2 program. The images have a dynamic range from -2048 to 2047 (-5 to 5 [V]).

The board is initialised (board number, channel, timers) in a first step to ready it for acquisition. Then the CCD is set to 0 (or black) to remove the former image or noisy photons (the camera is supposed to be maintained in a total dark environment). The timers wait for the CCD board signal to be externally triggered. When the acquisition starts, the timer wait during the given number of ticks corresponding to the integration time. The CCD is illuminated during that time. Then the CCD is covered by a shutter to stop imaging and to avoid a noisy surplus of photons during read-out. The CCD is finally discharged through the bottom line, line after line, each line being shifted one step downwards.

The rendering of black (level 0) has been measured at different gains (Fig. A.16) to have the reference.

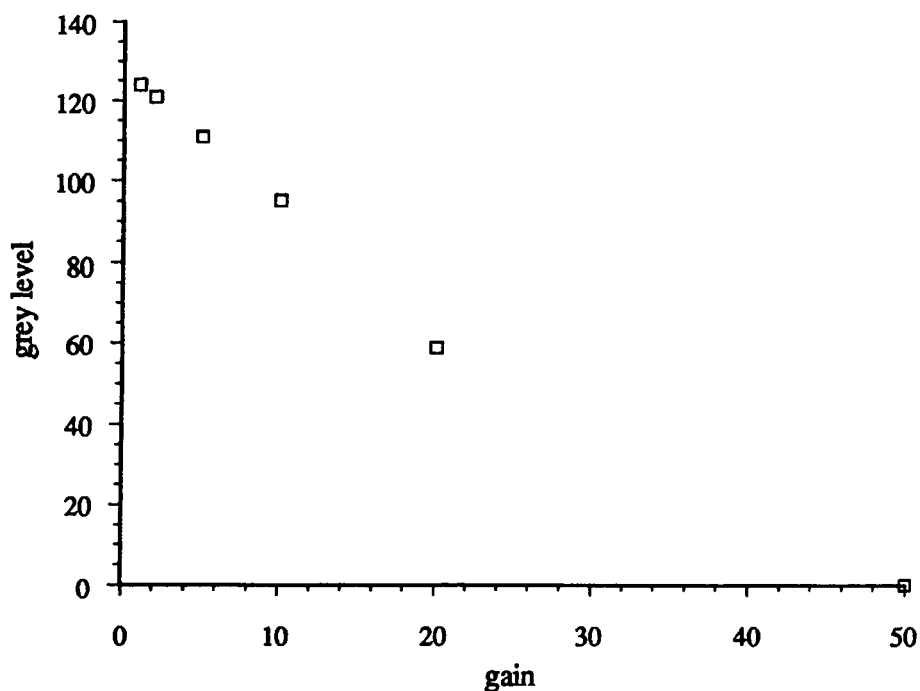


Fig. A.16: measured background intensity corresponding to black for the different available gain on the acquisition board.

## Curriculum vitae

**Last Name:** de Haller  
**First Name:** Emmanuel Bendicht  
**Birth date and Place:** August 25, 1962, Baden, Aargau, Switzerland  
**Citizenship:** Swiss  
**Marital Status:** single  
**Present Title:** Phys. Dipl. ETHZ  
**Office Address:** Laboratoire de Génie Médical  
Champs-Courbes 1  
CH-1024 Ecublens, Switzerland  
**Home Address:** Cherrat 6  
CH-1162 St. Prex, Switzerland

---

### Education:

Collèges de Lausanne, Latin and ancient Greek, 1973-1977.  
Boarding School, Maya-Joie, La Fouly, Switzerland, 1977-1978.  
Collège de Champittet, Pully, Switzerland, 1978-1983, Federal Maturity Certificate type C (sciences) in 1983.  
Swiss Federal Institute of Technology in Zurich (ETHZ), 1983-1988, diploma of physicist (Dept. IX) in 1988.  
Swiss Federal Institute of Technology in Lausanne (EPFL), Biomedical Engineering Laboratory, 1990-1993, PhD student on time resolved breast transillumination (supervisor: C. Depeursinge, PhD), PhD degree in march 1993.  
Postgraduate course on *Biomedical Engineering* (EPFL), 1990.  
Comett Euro-BME (biomedical engineering) course (PRAGM/PERMED) on *Medical Imaging*, 1991.  
Comett Euro-BME (biomedical engineering) course (PRAGM/PERMED) on *Instrumentation: "Minimum-Invasive" Intervention Techniques*, 1991.

### Experience:

Diploma work on high power laser transmission optimisation through optical fibers with molten lenses for ophthalmology (supervisor: Professor P. Niederer) ETHZ, Zürich, 1988.  
Biomedical Engineering Laboratory (EPFL), 1989, development of a tissular optical oximeter on four wavelength in the NIR for Zyma (Ciba-Geigy).

### Presentations:

A Cutaneous Sensor for Oximetry. *Medical Bioelectric and Thermal Surface Sensors*, INSERM, June 1990, Lyon, France.  
Time Resolved Breast Transillumination: a Preliminary Comparison between Monte Carlo Simulation and Measurements. *XVIII International Quantum Electronics Conference*, June 1992, Vienna, Austria.  
Time Resolved Transillumination: Simulation and Comparative Results. *14th Annual International Conference of the IEEE Engineering in Medicine and Biology Society*, October 1992, Paris, France.  
Time resolved breast transillumination: Monte-Carlo simulation and comparison with experimental results. *Biomedical Optics '93*, January 1993, Los Angeles, USA.

### Papers:

Rol, P., Niederer, P., Frankhauser, F., Arigoni, M. and de Haller, E.B. (1990) Q-switched pulses and optical breakdown generation through optical fibers. *Laser and Light in Ophthalmology*, 3, 213-219.  
de Haller, E.B. and Depeursinge, C. (1991) A Cutaneous Sensor for Oximetry. *Innov. Tech. Biol. Med.*, 12, 89-97.  
de Haller, E.B. and Depeursinge, C. (1992) Time Resolved Breast

Transillumination: a Preliminary Comparison between Monte Carlo Simulation and Measurements. *International Conference on Quantum Electronics Technical Digest series 1992*, 9, 410.

de Haller, E.B. and Depeursinge, C. (1992) Time Resolved Transillumination: Simulation and Comparative Results. *Proceedings of the 14th Annual International Conference of the IEEE EMBS*, 14, 334-335.

de Haller, E.B. and Depeursinge, C. (1993) Time resolved breast transillumination: Monte Carlo simulation and comparison with experimental results. *Proceedings of the SPIE Biomedical Optics'93*, in press.

de Haller, E.B. and Depeursinge, C. (1993) Simulation of the Time Resolved Breast Transillumination. *Med. & Biol. Eng. & Comp.*, 31, in press.

**“Pour me rassurer je me dis que les yeux ne peuvent pas tout voir  
et qu’il ne reste au coeur que ce qu’il peut contenir”**  
*Autre Face dans Sources du Vent de Pierre Reverdy*







*He'enalu*